

1999

Design, fabrication and analysis of a Terfenol-D based magnetostrictive external cavity diode laser sensor with an advanced signal processing capability

Wing Chiu Chung
Iowa State University

Follow this and additional works at: <https://lib.dr.iastate.edu/rtd>

 Part of the [Electrical and Electronics Commons](#), [Electromagnetics and Photonics Commons](#), and the [Physics Commons](#)

Recommended Citation

Chung, Wing Chiu, "Design, fabrication and analysis of a Terfenol-D based magnetostrictive external cavity diode laser sensor with an advanced signal processing capability " (1999). *Retrospective Theses and Dissertations*. 12655.
<https://lib.dr.iastate.edu/rtd/12655>

This Dissertation is brought to you for free and open access by the Iowa State University Capstones, Theses and Dissertations at Iowa State University Digital Repository. It has been accepted for inclusion in Retrospective Theses and Dissertations by an authorized administrator of Iowa State University Digital Repository. For more information, please contact digirep@iastate.edu.

INFORMATION TO USERS

This manuscript has been reproduced from the microfilm master. UMI films the text directly from the original or copy submitted. Thus, some thesis and dissertation copies are in typewriter face, while others may be from any type of computer printer.

The quality of this reproduction is dependent upon the quality of the copy submitted. Broken or indistinct print, colored or poor quality illustrations and photographs, print bleedthrough, substandard margins, and improper alignment can adversely affect reproduction.

In the unlikely event that the author did not send UMI a complete manuscript and there are missing pages, these will be noted. Also, if unauthorized copyright material had to be removed, a note will indicate the deletion.

Oversize materials (e.g., maps, drawings, charts) are reproduced by sectioning the original, beginning at the upper left-hand corner and continuing from left to right in equal sections with small overlaps. Each original is also photographed in one exposure and is included in reduced form at the back of the book.

Photographs included in the original manuscript have been reproduced xerographically in this copy. Higher quality 6" x 9" black and white photographic prints are available for any photographs or illustrations appearing in this copy for an additional charge. Contact UMI directly to order.

UMI[®]

**Bell & Howell Information and Learning
300 North Zeeb Road, Ann Arbor, MI 48106-1346 USA
800-521-0600**

**Design, fabrication and analysis of a Terfenol-D based
magnetostrictive external cavity diode laser sensor with an
advanced signal processing capability**

by

Wing Chiu Chung

A dissertation submitted to the graduate faculty
in partial fulfillment of the requirements for the Degree of
DOCTOR OF PHILOSOPHY

Major: Electrical Engineering (Electromagnetics)

Major Professors: Robert Weber and David Jiles

Iowa State University

Ames, Iowa

1999

Copyright © Wing Chiu Chung, 1999. All rights reserved.

UMI Number: 9940192

**Copyright 1999 by
Chung, Wing Chiu Russell**

All rights reserved.

**UMI Microform 9940192
Copyright 1999, by UMI Company. All rights reserved.**

**This microform edition is protected against unauthorized
copying under Title 17, United States Code.**

UMI
300 North Zeeb Road
Ann Arbor, MI 48103

**Graduate College
Iowa State University**

**This is to certify that the Doctoral dissertation of
Wing Chiu Chung
has met the dissertation requirements of Iowa State University**

Signature was redacted for privacy.

Co-Major Professor

Signature was redacted for privacy.

Co-Major Professor

Signature was redacted for privacy.

For the Major Program

Signature was redacted for privacy.

For the Graduate College

TABLE OF CONTENTS

LIST OF FIGURES	vi
ABSTRACT	xii
1. INTRODUCTION	1
1.1 Overview	1
1.2 Organization of Dissertation	2
2. PROTOTYPE FABRICATION	6
2.1 Introduction	6
2.2 Fabrication of an External Cavity Diode Laser Sensor	6
2.3 Mechanical Design of the Diode Laser Sensor Housing	10
2.4 Preparation of the Transducer Material	15
3. PROTOTYPE EVALUATION	20
3.1 Introduction	20
3.2 Interferometer Measurement Results	20
3.3 Alignment of the Transducer Module with the Diode Laser Sensor	26
3.4 Mechanical Translator Assisted Method	26
3.5 Iterative Adjustment Method	29
3.6 Closed-loop Alignment Method	31
3.7 Performance Evaluation of the Magnetometer Prototype	32
3.8 An Alternative Housing Design for the Sensor	37
4. ANALOG SUPPORTING ELECTRONICS	39
4.1 Introduction	39
4.2 Photodetector Pre-Amplifier	39
4.3 Detection Schemes	40
4.4 Design Issues	42
4.4.1 Amplifier gain	42
4.4.2 Stability and phase compensation	43
4.4.3 Noise bandwidth and noise gain	46
4.5 Bias Cancellation Circuitry	47
4.6 Simulation Results	50
4.7 Diode Laser Current Driver	54
4.8 Regulated Current Source	54
4.9 Voltage Compliance, System Stability and Sensitivity	56
4.10 Noise and Fluctuation Sources	58

4.11 Transient Protection Circuitry	62
4.12 Analog-to-Digital Converters and Other Issues	65
4.13 Servo Techniques for Extended Stability and Dynamic Range	65
4.14 Power Budget	68
4.15 Mixed Signal Layout Issues	69
5. COMPUTER MODELING OF THE DIODE LASER SENSOR COUPLED TO AN EXTERNAL TRANSDUCER	72
5.1 Problem Description	73
5.2 Mathematical Derivation on Calculating the Reflection Coefficient	76
5.2.1 Modeling of a Rough External Reflector	83
5.3 Computation Results	83
6. LIMIT OF SENSITIVITY OF THE TERFENOL BASED DIODE LASER SENSOR	89
6.1 Operation of the Device	89
6.2 Photodetector Preamplification Noise	90
6.3 Diode Laser Intensity Noise	93
6.4 Diode Laser Phase Noise	97
6.5 Total System Noise	98
7. CONCLUSIONS	100
7.1 System Engineering	101
7.2 Current Status	102
7.3 Future Direction.....	103
APPENDIX A. OPERATING PRINCIPLE OF A HETERODYNE INTERFEROMETER	104
APPENDIX B. DATA SHEETS OF THE DIODE LASER ML-4403 USED IN THIS STUDY	109
APPENDIX C. SPICE LISTINGS FOR VARIOUS ANALOG CIRCUITS	113
APPENDIX D. BASIC PROPERTIES OF AN EXTERNAL CAVITY DIODE LASER SENSOR	129
APPENDIX E. MATLAB SOURCE CODE FOR CALCULATING MODAL REFLECTIVITY	143
APPENDIX F. DESCRIPTION OF ON-BOARD MICROCONTROLLER	152

APPENDIX G. APPLICATION OF AN EXTERNAL CAVITY SENSOR IN THERMAL DISTORTION IMAGING	154
REFERENCES	155
ACKNOWLEDGEMENTS	158

LIST OF FIGURES

Figure 1.1	Block diagram showing the scope of the dissertation, which discusses the fabrication and performance assurance processes of the magnetometer development.....	3
Figure 2.1	Schematic diagram showing the interaction between the diode laser cavity and an external reflector closely coupled to one end of the cavity	7
Figure 2.2	Anatomy of a typical commercial diode laser in TO-5 format (drawing not to scale).....	9
Figure 2.3	Coupling complication due to diode laser manufacturing process. For example, (i) the location of the chip may not be flush with the heat sink. (ii) the connection pin prevents the diode laser facet from close coupling to an external reflector, and (iii) a similar problem as before but the location of the bonding wire is too close to the end of the pin.	11
Figure 2.4	Mechanical drawing for the magnet and transducer holder.	13
Figure 2.5	Original drawing for the sleeve for holding the magnet and the Terfenol transducer	14
Figure 2.6	Side view and top view of the assembled magnetometer prototype	16
Figure 2.7	Plot of dc magnetostriction of a Terfenol-D rod versus applied field strength. The measurement was obtained with a strain gauge attached to a Terfenol rod and the dc magnetic field was generated by an electromagnet.	17
Figure 2.8	Schematic diagram showing the application of a diamond saw in slicing the Terfenol-D material.	19
Figure 3.1	Experimental setup for transducer disk evaluation using a heterodyne interferometer capable of nanometer resolution. A solenoid coil is used to excite the transducer under test and the demodulated output of the interferometer is detected with an amplifier for synchronous detection. The data is collected via a desktop computer.	21
Figure 3.2	Different views of spatial scan results of a Terfenol-D disk with a heterodyne interferometer under an ac field excitatin 19 kHz.	22

Figure 3.3	Different views of spatial scan results of a Terfenol-D disk with a heterodyne interferometer under an ac field excitatin 45 kHz.	23
Figure 3.4	Different views of spatial scan results of a Terfenol-D disk with a heterodyne interferometer under an ac field excitatin 60 kHz.	24
Figure 3.5	Cross-sectional views of spatial scan results of a Terfenol-D disk with a heterodyne interferometer under an ac field excitation at various frequencies.	25
Figure 3.6.	Schematic diagram showing the critical alignment parameters for the diode laser external cavity sensor and the Terfenol transducer. These are the coupling distance and the angles between the XZ axis and the YZ axis.	27
Figure 3.7	One of the alignment techniques used in adjusting the coupling angle and position between the magnet assembly and the sensor.	28
Figure 3.8	Schematic illustrating the iterative alignment technique for aligning the transducer assembly.	30
Figure 3.9	Experimental setup for evaluating the performance of the sensor module. Both a lock-in amplifier and the spectrum analyzer are used to determine the signal strength, signal-to-noise ratio, and presence of spurious harmonics.	33
Figure 3.10	Magnetometer response as a function of excitation current with various excitation frequencies.	34
Figure 3.11	Frequency response of the prototype magnetometer with a fixed level of field excitations. A resonance peak is observed.	35
Figure 3.12	Frequency response of the prototype magnetometer signal-to-noise ratio on a log-log scale plot.	36
Figure 3.13	Schematic showing an improved design on the magnetometer housing. This design will aid the alignment process by using a tubular structure and by introducing a fine threaded inner core for adjustment between the diode laser holder and the transducer.	38

Figure 4.1	Schematic diagram of a transimpedance amplifier consists of a non-ideal operational amplifier. The finite gain of the amplifier fails to remove the diode capacitance which imposes a feedback pole on the system, causing potential instability.	41
Figure 4.2	Bode plot of gain versus frequency of an operational amplifier and its inverse feedback factor versus frequency plots.	45
Figure 4.3	(a) Circuit topology for a photodetector pre-amplifier with a low pass filter inside the feedback loop of the system. (b)Alternatively, the low pass filter can be placed outside the feedback loop. However, the former configuration provides a better noise performance.	48
Figure 4.4	A servo amplifier(i.e., an integrator) is used to continuously compensate for the dc background of the optical signal. The diagram indicates the technique schematically. A detailed analysis is required to ensure stable operation of the servo system.	49
Figure 4.5	Bode plot of a properly compensated transimpedance amplifier. A low noise JFET input operational amplifier, AD745 is used for the simulation.	51
Figure 4.6	Simulation results of a photodetector preamplifier with a dc bias nulling scheme. the dc bias nullor composes of a low pass network and an open loop operational amplifier serves as the integrator.	52
Figure 4.7	Simulation results of an improperly compensated transimpedance amplifier. Due to the presence of the second order response of the network, any electrical noise at the input may drive the amplifier into oscillation.	53
Figure 4.8	Schematic diagram of voltage controlled current source. This topology utilizes a reference voltage and a servo amplifier to constantly regulate the voltage drop across the sense resistor.	55
Figure 4.9	A comparison of the voltage compliance capability of a simple resistor biased current source and a voltage controlled current source.	57
Figure 4.10	Compensation network will be required to keep the system from oscillation when the series pass element presents a capacitive load to the servo amplifier.	59

Figure 4.11	A current source reference voltage controlled current source. Using a current source as a reference can improve the stability of the system.	61
Figure 4.12	Topology of a transient suppressor circuit to protect the diode laser from accidental current and voltage spike.	63
Figure 4.13	Response of the transient suppressor to a current spike. Similar response can be found for a voltage excitation.....	64
Figure 4.14	Block diagram showing the concept of comb filtering based signal separation technique.	66
Figure 4.15	Schematic diagram showing the concept of different servo techniques for maintaining system sensitivity and dynamic range.	67
Figure 4.16	System Power Budget.	70
Figure 4.17	Schematic diagram showing a recommended layout protocol for a mixed signal system.	71
Figure 5.1	Schematic diagram showing the waveguide discontinuity problem of the diode laser sensor. Region 1 composes of the diode laser cavity, region 2 is the coupling gap and region 3 is the transducer material.	73
Figure 5.2	The modal distribution of the fundamental, even TE mode of a symmetrical weakly guiding waveguide.	84
Figure 5.3	The spectral domain distribution of the fundamental, even TE mode of a symmetrical weakly guiding waveguide.	86
Figure 5.4	The modal reflectivity of a diode laser sensor coupled to a perfect external reflector with a varying coupling distance.	87
Figure 5.5	An experimental setup to evaluate the coupling distance of the diode laser sensor via the far field radiation pattern of the system.	88
Figure 6.1	Small signal model of a reversed biased PIN photodetector. I_{photo} is the ideal current generator, G_d is the resistance of the diode when it is reversed biased, C_d is the junction capacitance, and R_s is the contact resistance.	91

Figure 6.2	RIN of an index guided diode laser at a modulation frequency of 50 MHz.	94
Figure 6.3	RIN of a diode laser at baseband frequency.	96
Figure A1	Optical setup for the OP-35 heterodyne interferometer.....	105
Figure D1.1	(a) Experimental result of output power versus external cavity length. The starting position is not exactly known. A 99% mirror was used as the external reflector	130
	(b) Variation of output power versus external cavity length with two different sets of external reflector. The solid lines represent the plot of output variation using a 35% external reflector while the dashed line represents the output power fluctuation of the diode laser using a 4% reflector.	131
Figure D1.2	(a) Top view and side view of a diode laser chip mounted to a heatsink. Although the chip was carefully aligned, the solder chip prevented a tight coupling distance.	133
	(b) Experimental setup for studying the reflectivity modulation property of a diode laser.	135
Figure D2.1	The output of the monitoring photodetector of a diode laser coupled to a 4% reflector. The coupling distance is modulated by a piezoelectric translator excited by a 1 volt peak sinusoidal voltage. The non-linearity of the output indicates the modulation span beyond a half a wavelength.	137
Figure D2.2	The dc output level of the monitoring detector at different coupling distances between the 4% reflector and the diode laser.	138
Figure D2.3	The output voltage of the photodetector when the coupling distance between the 4% reflector is modulated by an piezoelectric translator. The upper trace shows the output of the photodetector when the operating point of the system was set manually at its maximum. The lower trace shows the output of the system when it is biased at the optimal position.	139
Figure D2.4	The output of the photodetector when the coupling distance between the 4% reflector and the diode laser is modulated with a 3.5 volts peak saw-tooth signal. The distortion of the waveform (i.e., the rounding off	

of the corner) may be a result of the bandwidth of the piezoelectric translator. 141

Figure D2.5 The output voltage of the photodetector when the coupling distance between the diode laser and the 4% reflector is modulated by a 4.5 volts peak saw-tooth signal. The dc bias level of the diode laser is increased considerably with respect to the experimental result shown in Fig. D2.4. With a higher bias, the output of the diode laser spans a greater range. 142

Figure F1 Block diagram showing the organization of the on-board microcontroller unit developed for the pocket size magnetometer. 153

ABSTRACT

Miniature magnetometer is desired in many applications, such as undersea surveillance, buried landmine detection, vehicle tracking and guidance and personal dosimetry. This dissertation reports the fabrication, and characterization of a miniature magnetometer, which utilizes the highly magnetostrictive material, Terfenol-D and an ultra-short external cavity diode laser sensor. A thin slice of the magnetostrictive material, biased by an open magnetic circuit, is configured as an external reflector modulating the effective modal reflectivity of the diode laser cavity in response to an ac magnetic field. The detection limit of the sensor are being investigated and the principle of the device is being examined as an abruptly terminated dielectric waveguide problem. Numerical results are obtained. Furthermore, the spatial variation of the magnetostriction amplitude across the transducer is being examined with a heterodyne interferometer. Suggestions are provided on improving the device performance, and extending the numerical capability to account for non-ideal reflector. Other metrology applications using the diode laser sensor is discussed.

1. INTRODUCTION

1.1 Overview

A miniature magnetometer is desired for different areas of application, ranging from land and undersea surveillance to personal dosimeter. The desired magnetometer should be capable of measuring a low frequency magnetic fields from 0.1 Hz to 20 kHz at low milli-Oersted level (The commonly used magnetic field measurement unit in the power industry is Gauss, which is equivalent to Oersted in free space). It should be configurable as a data logger and be manufacturable at a relatively low cost. Although quite a few magnetometers are available in the market, none of these devices can measure mOe signal levels in the mentioned frequency range with a small package size and at a reasonable price.

The concept of a novel optical magnetometer was demonstrated in a previous study [1] and the availability of a miniaturized version of such a magnetometer will facilitate many mobile field mapping applications. In this dissertation, we developed and evaluated a pocket-sized optical magnetometer which has a wide measurement bandwidth and is relatively inexpensive. A low cost diode laser, which is used in compact disk players, and a highly magnetostrictive material, Terfenol-D, served as the sensing element in this miniature magnetometer. The perturbation in the physical dimensions of a magnetostrictive material, as a result of an external ac magnetic field excitation, is detected with an external cavity diode laser configured as an optical displacement sensor. A photodetector, located in the same package as the diode laser, provided an amplitude modulated signal proportional to the displacement of the magnetostrictive material. This signal was then conditioned, sampled and numerically processed by an on-board micro-controller to estimate the frequency content of the ac magnetic fields.

Different types of signal processing algorithms can be employed by modifying the firmware. The microcontroller was also capable of storing the data in memory, which can be downloaded to a desktop computer at a later time for further analysis. In addition, a liquid crystal display mounted on the magnetometer indicated some user pre-selected information about the measurement.

1.2 Organization of Dissertation

The scope of this dissertation discusses the fabrication process and quality assurance techniques involved in ensuring a reproducible device. For example, the fabrication process starts with a careful examination of the properties of the diode laser sensor and the miniaturized transducer module. It is especially important in identifying and avoiding the factors limiting the performance of the sensor and the transducer. Both the sensor and the transducer module are then integrated with the supporting analog and digital electronics modules. The theoretical limitation of the device and further optimizations are examined. A numerical engineering design aid are developed to study performance limiting factors when experimental investigation becomes impossible. Figure 1.1 depicts a block diagram showing the scope of the dissertation.

This dissertation is organized as follows: Chapter 2 describes the construction procedure and the mechanical design of the miniature sensor module using a highly magnetostrictive material, Terfenol-D and an external cavity diode laser sensor. An improved design of the sensor housing is also discussed. The laboratory performance of the prototype, such as frequency response, sensitivity and output linearity, are presented in Chapter 3, where an optical measurement of the ac magnetostriction of a Terfenol-D disk using a HeNe heterodyne interferometer is described. A proposal for the origin of the observed ac magnetostric-

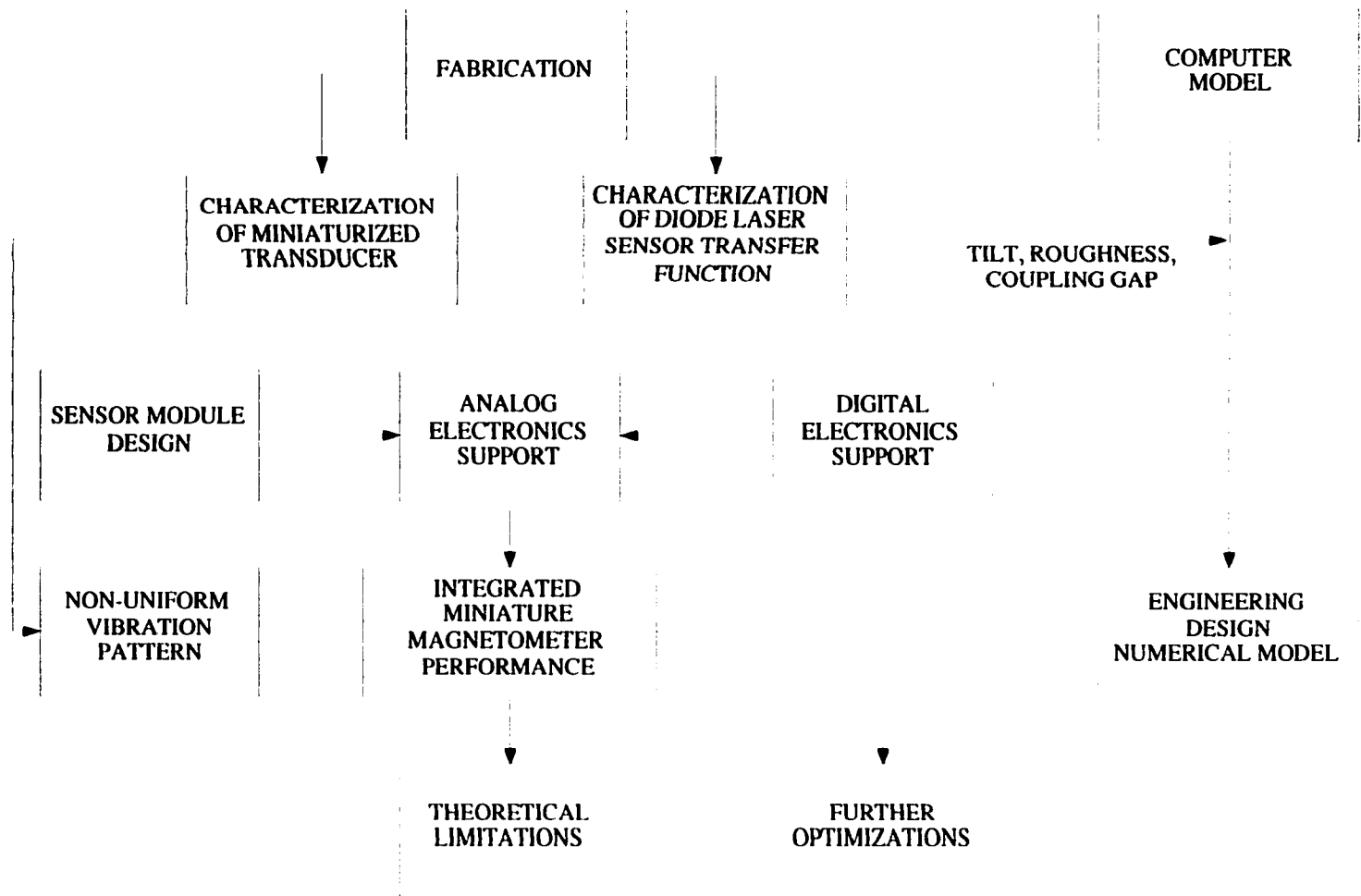


Figure 1.1 Block diagram showing the scope of the dissertation, which discusses the fabrication and performance assurance processes of the magnetometer development.

tion pattern is included for further study. This chapter provides all the necessary detail for successfully reproducing the prototype.

Chapter 4 explains the design and analysis of supporting electronics for the prototype. We examine the details for the design of the photodetector amplifier and the diode laser driver in this chapter. Since the noise performance and stability of the above systems are critical to an optimal detection process and pose a lower limit to the system sensitivity, PSpice simulations of the analog circuit stability and noise performance are provided. In addition, alternative design methodologies for the diode laser current drivers are compared and discussed. Furthermore a design for a $1/f$ noise reduction scheme is presented. This scheme provides a more versatile solution than the conventional automatic gain control technique commonly used in optical communication systems [2]. As the diode laser can be damaged by electrostatic discharge, the designs of transient protection and soft-starter circuits are given.

Chapter 5 provides a theoretical understanding of the operating principle of the diode laser external cavity sensor. We have modeled the electromagnetic scattering process between the diode laser and the Terfenol end face. We have considered a parallel reflector and studied its effect on the operation of the diode laser sensor. The solution to the problem of a tilted reflector is outlined. Furthermore, the modelling approach to the effect of a rough scattering surface on the operation is proposed.

The scattering problem is approached with a plane-wave expansion technique and is solved numerically. Our model treats the interaction process as a steady state phenomenon; therefore, the oscillating frequency pulling of the laser due to the perturbation of an external cavity is ignored in the treatment. Consequently, we have not explored the effect of the external cavity on the dynamics of the diode laser. The results of this work can be used to study a diode laser's performance with an imperfect anti-reflection coating and the applica-

tion of multiple anti-reflection layers for optical amplification.

Chapter 6 discusses the ultimate sensitivity, limited by the intrinsic phase noise and intensity noise of the diode laser, the shot noise of the photodetector system, and the noise introduced by the diode laser driver.

We have summarized the findings in Chapter 7, the conclusions, and proposed future directions for the research. Furthermore, the system engineering aspect, such as calibration, maintainability and manufacturability, of the device is discussed.

2. PROTOTYPE FABRICATION

2.1 Introduction

A rugged and simple magnetostrictive optical magnetometer was fabricated using the highly magnetostrictive material, Terfenol-D, and an external cavity diode laser sensor. The concept of this novel magnetometer has been demonstrated in a previous study [3]. This section of the thesis describes the fabrication of a compact prototype suitable for a pocket-size personal magnetic field dosimetry unit. The construction of an external-cavity-diode-laser sensor and the miniaturization of the transducer material is discussed together with the mechanical design of the housing. Also included are discussions of possible improvements in fabrication for the next generation prototype.

2.2 Fabrication of an External Cavity Diode Laser Sensor

Although a thorough investigation of the physics of the sensor is important, a simple approach which provides a sufficient guideline for fabricating a prototype device will be used in this chapter. A more rigorous analysis of the sensor's operating principle based on a plane wave spectrum approach will be analyzed in Chapter 5 of this thesis (see also [4]). By closely coupling a reflective object to one facet of a diode laser chip (i.e., facet A in Figure 2.1), the effective reflection coefficient on that facet is modified as a result of the multiple reflections of laser light between the object and the facet. Since the facet reflectivity of the cavity directly modulates the loss of the laser cavity, the output power of the diode laser is perturbed. Referring to Figure 2.1, as the coupling distance changes between the external reflector and the laser facet A in response to an external perturbation such as an ac magnetic

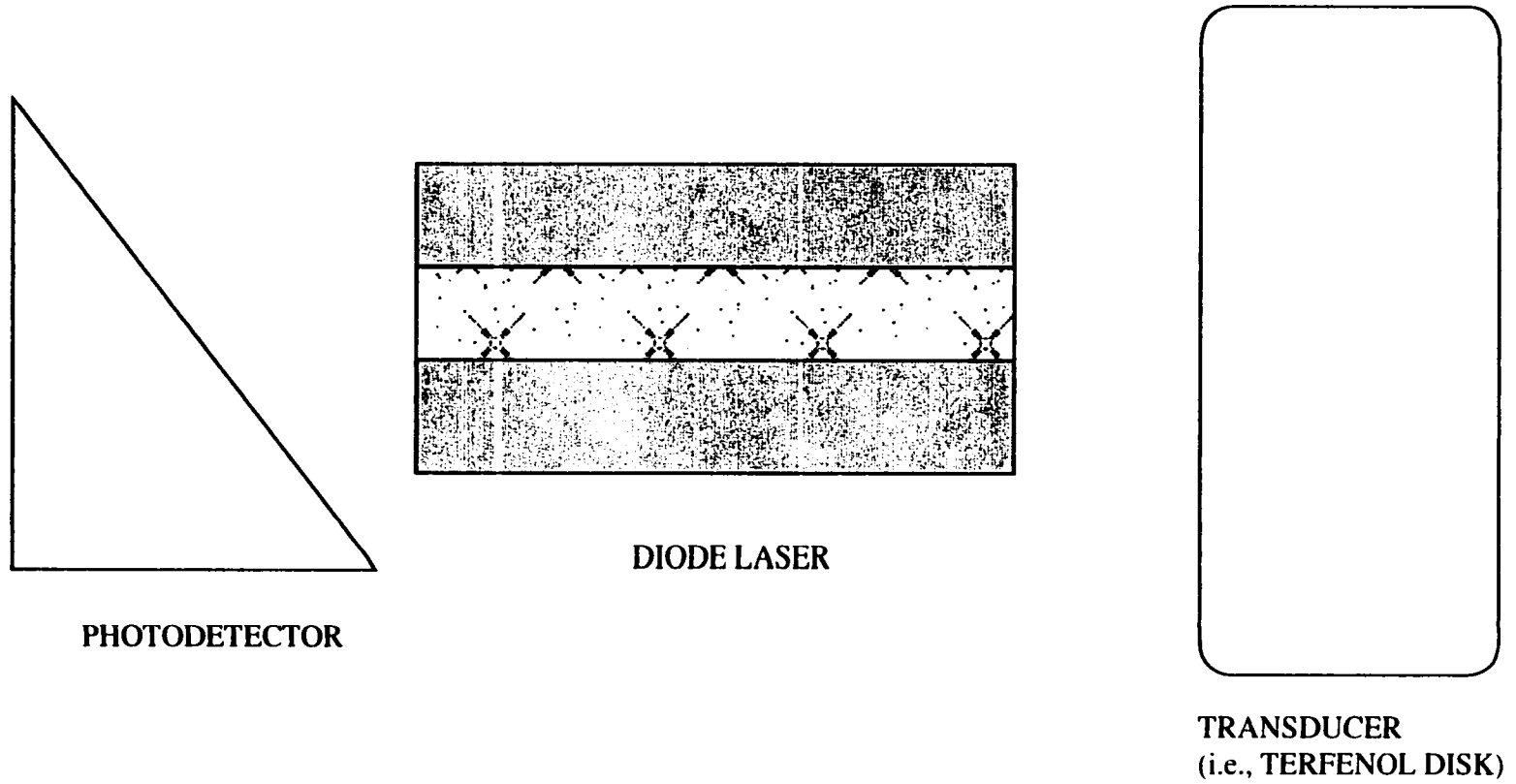


Figure 2.1 Schematic diagram showing the interaction between the diode laser cavity and an external reflector closely coupled to one end of the cavity

field, an amplitude modulation on the output intensity of the laser will be observed. Although this simple explanation ignores the diffraction loss of the laser light during the multiple reflection process, it qualitatively describes the behavior of the sensor.

Researchers at the Naval Research Laboratory [5] reported that a coupling distance less than 10 μm was desired for a device with adequate sensitivity. The following discussions emphasize the procedure necessary for achieving good coupling to a commercial compact-disk player diode laser. Most low-cost diode lasers are designed for the compact disk player and optical disk drives. The diode laser is usually packaged in a 9 mm (i.e., TO-5) or a 5.6 mm format as shown in Figure 2.2. An aperture on top of the header permits the laser to radiate to the outside. This aperture is usually protected by an anti-reflection (AR) coated sapphire or glass window with a typical thickness of 0.4 mm to 0.7 mm. The diode laser chip is located 1.5 mm to 2.0 mm beneath the sapphire window. Therefore, the standard 9 mm packaging style prevents a close coupling to the diode laser facet and a mechanical modification of the laser diode was required. Although most manufacturers produce an open-carrier package allowing easy access to the laser chip, the price and the quality of such a diode laser was not suitable for this project. Besides, the open-carrier package does not include a built-in photodetector that comes as standard with the 9 mm package. However, the 9 mm header can be removed manually and the laser facet then becomes accessible to the experimenter.

Before any modification procedure was undertaken, the anode and cathode of the diode laser were shorted together by a conducting wire. This is a safety practice in preventing unexpected electrostatic damage to the laser diode throughout the modification process. Due to the delicate nature of the diode laser, the operator needs to be grounded and the operation must be performed at an anti-static station. Electrostatic damage to the diode laser may not be obvious immediately but the lifetime and the electrical or optical specification of

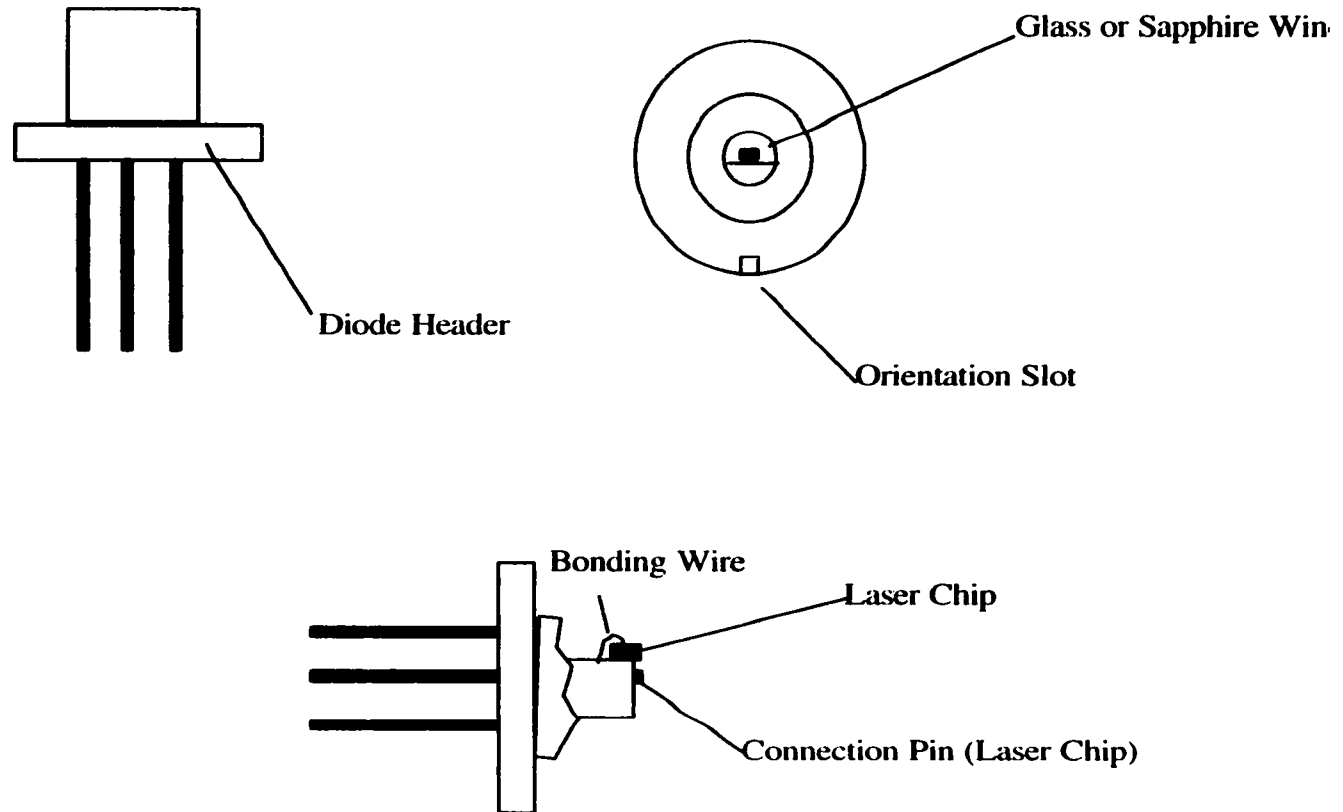


Figure 2.2 Anatomy of a typical commercial diode laser in TO-5 format (drawing not to scale)

the laser would be affected.

With the diode laser properly protected, the 9 mm can was then removed with a miniature saw blade with a high tooth per inch (TPI) ratio. Although a low TPI blade suffices, a high TPI blade produces a much better finish. The diode laser should be mounted on a custom-made holder during the operation. The blade should not be allowed to penetrate beyond the thickness of the capsule wall (i.e., 1.0 mm) during the sawing process otherwise mechanical damage to the bonding wire and the laser chip may occur. Usually, accidents occur as the capsule is about to detach and the blade , which cannot be stopped in time, allowing the SAW to cut inside the capsule and damage the connection pin to the diode chip. It is suggested that a lathe would be a more effective method for removing the capsule but it was not used in this work.

Depending on the model and the manufacturer of the diode laser, two complications may arise after the removal of the capsule: (a) the connection pin to the diode laser chip may prevent a tight coupling distance and (b) the chip may be offset from the edge of the heat-sink. The latter complication cannot be overcome by any means known but the former case can be resolved by cutting off the extra portion of the connection pin, provided the bonding wire is located in a favorable position. These complications are depicted in Figure 2.3. Once the capsule and all other obstacles are removed, the diode laser can be used in the fabrication of an external-cavity sensor.

2.3 Mechanical Design of the Diode Laser Sensor Housing

A miniature housing was also designed in this project. Besides working as a platform for the sensor, the housing also serves as a heat sink for the diode laser. The housing material must be non-magnetic to avoid any shielding effect on the measurement. Aluminum alloy

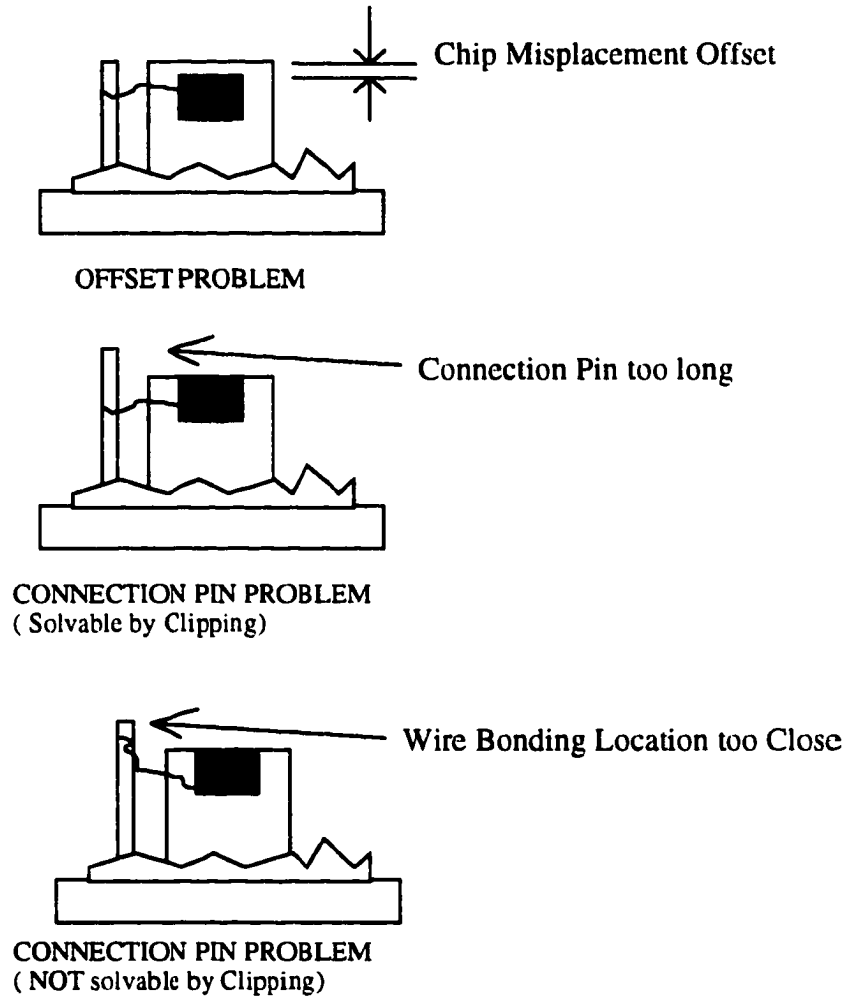


Figure 2.3 Coupling complication due to diode laser manufacturing process. For example, (i) the location of the chip may not be flush with the heatsink, (ii) the connection pin prevents the diode laser facet from close coupling to an external reflector, and (iii) a similar problem as before but the location of the bonding wire is too close to the end of the pin.

7075 was used in the fabricating the housing. Any other aluminum alloy or brass housing can be used. Copper was found to be an unsuitable material for the housing (despite its high heat conduction property) because of the softness of the material which caused many problems in the threading of screws. However, it should be noted that an aluminum housing will suffer from eddy current induced magnetic noise and other non-magnetic material, such as G-10 may be used instead. In general, a conductive enclosure is desired in protecting the device from potentially strong external electric fields.

The overall dimensions (i.e., width, height and length) of the housing should be minimized since limited space is available in a pocket-sized form factor. The function of the housing is to hold the diode laser head and the transducer in place. In order to achieve a tight coupling between the diode laser facet and the external reflector, fine resolution adjustments are anticipated in this diode laser magnetometer. The compactness requirement in this application eliminates the incorporation of any translation device in the housing. Thus, different techniques, which will be discussed later in this thesis, are used to circumvent the alignment difficulty. The present housing design proved to be effective for a laboratory prototype but a different design may be better suited for manufacturing.

The mechanical drawing for the housing and the transducer sleeve are shown in Figure 2.4 and Figure 2.5 respectively. As mentioned previously, the housing also serves as a heat sink to the diode laser. A good thermal contact between the housing and the header is desired. Thus, the contact area and the holding pressure of the header are maximized in this design. The diode laser header was clamped in placed via a 2-56 machine screw. It is critical that the header was seated perpendicular to the reference plane of the holder. Both the diode header platform and the transducer holder shared a common substrate for maximum mechanical stability. The current design can also be used to minimize the effect of thermal expansion on the performance of the sensor when the proper combinations of materials are chosen.

SCALE 1 : 1
DIMENSIONS: INCHES
MATERIAL: AL 2024-T3

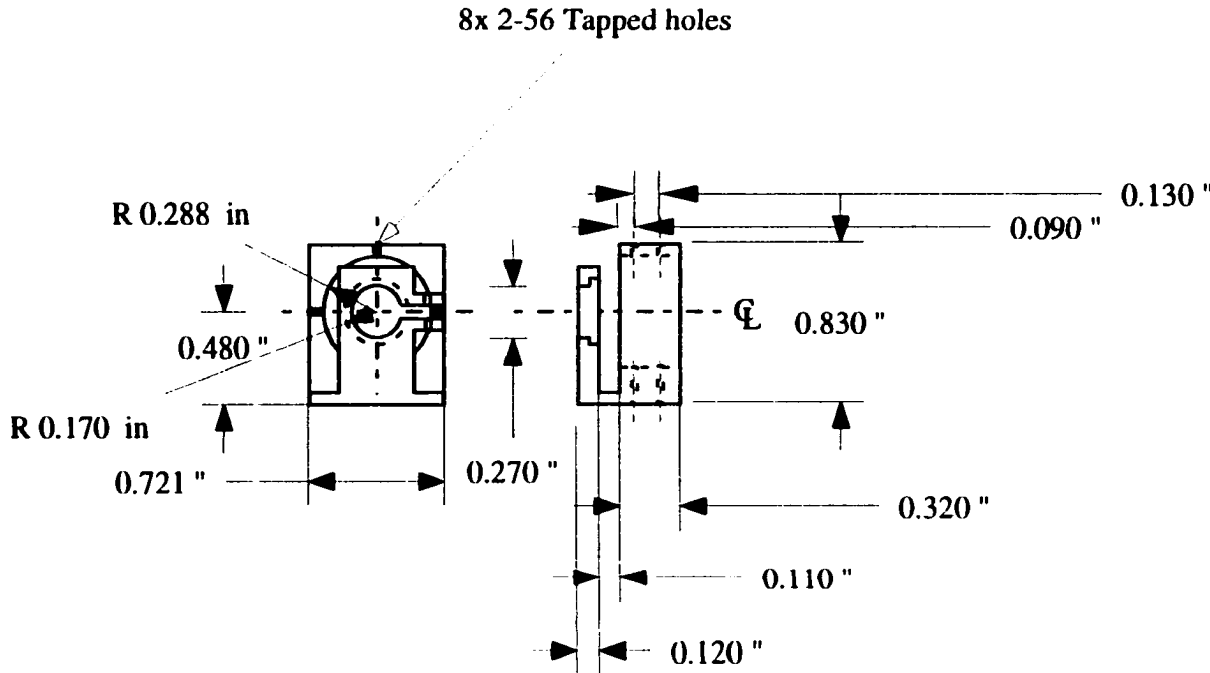


Figure 2.4 Mechanical drawing for the magnet and transducer holder.

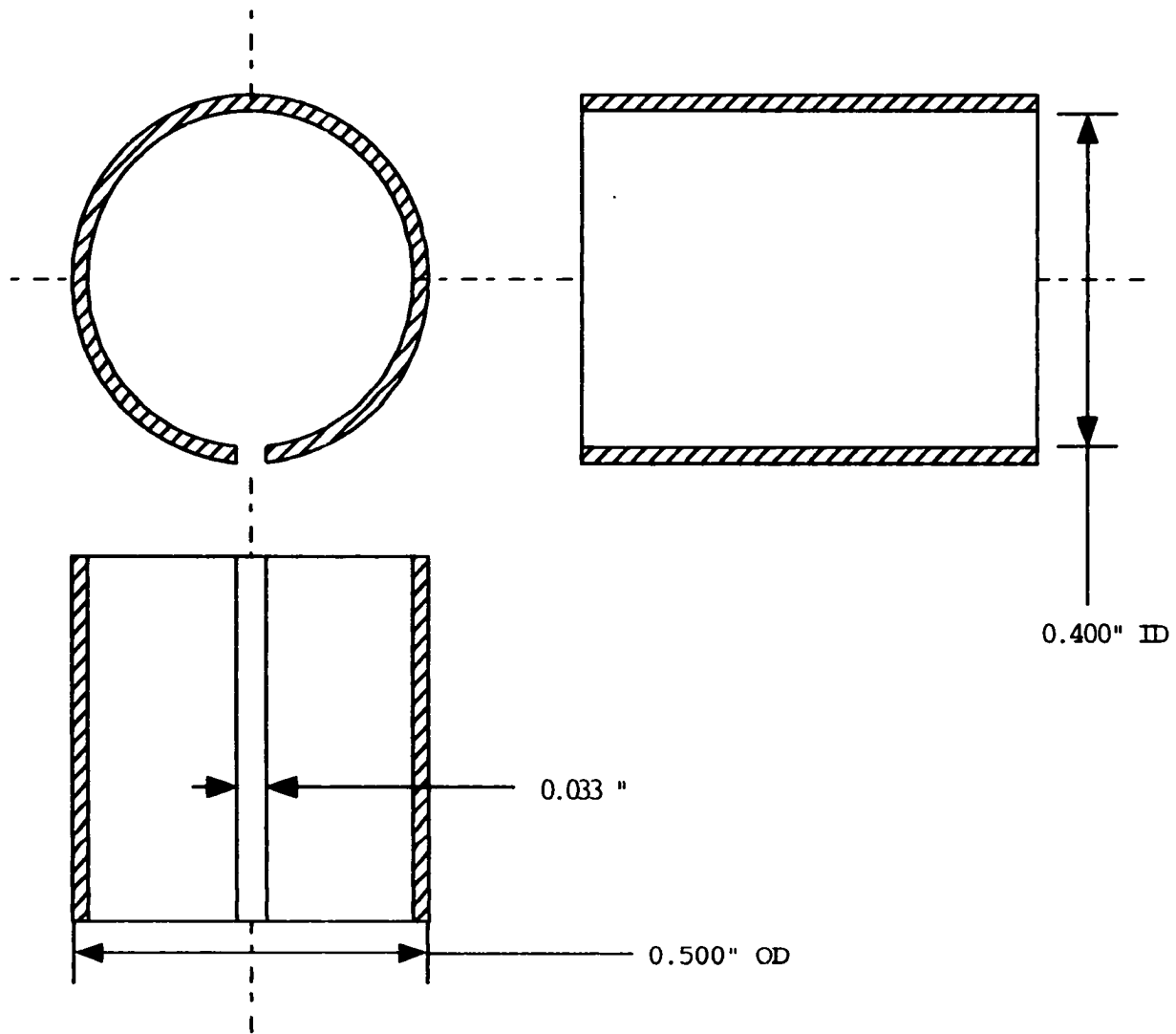


Figure 2.5 Original drawing for the sleeve for holding the magnet and the Terfenol transducer

Four 4-40 set screws (and epoxy), as shown in Figure 2.6 were used to hold the transducer (i.e., Terfenol-D disk) in place and they are not intended to provide any fine adjustment in this design. Instead, the sensor is aligned with external translators. The overall dimension of the housing was 25 mm wide x 25 mm long and 18 mm thick. The entire assembly was fabricated with a conventional milling machine at Ames Laboratory. A more complicated design can be fabricated with electric discharge machining (EDM) techniques.

2.4 Preparation of the Transducer Material

The highly magnetostrictive material Terfenol-D is used as the transducer material in this work. The operating characteristic of Terfenol-D is shown in Figure 2.7. The data was obtained with a strain gauge attached to the surface of a Terfenol rod and the dc magnetic field was generated by an electromagnet. It should be noted that only the dc operating characteristics of the transducer material was obtained using the above technique. A dc magnetic field bias, of approximately 200 Oe, is required for optimal ac performance. A 12 mm in diameter and 3 mm thick ceramic disk-shaped permanent magnet provided the necessary bias field in this prototype. The disk-shaped permanent magnet was sliced from a larger piece of permanent magnet with a diamond saw as shown in Figure 2.8. The magnetic flux of the disk-shaped magnet was determined with a Hall sensor and the spatial variation of the magnetic field intensity was also measured.

No 'hot-spot' or spatial localization of a high magnetic field intensity was observed in the sample. A 1 mm thick and 6.4 mm diameter Terfenol-D disk was removed from a Terfenol-D rod with a diamond-blade cutter. Since Terfenol-D is a brittle material, the saw must be operated at a slow cutting speed and appropriate force. The Terfenol-D assembly was then polished with optical lapping papers to provide a reflecting surface. No other post-

Magnetometer Housing Design

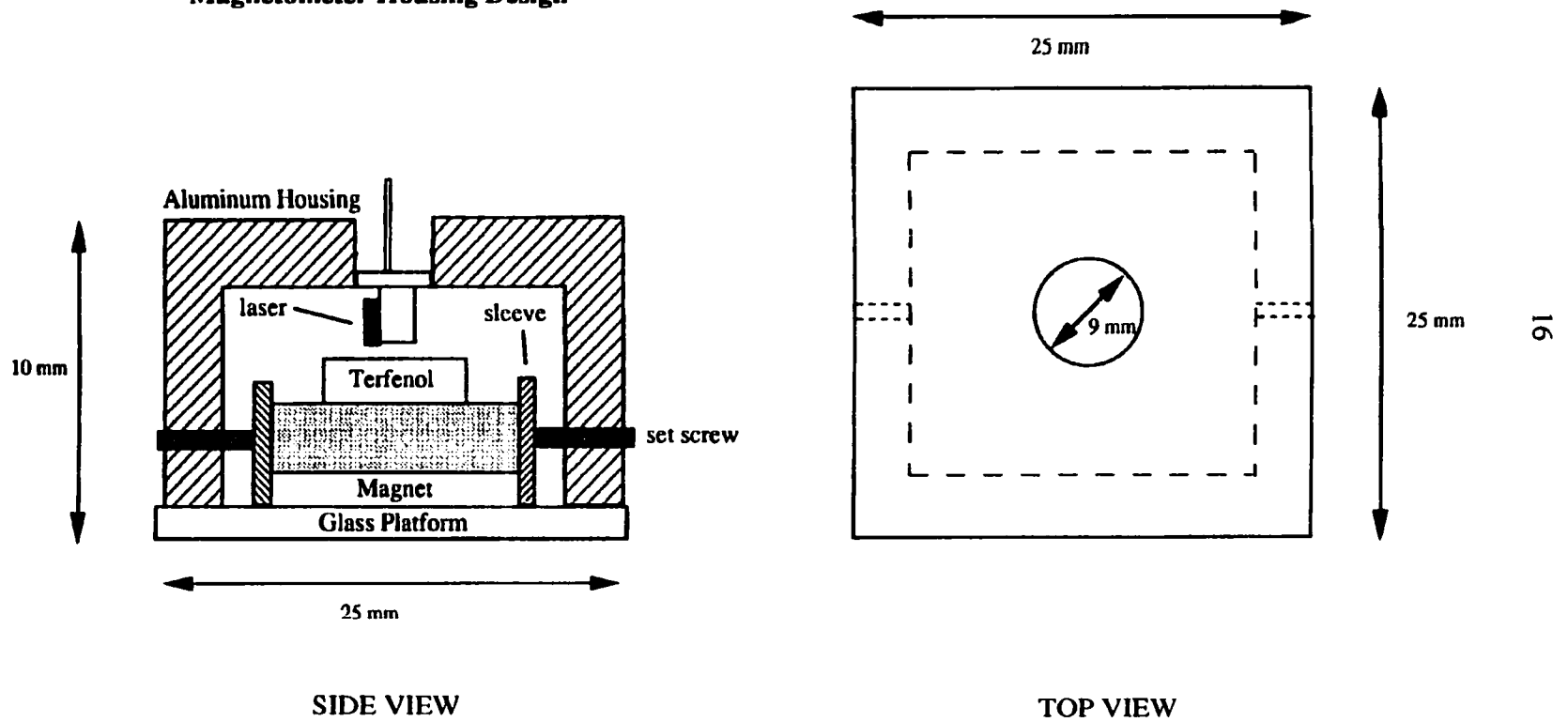


Figure 2.6 Side view and top view of the assembled magnetometer prototype

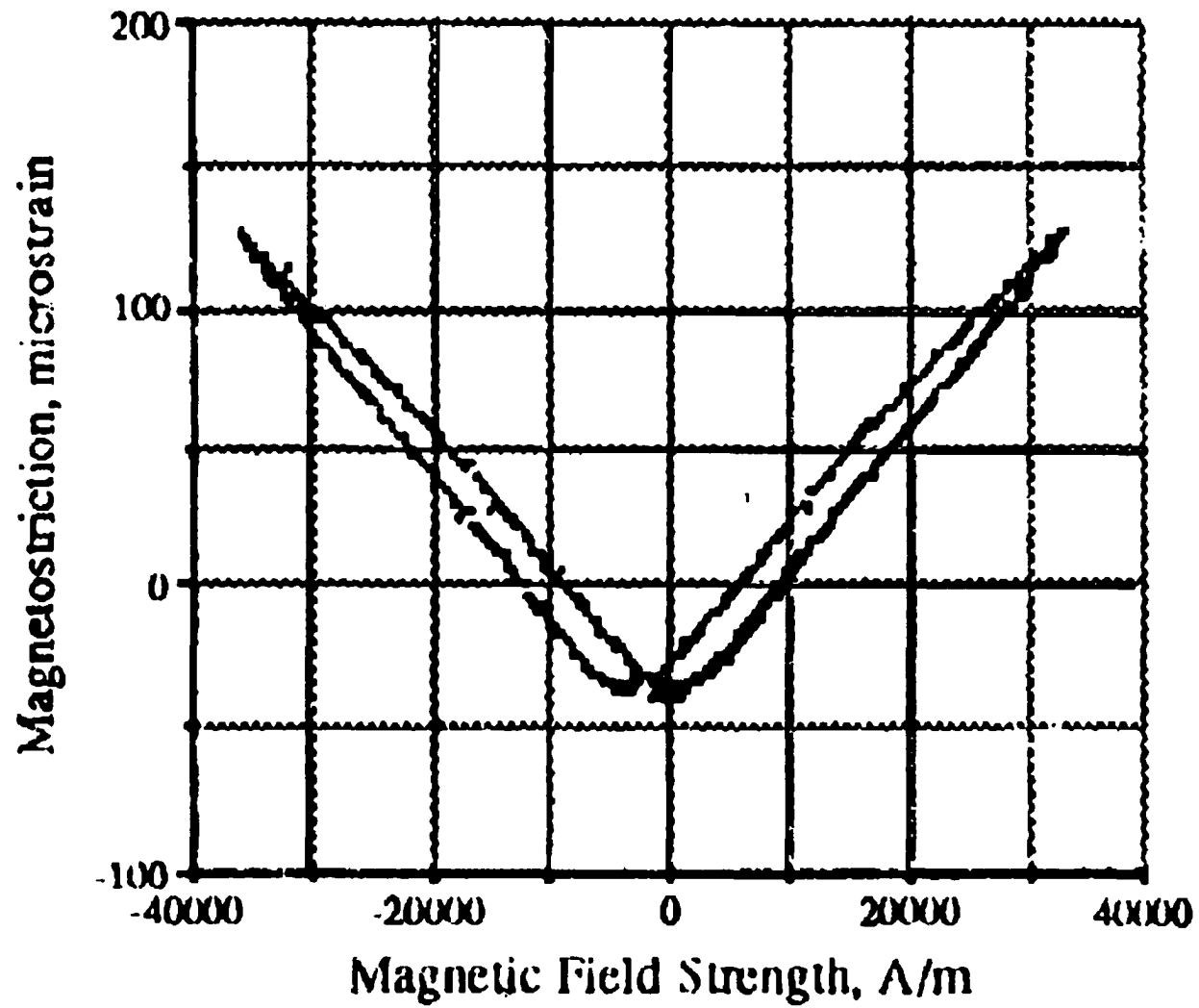


Figure 2.7 Plot of dc magnetostriction of a Terfenol-D rod versus applied field strength. The measurement was obtained with a strain gauge attached to a Terfenol rod and the dc magnetic field was generated by an electromagnet.

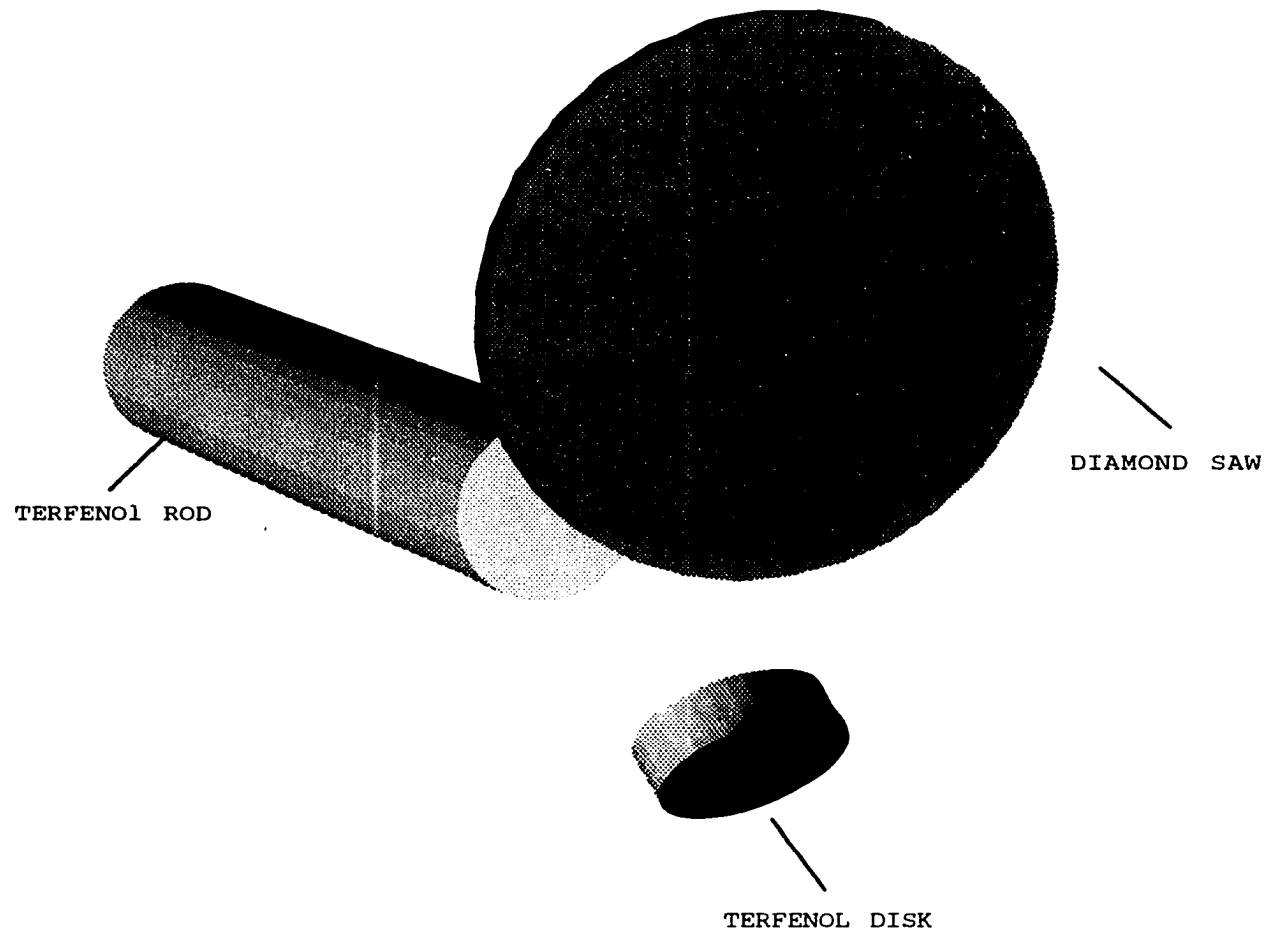


Figure 2.8 Schematic diagram showing the application of a diamond saw in slicing the Terfenol-D material.

processing technique, such as chemical etching, was applied to the sample. Nevertheless, an etching technique is expected to provide a better surface finish in a manufactured device. Since the mechanical cutting procedure inevitably damaged some of the surface structure of the material, an electric-arc cutting or chemical cutting methods would be preferred for a high performance application.

Unlike a conventional magnetic biasing scheme with a closed magnetic circuit, the 1 mm thick Terfenol-D disk is biased by the fringing field of the magnet, which was tightly coupled to the Terfenol-D disk with epoxy. A Hall sensor was used to evaluate the gradient of the fringing field prior to assembly. The normal component of the fringing field decreased by 20% at a distance of 1.5 mm from the surface. It should be noted that a disk shaped transducer possesses a large demagnetization factor.

3. PROTOTYPE EVALUATION

3.1 Introduction

This chapter describes the research undertaken to evaluate the performance of the device. A HeNe heterodyne interferometer was used to investigate the performance of the biased Terfenol-D module. The operating principle of the interferometer is discussed by Monchalin [6] and reviewed in Appendix A. The experimental setup is shown in Figure 3.1. The transducer assembly was fixed to a XY stage and placed inside a solenoid. The sample was excited with an ac magnetic field. Spatial scans over the surface of the Terfenol-D were obtained from 30 Hz to 20 kHz. The results of selected excitation frequencies are shown in Figure 3.2, Figure 3.3 and Figure 3.4. The cross sectional view of various excitation frequencies is shown in Figure 3.5. A summary of the findings was reported by Shultz, et. al. [7].

3.2 Interferometer Measurement Results

In general, the experimental results revealed a non-uniform displacement of the sensor material and significant movement occurred at the edge of the sensor disk and the center of the material. We postulated that the non-uniform distribution of the displacement was a manifestation of eddy current effects. As a result, a significant amount of magnetostriction was observed along the perimeter of the sample. The movement that occurred in the center of the sample could be a result of either Lorentz force or magnetoelastic deformation. Similar to the operating principle of Electromagnetic Acoustic Transducer (EMAT) pioneered by Bruce Thompson of CNDE, a Lorentz force is generated as a result of the dc magnetic bias and the eddy current persisted around the perimeter of the sample. The Lorentz force

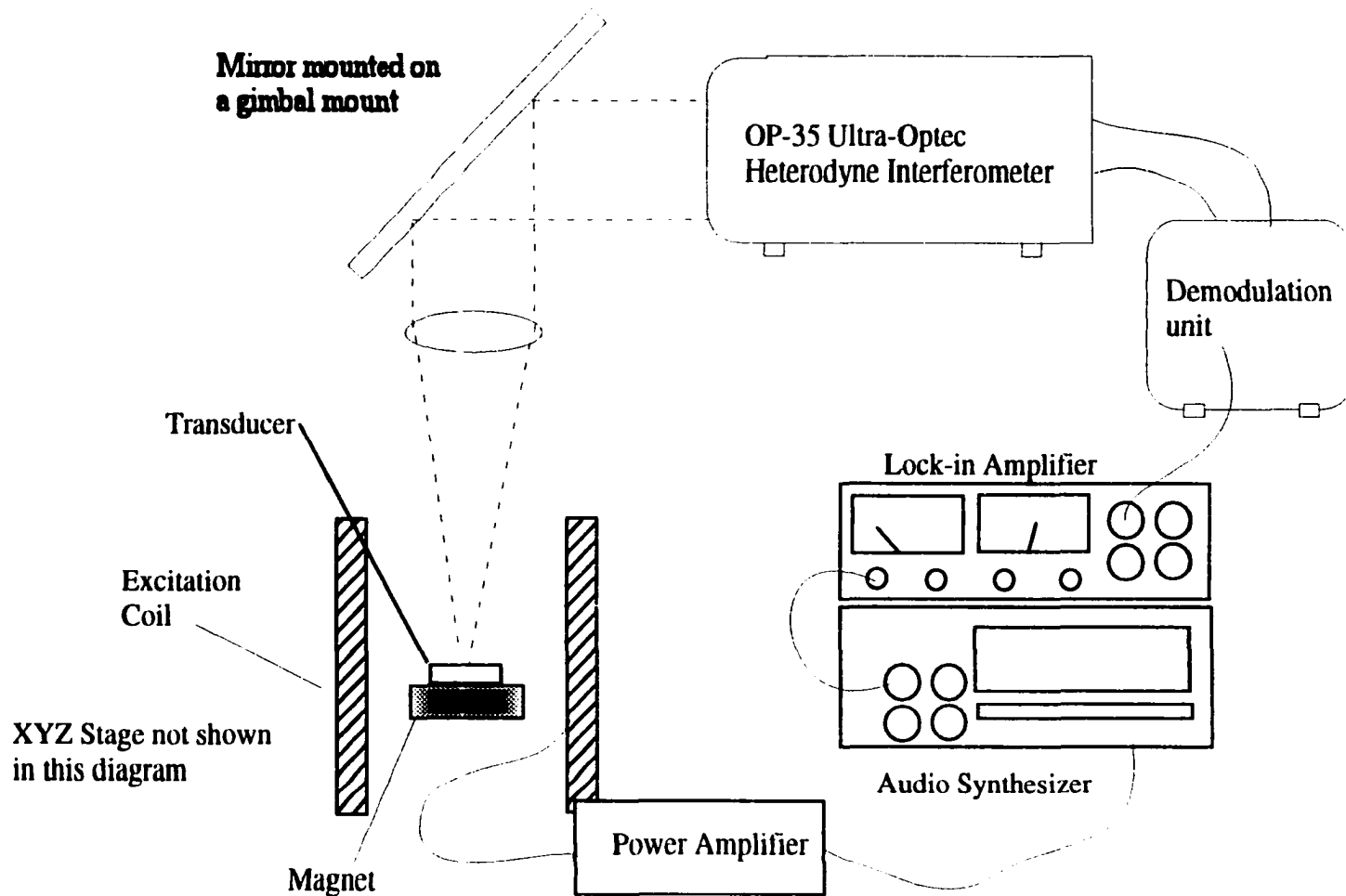


Figure 3.1 Experimental setup for transducer disk evaluation using a heterodyne interferometer capable of nanometer resolution. A solenoid coil is used to excite the transducer under test and the demodulated output of the interferometer is detected with an amplifier for synchronous detection. The data is collected via a desktop computer.

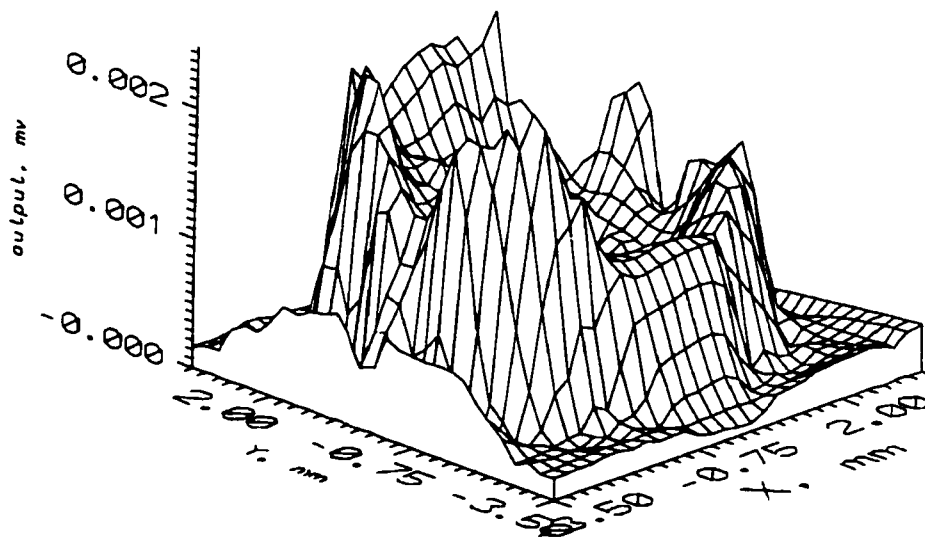
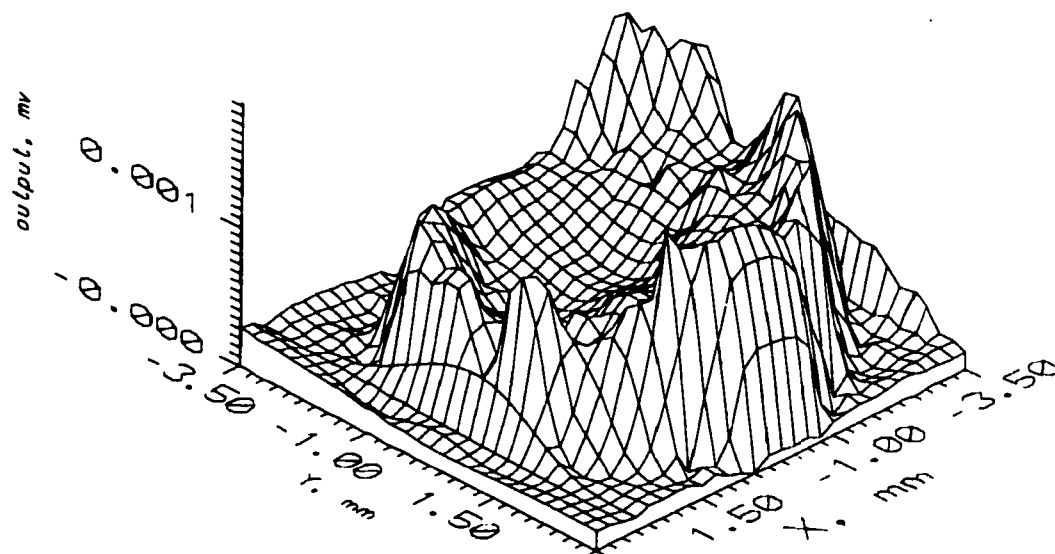


Figure 3.2 Different views of spatial scan results of a Terfenol-D disk with a heterodyne interferometer under an ac field excitatin 19 kHz.

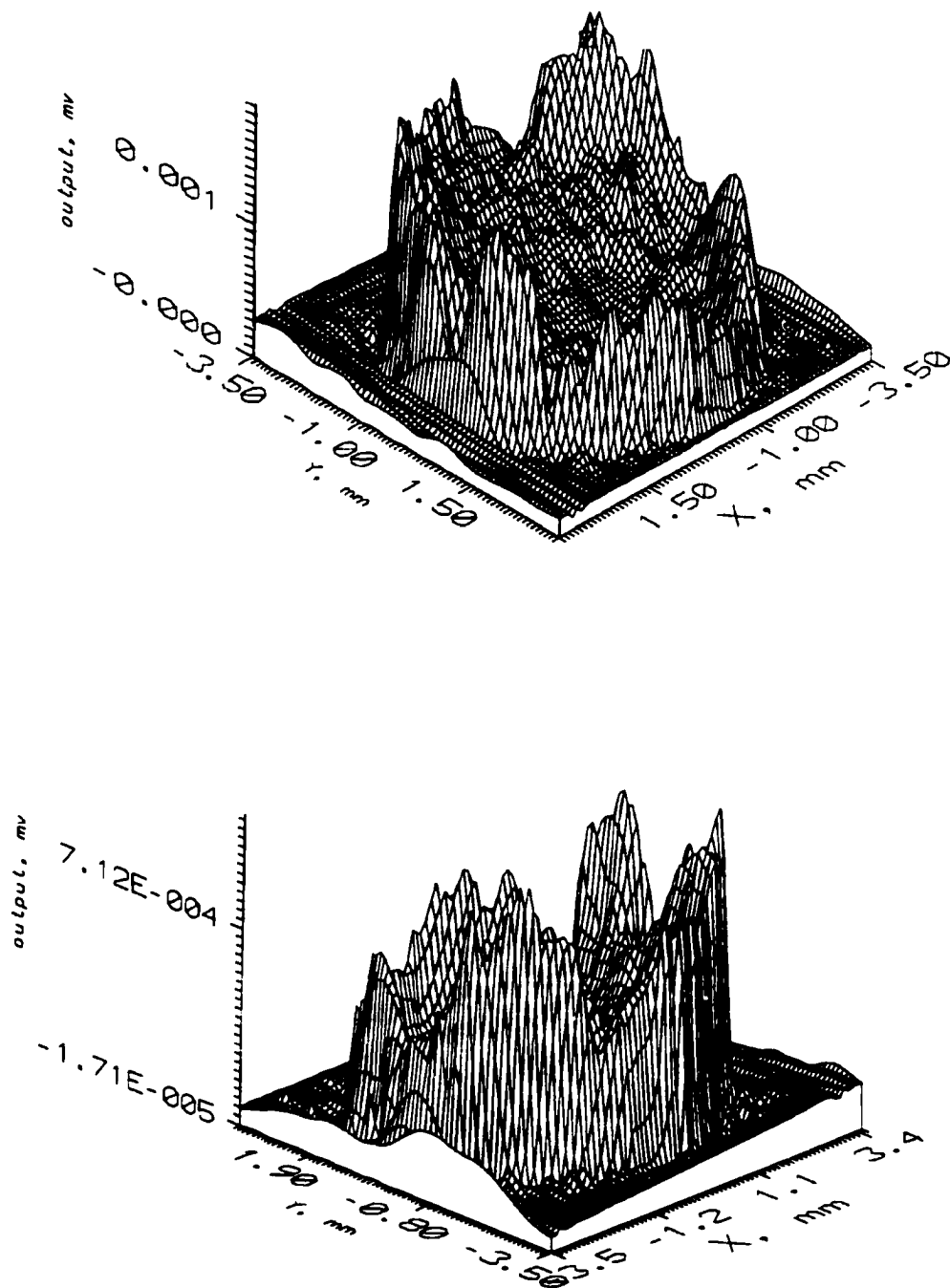


Figure 3.3 Different views of spatial scan results of a Terfenol-D disk with a heterodyne interferometer under an ac field excitatin 45 kHz.

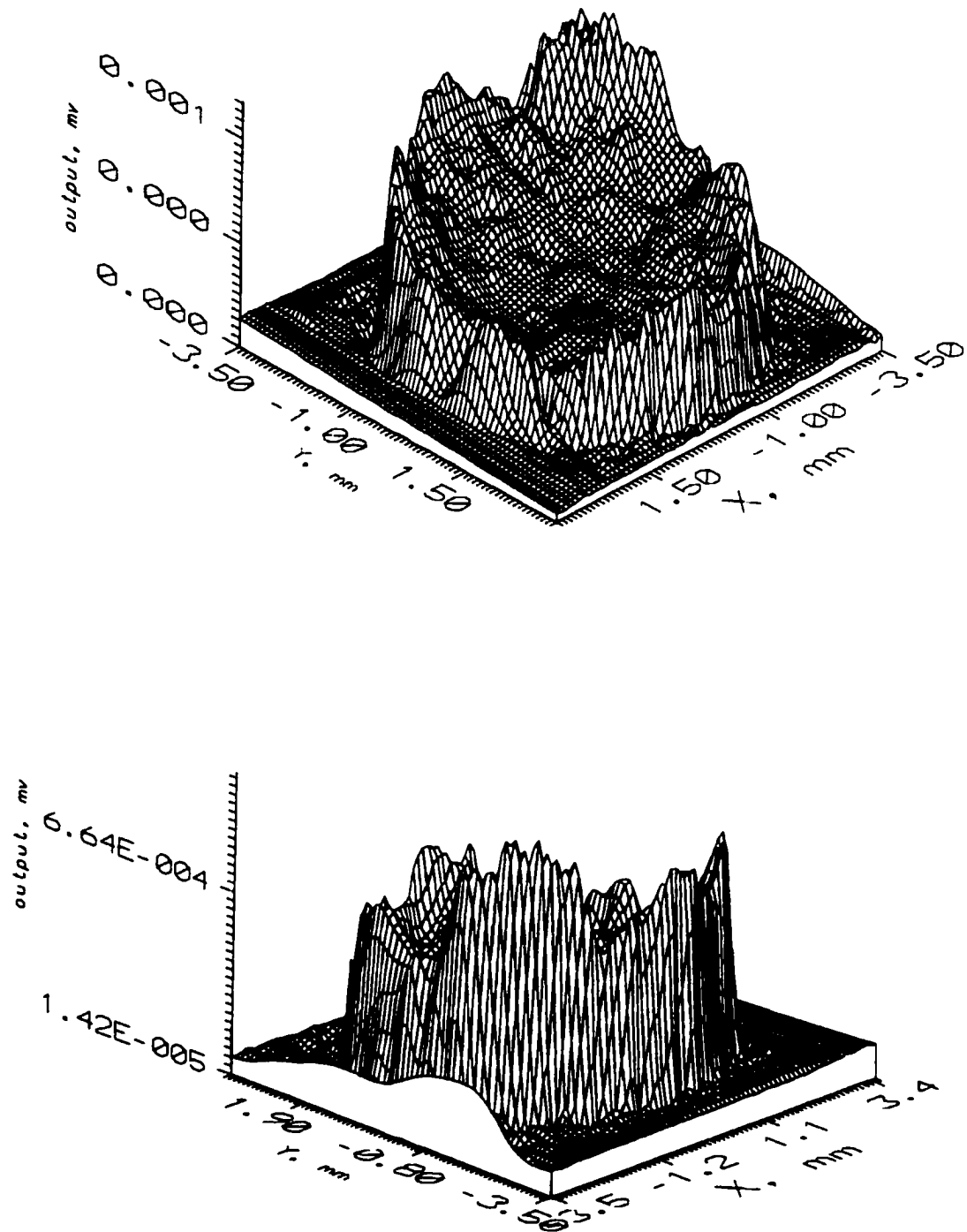


Figure 3.4 Different views of spatial scan results of a Terfenol-D disk with a heterodyne interferometer under an ac field excitatin 60 kHz.

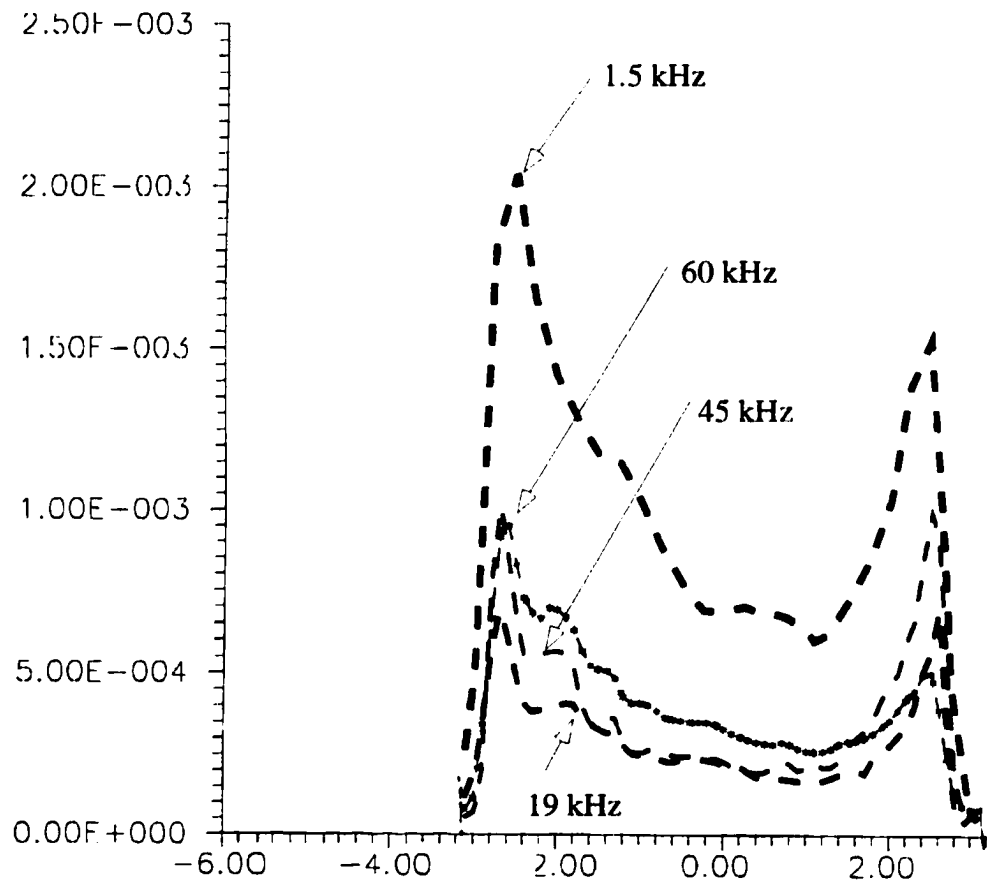


Figure 3.5 Cross-sectional views of spatial scan results of a Terfenol-D disk with a heterodyne interferometer under an ac field excitation at various frequencies.

was directed radially inward and caused the inner portion of the material to protrude normal to the surface. Alternatively, the sample may vibrate in a specific mode determined by the boundary conditions and the loading of the sample. The origin of this non-uniform surface deformation requires a detailed analysis of the elastodynamical properties of the transducer material and geometry.

3.3 Alignment of the Transducer Module with the Diode Laser Sensor

Incorporating the transducer module with the diode laser sensor was a difficult task because a good optical alignment (i.e., tight coupling) between the laser facet and the Terfenol-D disk was required. A misaligned transducer module caused a decline in the performance due to the excessive diffraction loss as light transversed back and forth within the external cavity. As shown in Figure 3.6, there are three critical parameters in this alignment procedure: (a) the coupling distance between the diode facet and the Terfenol-D disk, (b) the rotation angle between the outward normal of the facet and the Terfenol-D disk in the x - z plane, and (c) the rotation angle between the outward normal of the facet and the Terfenol-D disk in the y - z plane. Three different techniques for aligning the transducer with the diode laser facet were investigated.

3.4. Mechanical Translator Assisted Method

With a micrometer based xyz translation stage, rotator, and tilting stage, the transducer module can be aligned with great precision. The alignment process was monitored with a high-power microscope. As shown in Figure 3.7, the transducer module was mounted onto a right-angle bracket extending from the translator assembly. Then, the transducer

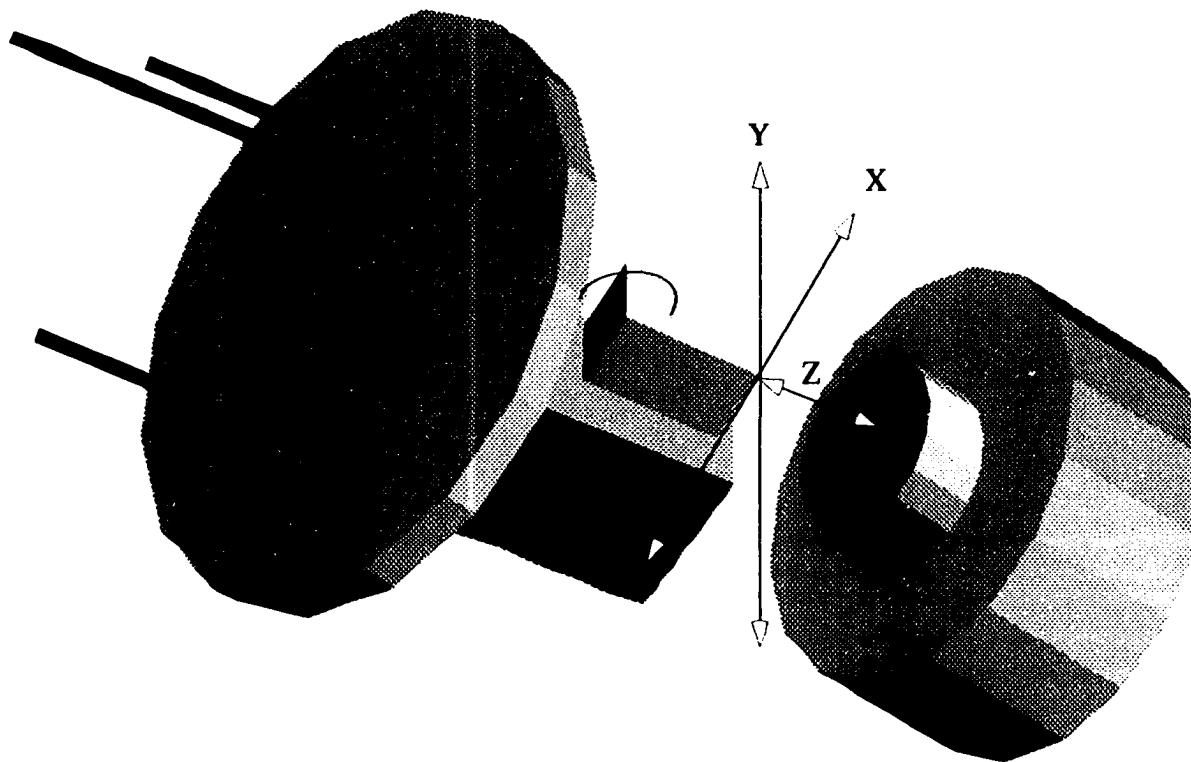


Figure 3.6 Schematic diagram showing the critical alignment parameters for the diode laser external cavity sensor and the Terfenol transducer. These are the coupling distance and the angles between the XZ axis and the YZ axis.

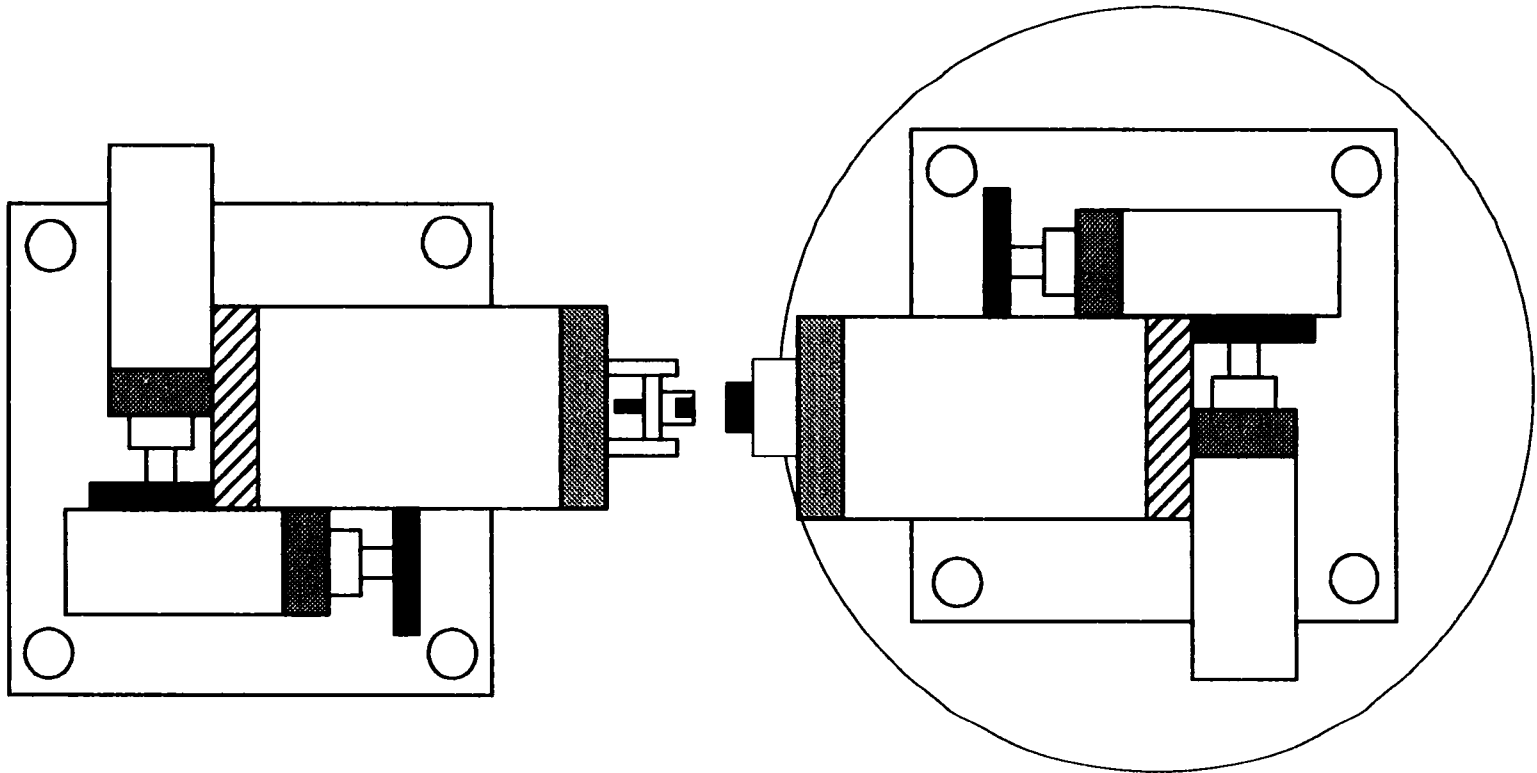


Figure 3.7 One of the alignment techniques used in adjusting the coupling angle and position between the magnet assembly and the sensor.

module was locked with set screws and bonded into place after it had been aligned using epoxy adhesive. This technique has been tried with a Newport XYZ table equipped with a tilting stage and 1 micrometer resolution, and an Oriel rotator. The position of the transducer, relative to the diode laser facet, could not be stabilized and a steady drift in the output was observed. Moreover, the limited resolution on the micrometer head cannot provide the desired accuracy and repeatability. In addition, the tilting stage had a backlash problem rendering it unusable in this application. This technique was later repeated with a ultra-high resolution micrometer head (Newport 0.2 differential micrometer resolution) and the results were still unsatisfactory due to its poor repeatability [8].

3.5. Iterative Adjustment Method

This method does not provide as much control as the previous technique. An extra brass socket (or sleeve) was machined and used as a support for the transducer module. By inserting the transducer module into the sleeve, the outward normal of the Terfenol-D disk was made perpendicular to the diode facet if (1) the ceramic magnet is a perfect cylinder or thick disk, (2) the Terfenol-D disk is also a perfect cylinder and (3) the bonding between the Terfenol-D and the magnetic does not introduce a tilt. The schematics of the brass sleeve with the transducer module in place is shown in Figure 3.8. The transducer module is temporarily fixed by the friction between the inner wall of the brass sleeve and the edge of the ceramic magnet. The lower edge of the sleeve was then bonded onto a substrate using epoxy adhesive. A microscope slide was used in this application.

The magnet-Terfenol sensor assembly was positioned in the upper portion of the brass sleeve as shown in Figure 3.8. The aluminum housing, with the diode laser installed, was inserted as shown. A tight coupling was achieved as the diode laser was pushed against the

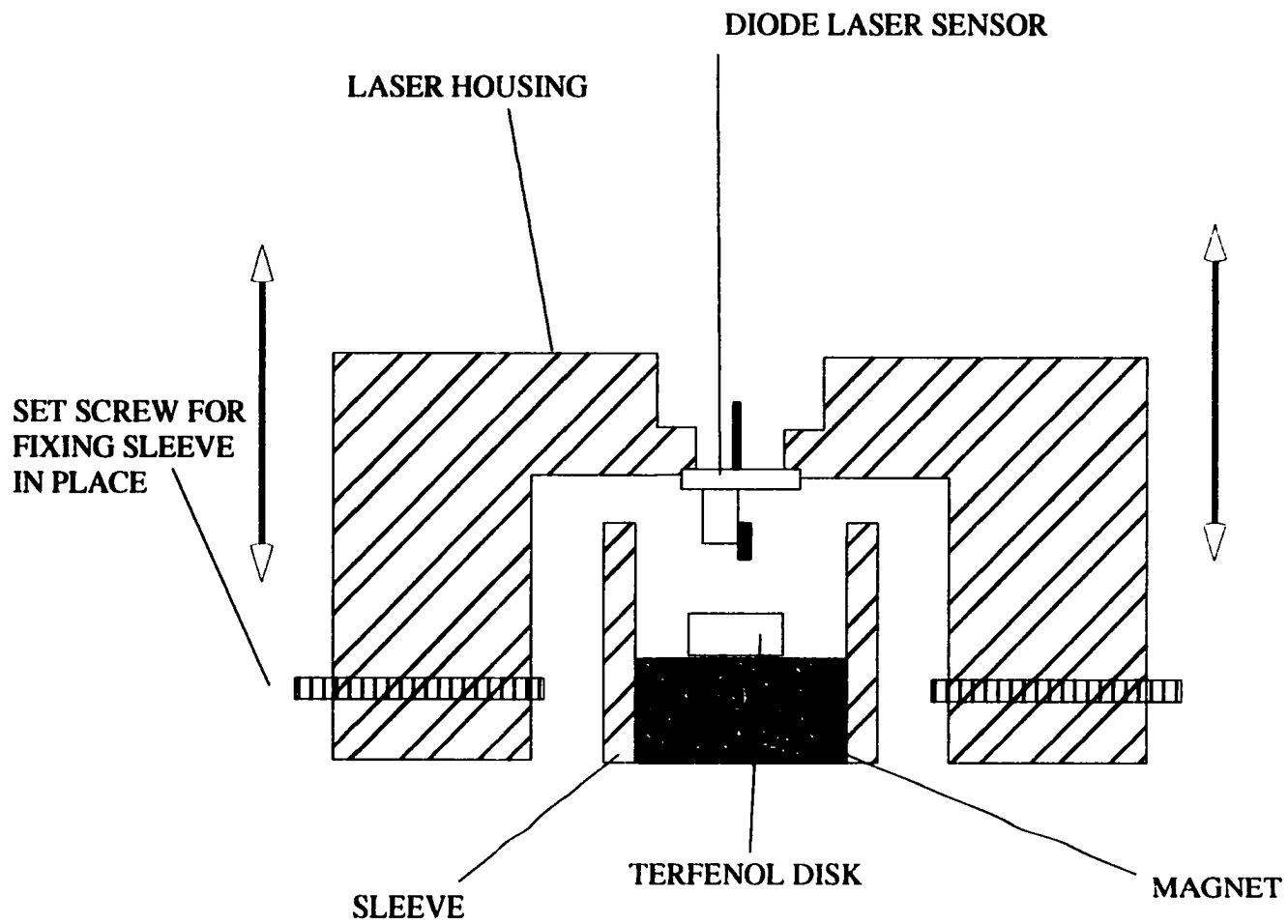


Figure 3.8 Schematic illustrating the iterative alignment technique for aligning the transducer assembly.

transducer. A thin piece of non-abrasive material, such as a 0.025mm lens paper, was placed between the Terfenol-D disk and the diode laser to prevent any damage to the surface of the laser during the installation. The diode laser chip may crack in this process and the procedure had to be repeated to obtain the best result. The entire assembly was finally held together by epoxy.

Both a high-power microscope and the dc response of the diode laser were used to evaluate the quality of the alignment after the epoxy cured. It should be mentioned that the performance of the sensor might drift during the curing period. The installation was considered a success when the sensor demonstrated satisfactory ac response. Although this iterative process was costly and time consuming, satisfactory results were obtained using this method. The laboratory prototype used in this thesis was produced using this technique.

3.6. Closed-loop Alignment Method

The result of the above techniques was operator dependent. Thus, they are not really suitable for use in a manufactured device. A closed-loop control system for controlling the coupling is desired. For example, the three micrometers for controlling three orthogonal axes can be replaced by a piezoelectric translator. The movement of the transducer could be controlled by a desktop computer. Although an electrical translator system is able to provide a high degree of precision in the alignment process, the sequence of aligning the sensor must be studied in detail. It is especially important to investigate if there is a local minimum in the three dimensional alignment error function.

3.7 Performance Evaluation of the Magnetometer Prototype

The performance of the sensor was evaluated with the experimental setup as shown in Figure 3.9. The diode laser was biased at 40mA with a constant current source. The sensor module was placed inside a coil. The current-to-field conversion ratio was calibrated as 1.23 A/m (15 mOe) per milliamp. The intensity of the test field was varied from 2 A/m (25 mOe) to 33 A/m (420 mOe) at selected frequencies ranging from 70 Hz to 20 kHz. The response of the sensor was recorded with a 12 bit analog-to-digital card and was monitored with an audio spectrum analyzer and a lock-in amplifier. The sensor output versus the magnitude of excitation current to the coil and frequency are plotted in Figure 3.10. In general, the sensor module demonstrated a highly linear response throughout most of the testing range. However, we also observed that the linearity of the module declined when the intensity of the test field was small (i.e., less than 5 A/m or 62 mOe). Although no testing was performed below 70 Hz, the device is expected to perform in the sub-Hz level.

The frequency response of the sensing module was also studied by applying a constant ac magnetic field from 70 Hz to 20 kHz. The response of the module to constant ac magnetic fields declined linearly with frequency as indicated in Figure 3.11. This implied that the module would be more sensitive to excitation at low frequency than to excitation at high frequency. Problems associated with this trend can be equalized by software. In addition to examining the frequency response, the signal-to-noise ratio (SNR) of the module was investigated. The signal-to-noise ratio is depicted in Figure 3.12. A decline in the signal-to-noise ratio was observed as the excitation frequency increased.

These results clearly demonstrated the ability of the module to detect ac magnetic fields from 70 Hz to 20 kHz. The performance of the device below 70 Hz can be extrapolated from the Figure 3.12. Although 60 Hz magnetic fields is of prime interest in personal

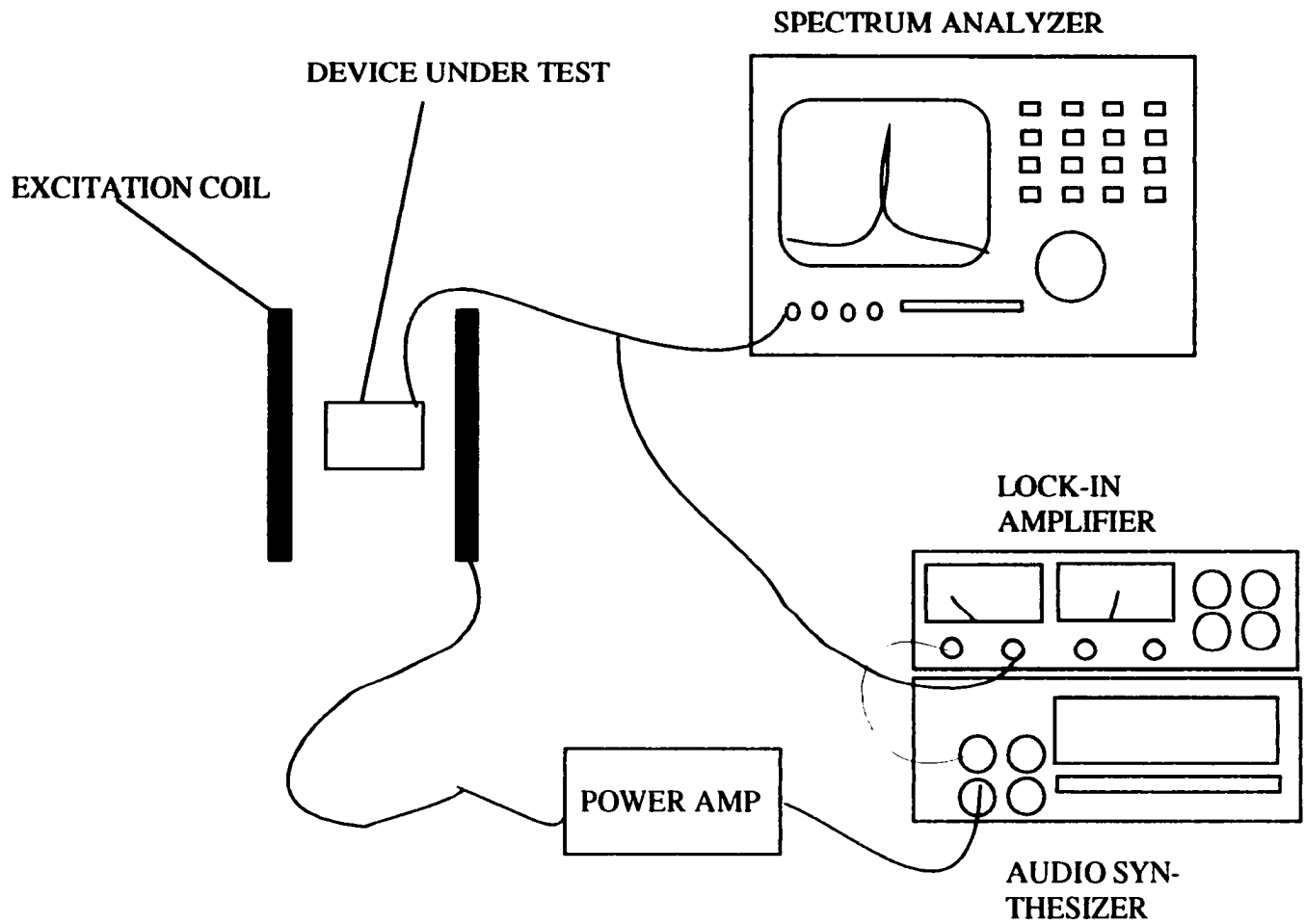


Figure 3.9 Experimental setup for evaluating the performance of the sensor module. Both a lock-in amplifier and the spectrum analyzer are used to determine the signal strength, signal-to-noise ratio, and presence of spurious harmonics.

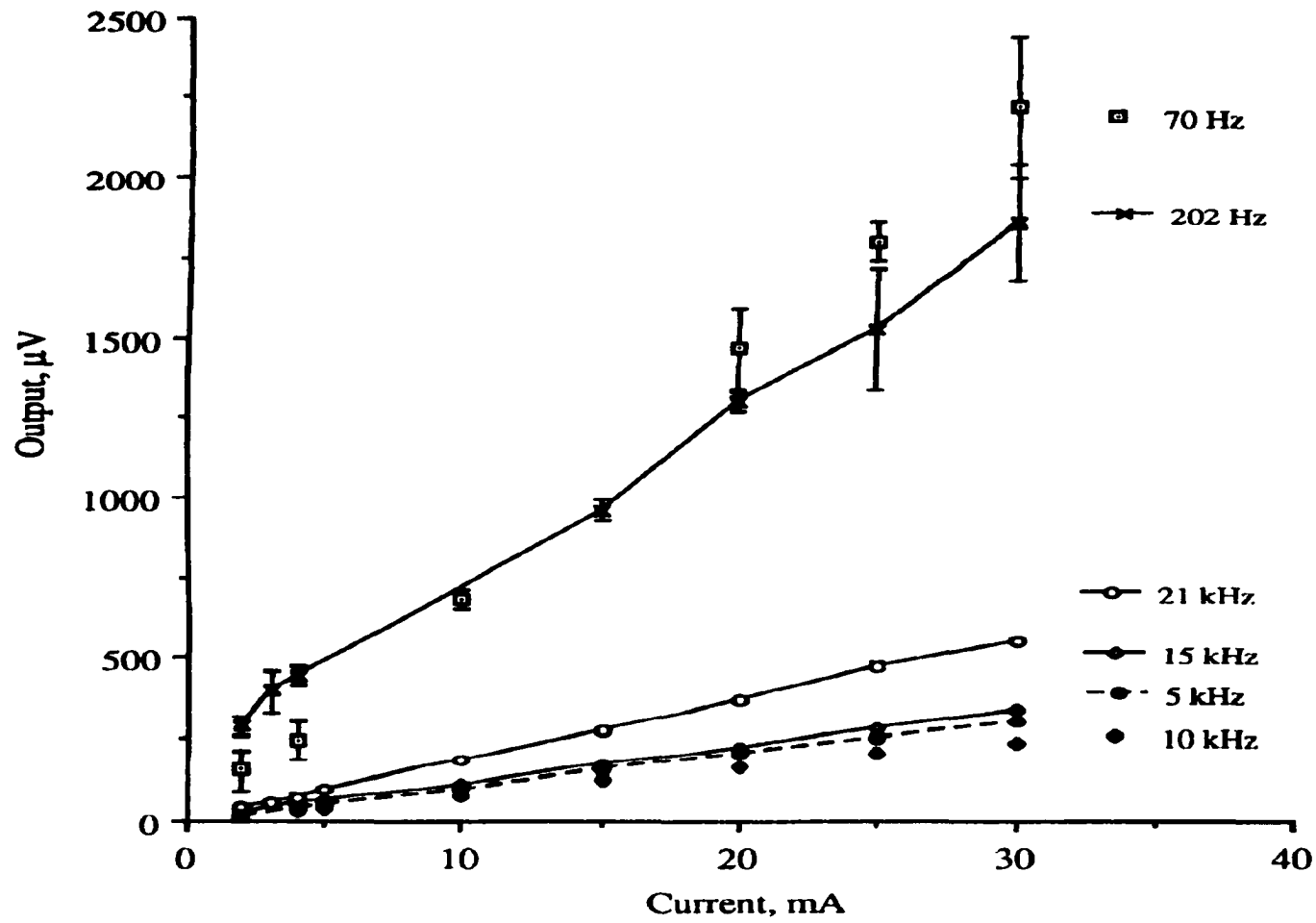


Figure 3.10 Magnetometer response as a function of excitation current with various excitation frequencies.

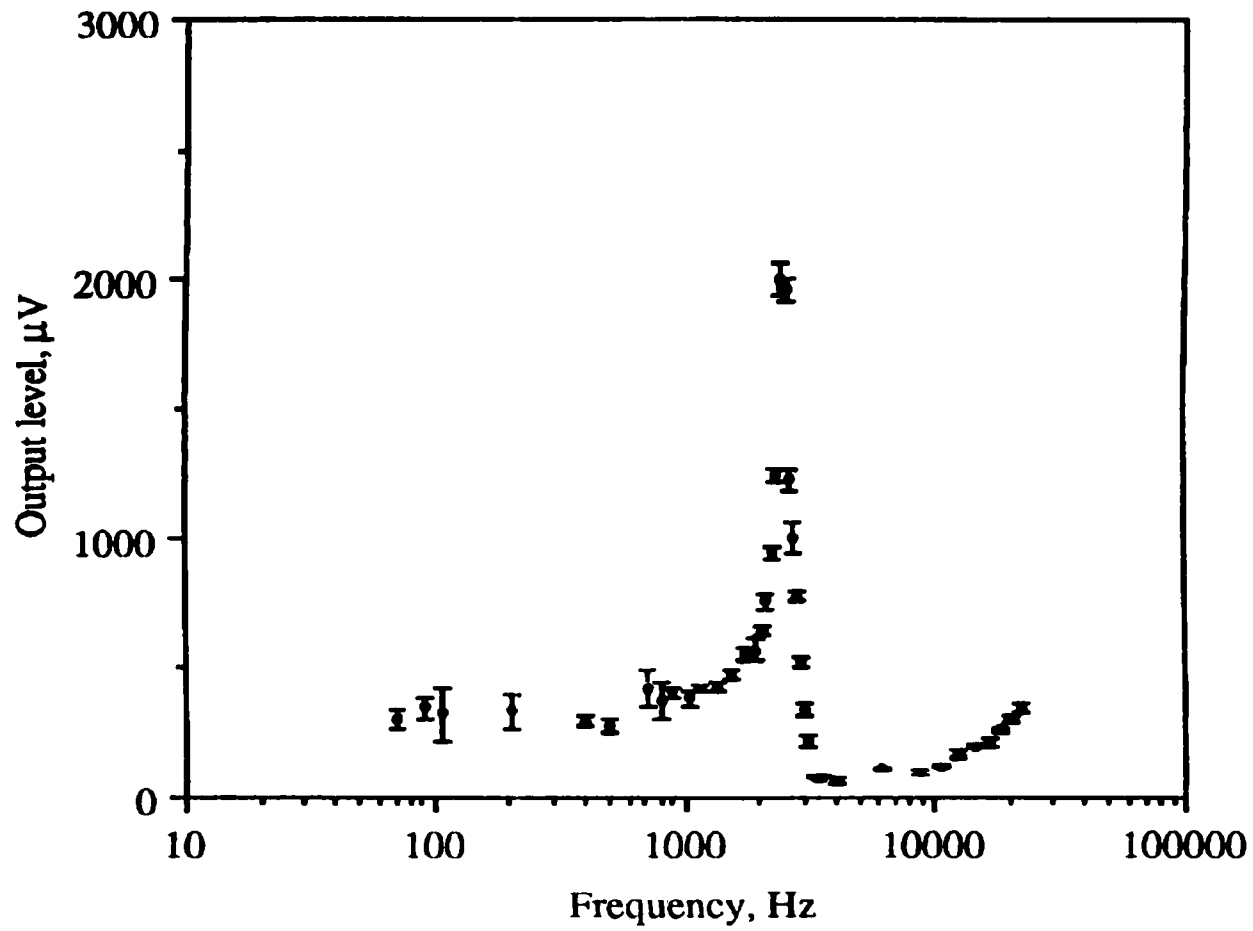


Figure 3.11 Frequency response of the prototype magnetometer with a fixed level of field excitations. A resonance peak is observed.

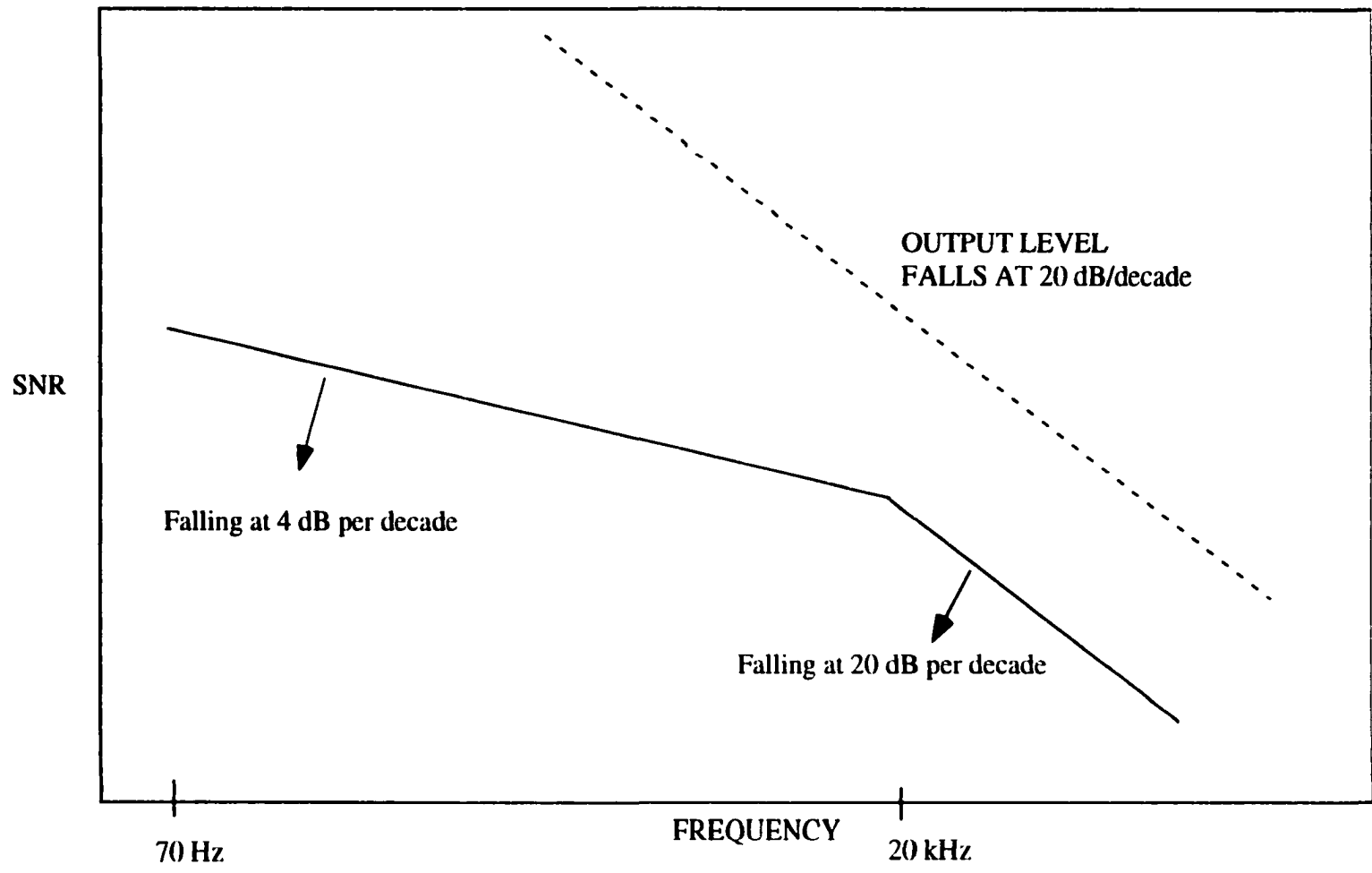


Figure 3.12 Frequency response of the prototype magnetometer signal-to-noise ratio on a log-log scale plot.

dosimeter application, 70 Hz was chosen as the evaluation frequency to avoid pick-up problem. A proper calibration procedure is required if a quantitative comparison between measurements at different frequencies is desired. Further detail on the calibration process of the unit will be discussed in Chapter 7. A brief description of the microcontroller unit is provided in Appendix F.

3.8 An Alternative Housing Design for the Sensor

The previous housing design does not allow convenient registration between the diode laser facet and the Terfenol transducer material. A self-aligning scheme, limited by the resolution of the machining tolerances, can be used instead. A schematics demonstrating the idea of the design is shown Figure 3.13.

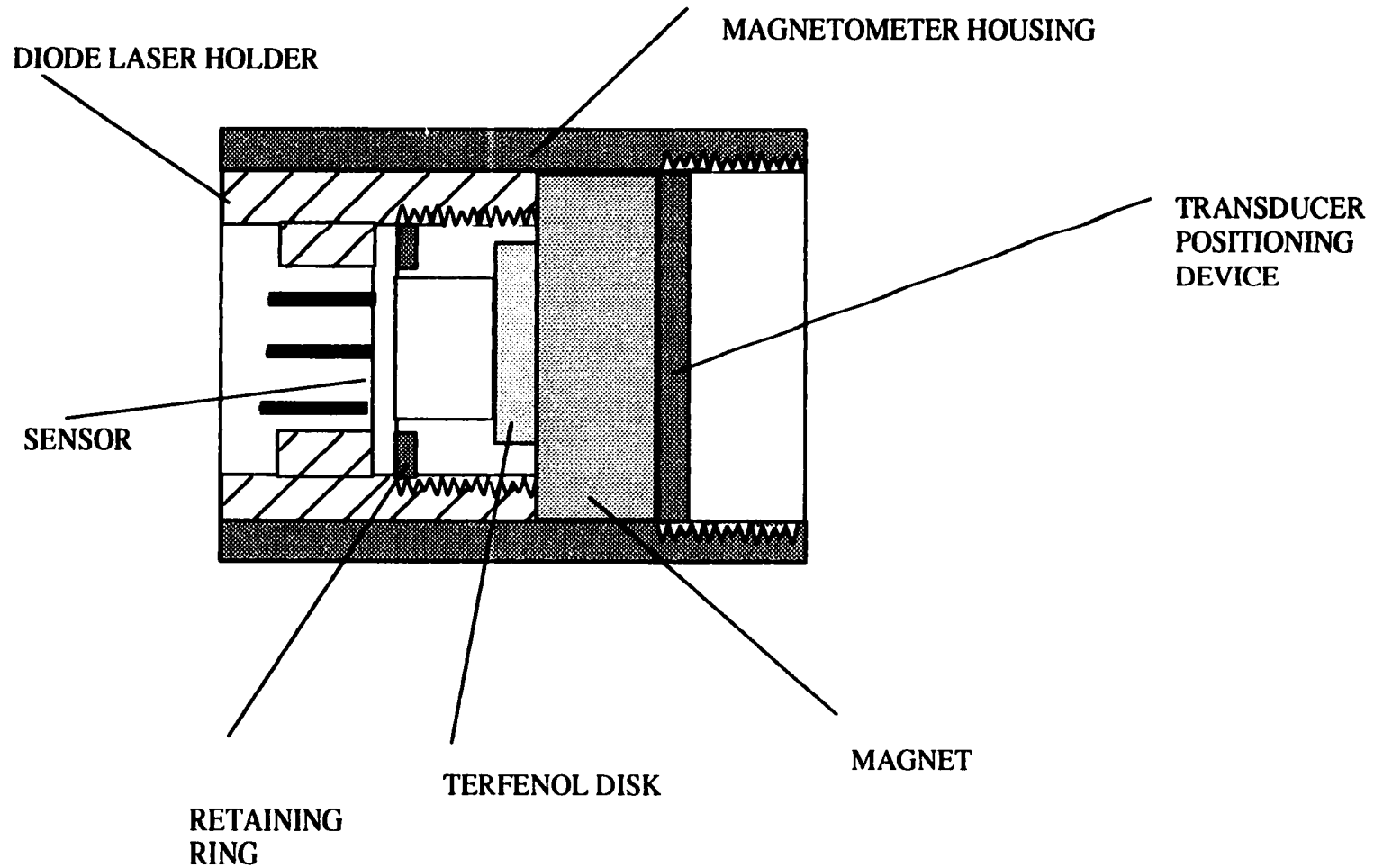


Figure 3.13 Schematic showing an improved design on the magnetometer housing. This design will aid the alignment process by using a tubular structure and by introducing a fine threaded inner core for adjustment between the diode laser holder and the transducer.

4. ANALOG SUPPORTING ELECTRONICS

4.1 Introduction

The operation of the diode laser sensor requires a low-noise current supply, a transient protection circuit and a low-noise photodetector pre-amplifier. This chapter describes the functions and a few design issues concerning the analog signal processing circuitry.

This chapter is divided into three sections: Section 4.2 describes the function of the photodetector amplifier, various circuit topologies, and design issues. SPICE simulations of the performance of the amplifier are provided. A dc nulling scheme to maximize the dynamic range is presented. Section 4.3 discusses the function of the diode laser current driver. Section 4.4 discusses design issues, such as stability and noise sources. SPICE simulation on the performance of the diode laser driver are presented. Moreover, a few circuit ideas for protecting the diode laser from current or voltage transient are described. The performance of these proposed protection circuits are presented.

4.2 Photodetector Pre-Amplifier

The photodetector amplifier converts the optical signal to an electrical signal for further processing. It is one of the most important analog components in the magnetometer prototype since its performance directly affects the overall sensitivity of the system. In the prototype device, we used the monitoring photodetector, which is likely to be used in future production, housed with the diode laser. Therefore, the following analysis assumes the typical specifications of a monitoring photodetector of a ML-4403 diode laser (see Appendix B).

In general, the manufacturer does not optimize the performance of the monitoring photodetector, which usually has a higher level of dark current and larger junction capacitance with respect to some high-end stand alone photodetector diodes. Consequently, the bandwidth of the system will be limited. However, this will not limit the performance of the sensor. When a higher measurement bandwidth is required, some manufacturers provide a high performance photodetector at a higher cost [9]. The performance of the photodetector amplifier is usually judged by its measurement bandwidth, signal gain or sensitivity, SNR and dynamic range.

4.3 Detection Schemes

The photodetector can be operated in a photovoltaic mode or a photoconductive mode. Photoconductive detectors produce a current in response to incident light, whereas photovoltaic detectors generate a voltage in response to the incident light. In other words, the photovoltaic detector operates in an open circuit mode while the photoconductive detector operates in a short circuit mode. The former can be realized by connecting the diode directly to the input of a voltage amplifier and the latter can be implemented by connecting the diode to a current amplifier. In practice, a transimpedance amplifier is frequently used to convert the photodiode current to an output voltage. A typical transimpedance op-amp circuit is shown in Figure 4.1. In this circuit, the op-amp drives the inverting input to virtual ground by providing a current equal to the photodetector current through the feedback resistor. The output voltage is therefore:

$$V_{OUT} = -I_{PD} * R_f \quad (4.1)$$

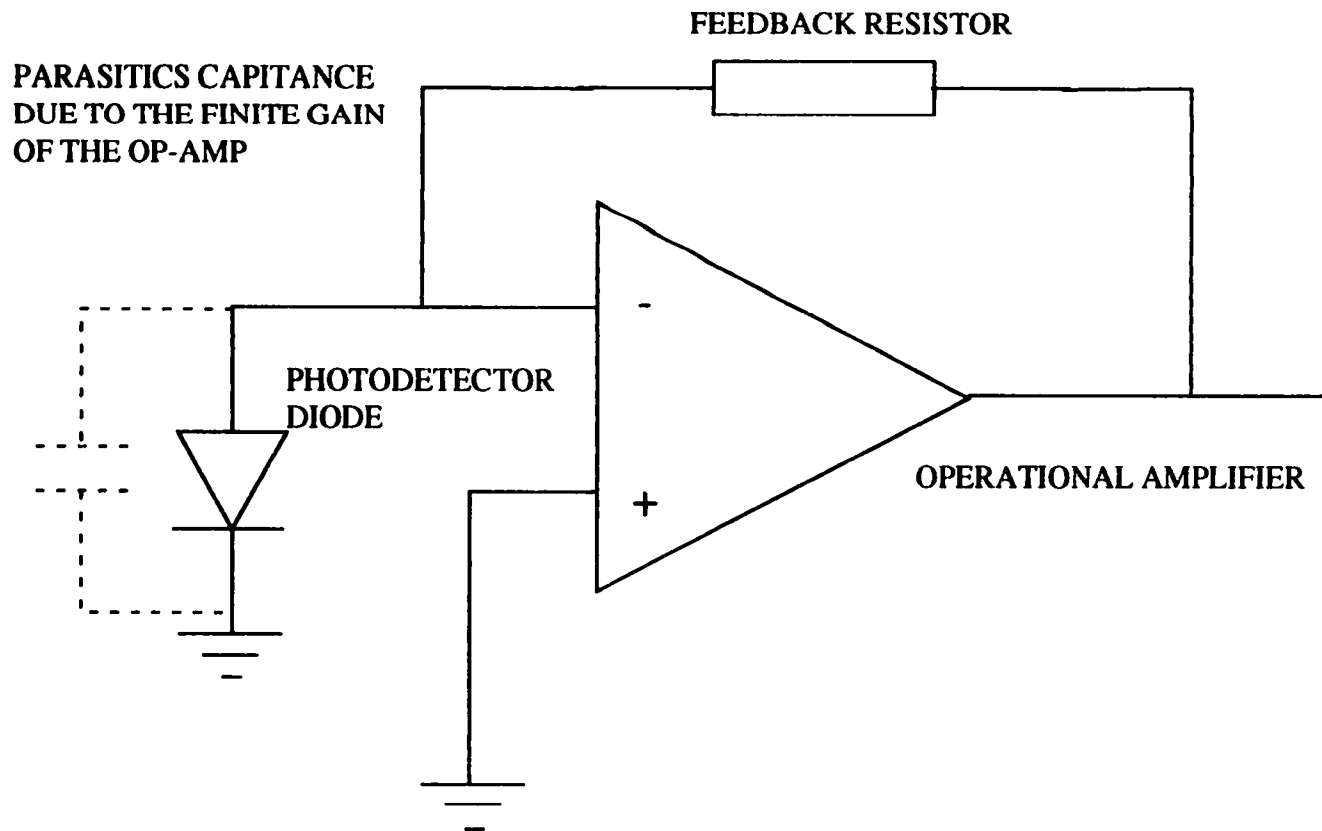


Figure 4.1 Schematic diagram of a transimpedance amplifier consists of a non-ideal operational amplifier. The finite gain of the amplifier fails to remove the diode capacitance which imposes a feedback pole on the system, causing potential instability.

where V_{out} is the output voltage of the amplifier, I_{pd} is the photocurrent generated by the photodetector in response to an optical input, and R_{f} is the feedback resistor.

While the measurement bandwidth of the photovoltaic mode is limited by the diode capacitance, the transimpedance configuration provides signal isolation to the photodetector so that the effect of the diode capacitance on measurement bandwidth is minimized. In addition, the virtual ground property of an operational amplifier provides an effective short circuit to the load of the photodiode thus preventing the development of a forward bias voltage. Nevertheless, the op-amp's finite open-loop gain limits the isolation performance of the pre-amplifier and the diode capacitance shunts away the signal current at high frequency, placing a limit on the system bandwidth. As the value of the diode capacitance increases, the presence of a feedback pole (see Figure 4.1) in the transimpedance amplifier can no longer be ignored and a detailed examination of optimal noise performance and stability of the system is required.

4.4 Design Issues

4.4.1 Amplifier gain

The gain of the transimpedance amplifier is determined by the value of the feedback resistor. The output voltage of the amplifier increases linearly with the feedback resistor. Thus, the sensitivity of the transimpedance amplifier improves when a large feedback resistor is employed. Nevertheless, when the measurement involves a considerable amount of dc signal, the dynamic range of the system prohibits a large feedback resistor from being used. Automatic gain control, or other techniques, must be applied to improve the performance of the system.

The detail of a simple dc nulling scheme will be discussed in the following section. It should be noted that any transimpedance amplifier should use the highest feedback resistance tolerable since the measurement SNR increases as the square root of R_f . The detail of the noise performance of the transimpedance amplifier will be discussed. Most resistors, especially those with high resistance, are capacitive. Thus, a feedback zero will be introduced as a result of the above parasitic capacitance, which complicates the noise analysis of the transimpedance amplifier. When an extremely high feedback resistance is required, a T-network is usually employed to replace a hard-to-find resistor in the hundreds of mega-ohm range.

It should be noted that a careful construction technique is required when an extremely high impedance feedback resistor is employed. A teflon standoff is often used to isolate the feedback resistor from the printed circuit board to avoid stray capacitance and leakage current. Furthermore, the circuit should be protected from moisture to ensure reliable operation.

4.4.2 Stability and phase compensation

The finite open loop gain of the op-amp puts part of the output voltage (i.e. $V_{out}/open$ loop gain) across the input. As a result, the effect of the input capacitance of the op-amp associated with the presence of a photodiode and the resultant phase alteration cannot be ignored as the open loop gain decreases with frequency. Figure 4.1. illustrates the effect of the input capacitance on the performance of a transimpedance amplifier. The feedback resistor and the input capacitance form a single pole filter in the feedback path of the circuit. Phase delay of this low-pass filter reduces the op-amp phase margin. With a large feedback resistor, instability may occur. The effect of this feedback pole can be cancelled by introducing a feedback zero by putting a bypass capacitor across the feedback resistor.

The stability of the amplifier can be analyzed using feedback plots. This is depicted in the Bode plot of Figure 4.2, which shows the interaction between the open loop gain of the operational amplifier and the reciprocal of the feedback factor (i.e. the reciprocal of the fraction of the output signal feedback to the input). The feedback network determines the amount of feedback and is usually configured as a voltage divider network in a purely resistive case or a filter network in a more general case. The loop gain of the system is defined as the difference of ordinates A and $1/b$ on the logarithmic scale, where A is the open loop gain and b is the feedback factor.

Since the $1/b$ line represents the feedback demand, closed loop requirements will be satisfied as long as this line is below the amplifier gain curve. When this condition is no longer true, the actual response drops, following the amplifier open loop response downward. For most single pole operational amplifier, the rate of descent is 20 dB per decade. The intercept point between the $1/b$ curve and the open loop gain curve indicates a key characteristics of the system: the stability of the amplifier. Since the closed loop gain at the intercept point is 1, a 180 degree phase shift will cause the system to oscillate. Thus, the feedback factor and the open loop gain plot serves as a quick diagnostic tool for system stability.

The closed loop response of an uncompensated transimpedance amplifier of the amplifier being used shows a peak in the closed loop response. This is commonly known as "gain peaking". It is a result of the feedback zero of the input capacitance. The feedback factor of the system behaves as a high pass filter and may rise up at 20 dB per decade. When the feedback factor curve intercepts the open loop gain curve of the amplifier, the stability of the system reaches a critical point of zero phase margin. Any additional phase shift causes the system to go into oscillation. The problem can be solved by a proper choice of the bypass capacitor connected across the feedback resistor.

For a unity-gain stable operational amplifier, the compensation capacitor for a 45

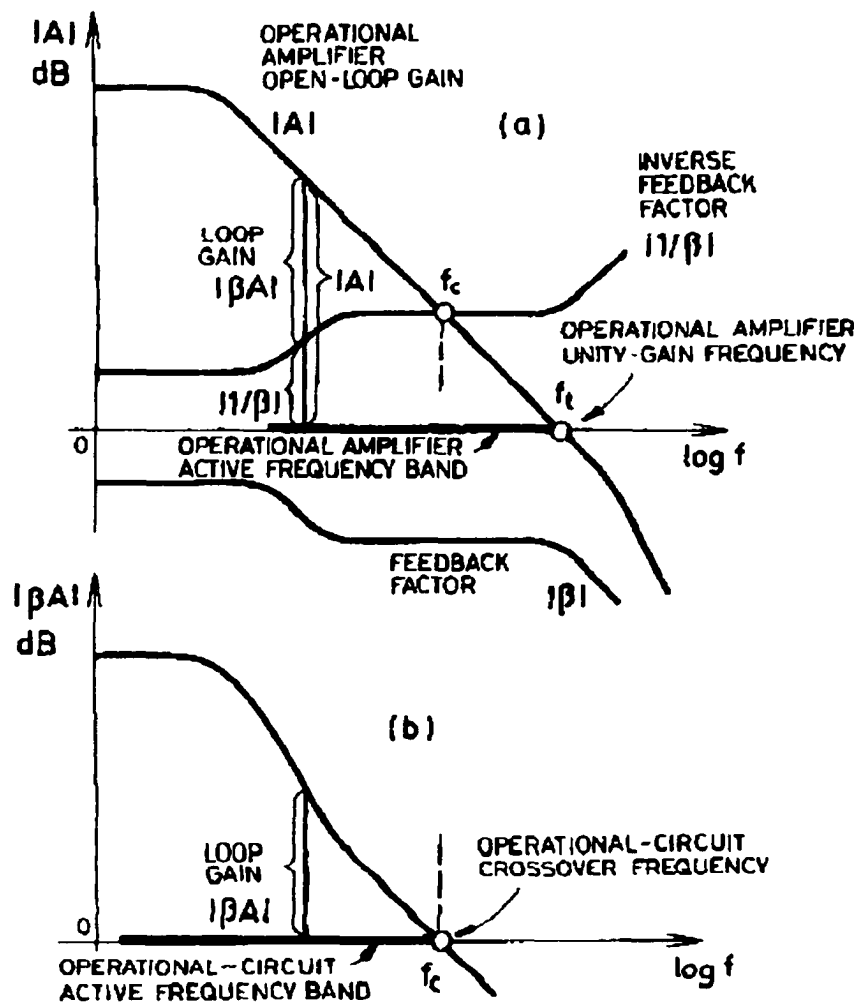


Figure 4.2 Bode plot of gain versus frequency of an operational amplifier and its inverse feedback factor versus frequency plots.

degree phase margin can be found as [10]

$$C_f = C_c / 2 * \sqrt{1 + 4C_I / C_c} \quad (4.2)$$

where C_f is the compensation capacitor across the feedback resistor, R_f , $C_c = 1/2\pi R_f f_c$ and C_I = total input capacitance and f_c = op-amp unity crossover frequency. However, this formula may not apply to a non-unity-gain-stable amplifier.

4.4.3 Noise bandwidth and noise gain

A common practice in low noise circuit design is to minimize the signal bandwidth such that the input noise power can be limited. The bypass capacitor across the feedback resistor and the resistor sets the corner frequency of signal bandwidth. This removes noise presented as an input signal (i.e., input noise at the non-inverting input pin). However, the intrinsic op-amp noise cannot be removed by this single pole filtering, especially in an inverting configuration, such as the transimpedance amplifier. In fact the op-amp noise bandwidth extends across the entire op-amp bandwidth while the signal bandwidth is set by the first order compensation network.

If the signal bandwidth is smaller than the amplifier unity-gain bandwidth, the noise gain will drop to unity at the signal bandwidth unity gain point and continue out to the open-loop 0 dB point. Therefore, while the signal is attenuated, the op-amp noise is still supported by unity gain. For an amplification system with a small signal gain, the op-amp voltage noise can significantly affect a low noise design. As it was pointed out in reference [11], the only way to avoid excessive noise bandwidth is to restrict the frequency range of the op-amp, for instance using passive filtering within the feedback loop.

In many low-noise amplifier designs, a low-pass filter is placed at the output of the

op-amp. Unfortunately, this will increase the output impedance of the circuit. Furthermore, the leakage current of the capacitor may introduce another source of error.

Figure 4.3a shows an improved transimpedance amplifier with passive filtering within the feedback loop to improve the signal-to-noise ratio of the amplifier. This circuit has only one third of the noise [12] of the circuit shown in Figure 4.3b.

4.5 Bias Cancellation Circuitry

In many photodetector applications, a small ac signal of interest is superimposed on a large dc background. When the magnitude of the ac signal is much smaller than its dc background, a large dynamic range is required to provide sufficient gain for the ac portion of the signal. For some applications, the dc output of the photodetector does not provide useful information. It is therefore desirable to provide a dc nulling circuitry to remove the dc background. A current switch has been proposed to perform a similar cancellation function in place of the conventional automatic gain adjustment technique. In this section, we will examine a nulling scheme using a op-amp configured as a transconductance amplifier. In addition to removing the dc portion of the signal, the nulling circuitry can also be configured to remove the relatively high $1/f$ noise content of the output.

The topology for the dc nulling circuit is shown in Figure 4.4. The photodetector current is transformed to an output voltage via a transimpedance amplifier while an error amplifier is used to maintain the low frequency output of the transimpedance amplifier at zero by shunting away the low frequency portion of the input current. This nulling circuit can also be configured to null out 60 Hz or 120 Hz signal with a comb filter preventing the saturation of the transimpedance amplifier. The user can obtain both the low frequency portion of the photodetector current through the feedback network and the rest of the signal

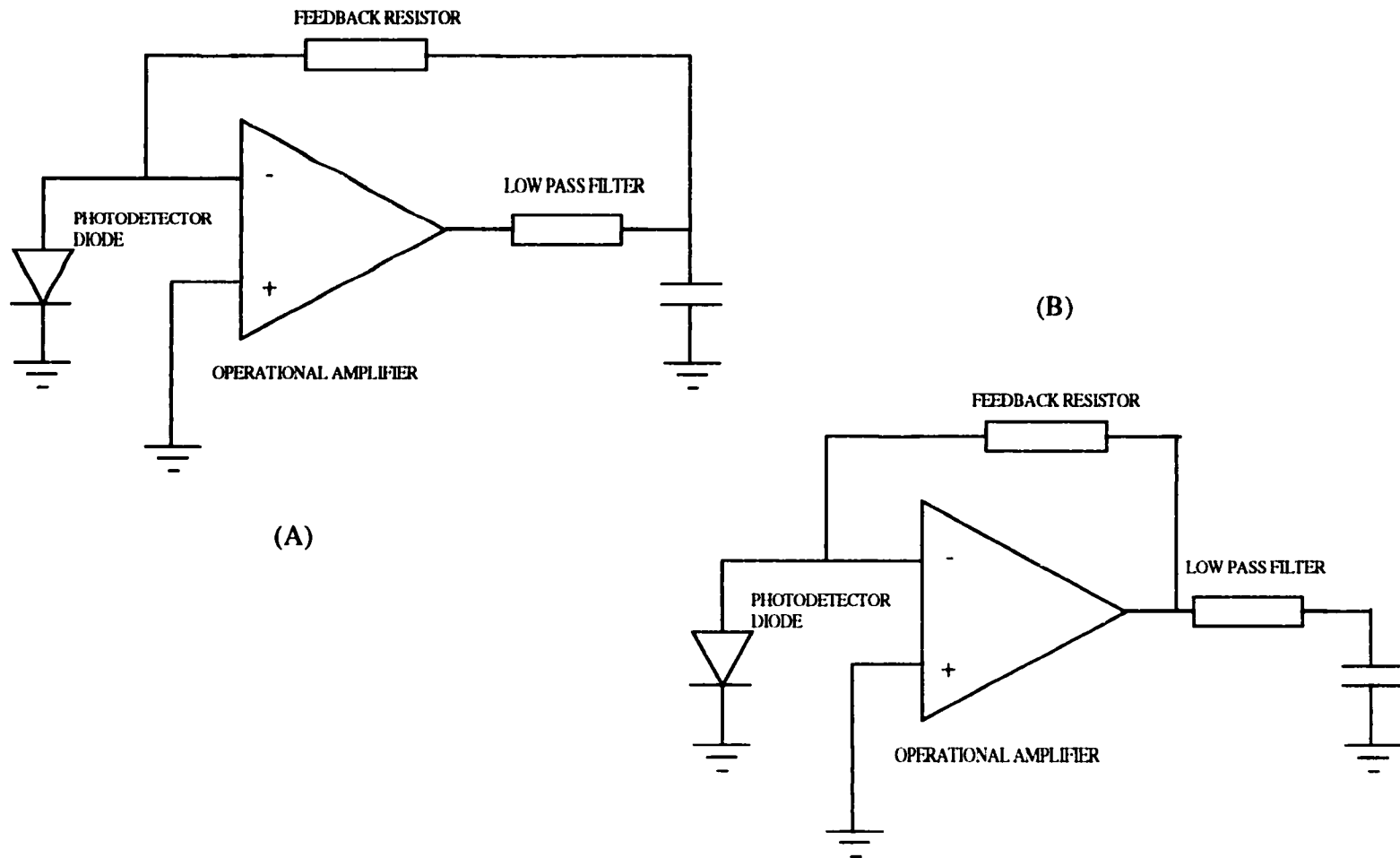


Figure 4.3 (a) Circuit topology for a photodetector pre-amplifier with a low pass filter inside the feedback loop of the system. (b) Alternatively, the low pass filter can be placed outside the feedback loop. However, the former configuration provides a better noise performance.

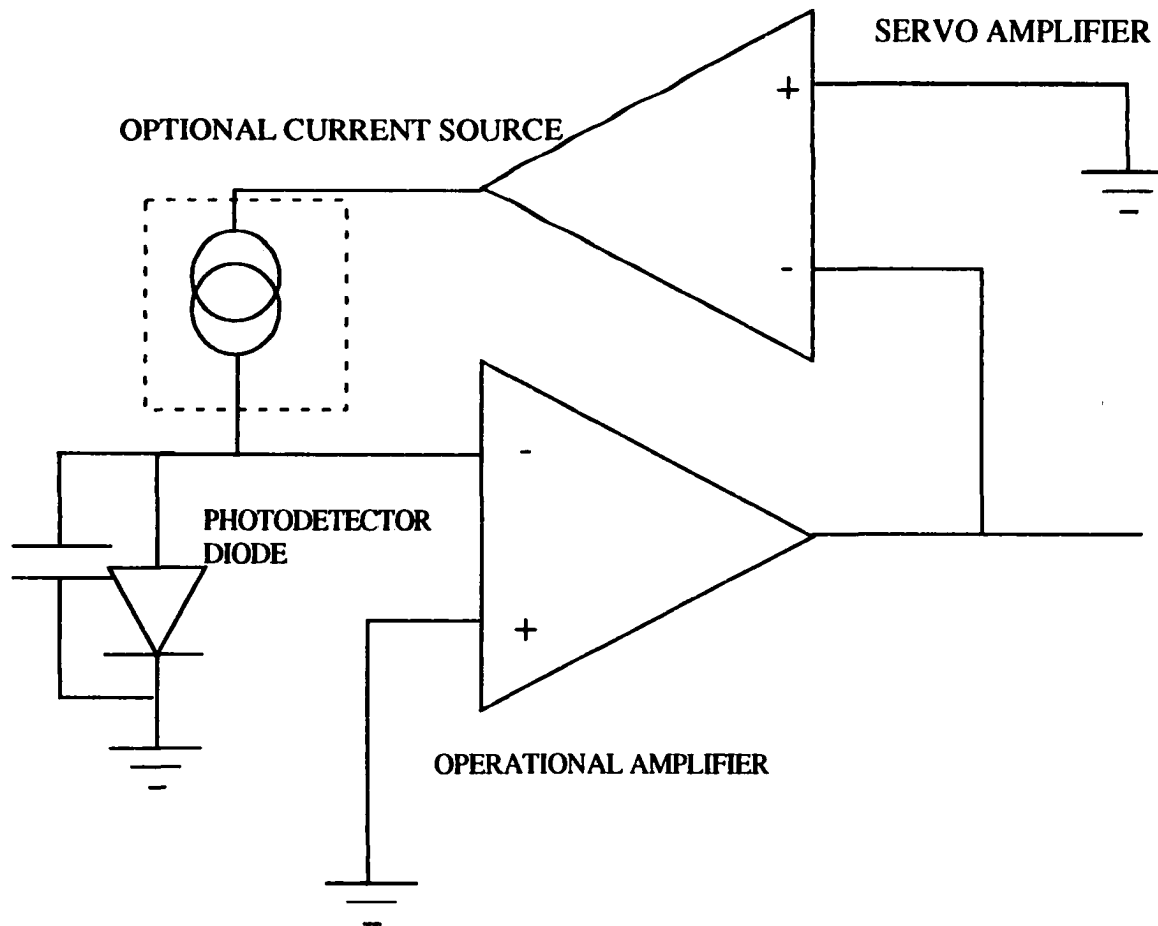


Figure 4.4 A servo amplifier (i.e., an integrator) is used to continuously compensate for the dc background of the optical signal. The diagram indicates the technique schematically. A detailed analysis is required to ensure stable operation of the servo system.

through the output of the transimpedance amplifier. It should be emphasized that the low frequency portion of the signal experiences a different current-to-voltage gain.

4.6 Simulation Results

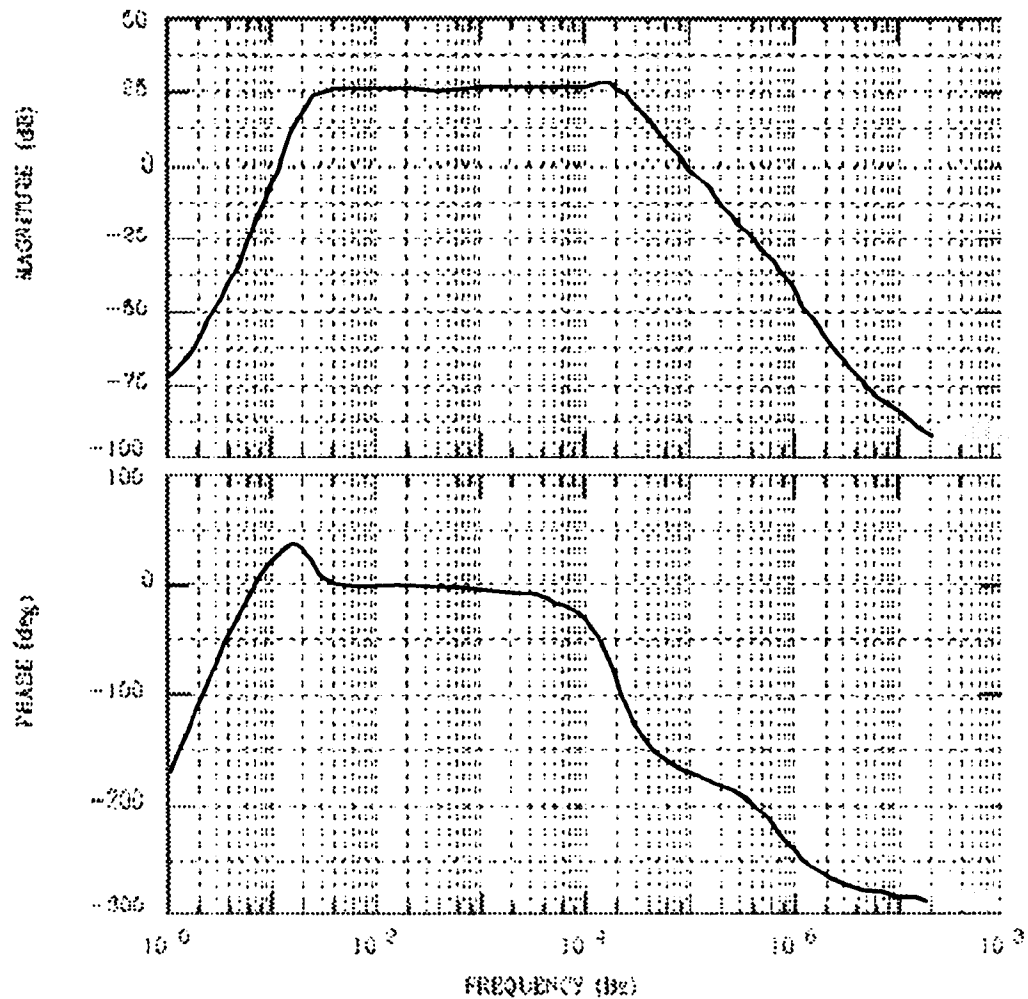
In this section, we examine the simulation results of the photodetector pre-amplifier and the dc nulling circuit. First of all, the performance of a properly compensated photodetector preamplifier is shown. An AD745 low noise operational amplifier with a JFET input is used in the simulation. The photodetector capacitance is assumed to be 2000 pF and a current-to-voltage gain of 10,000 is used. The output of the amplifier with a photogenerated current of 1 micro-ampere is shown in Figure 4.5. The listing for the PSPICE simulation is shown in Appendix C.

In order to extend the dynamic range of the amplifier, the dc background of the photogenerated current can be removed via an integrator. A low noise audio operational amplifier OP27E and a low pass network is used to configure a dc bias nulling circuit, the simulation result is shown in Figure 4.6.

Both of the above simulation results were produced with a properly compensated transimpedance amplifier. Without the compensation effect of the feedback bypass capacitor, a gain peaking phenomenon will be observed. A PSPICE simulation on the gain peak of an improperly compensated transimpedance is shown in Figure 4.7.

PHOTODETECTOR PERAMP

TSPICE+ 2.53A
 G6-A00-95
 14:08:29
 Window 1
 Window 2



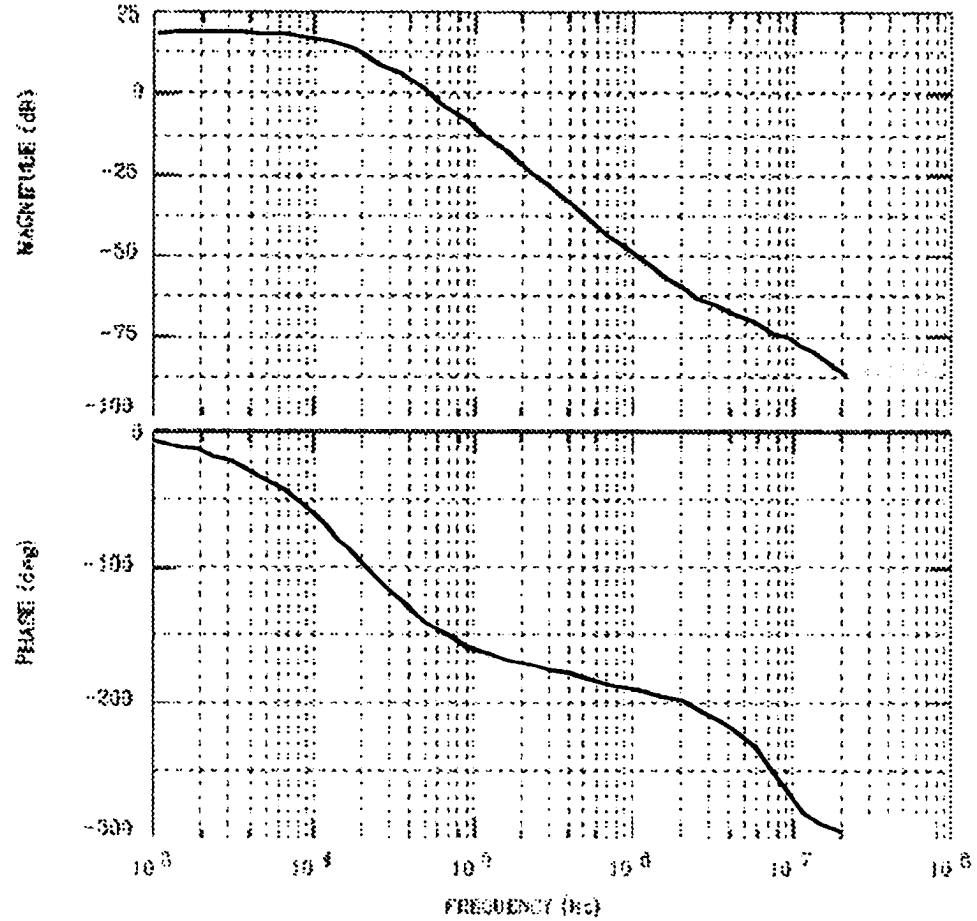
File: DATEPAD08130.DOUT

Figure 4.5 Simulation results of a photodetector preamplifier with a dc bias nulling scheme. the dc bias nullor composes of a low pass network and an open loop operational amplifier serves as the integrator.

PHOTODETECTOR PREAMP

YEPICB: 2.09A
06-AUG-95
13:07:44

Window 1
.....
Window 2
.....



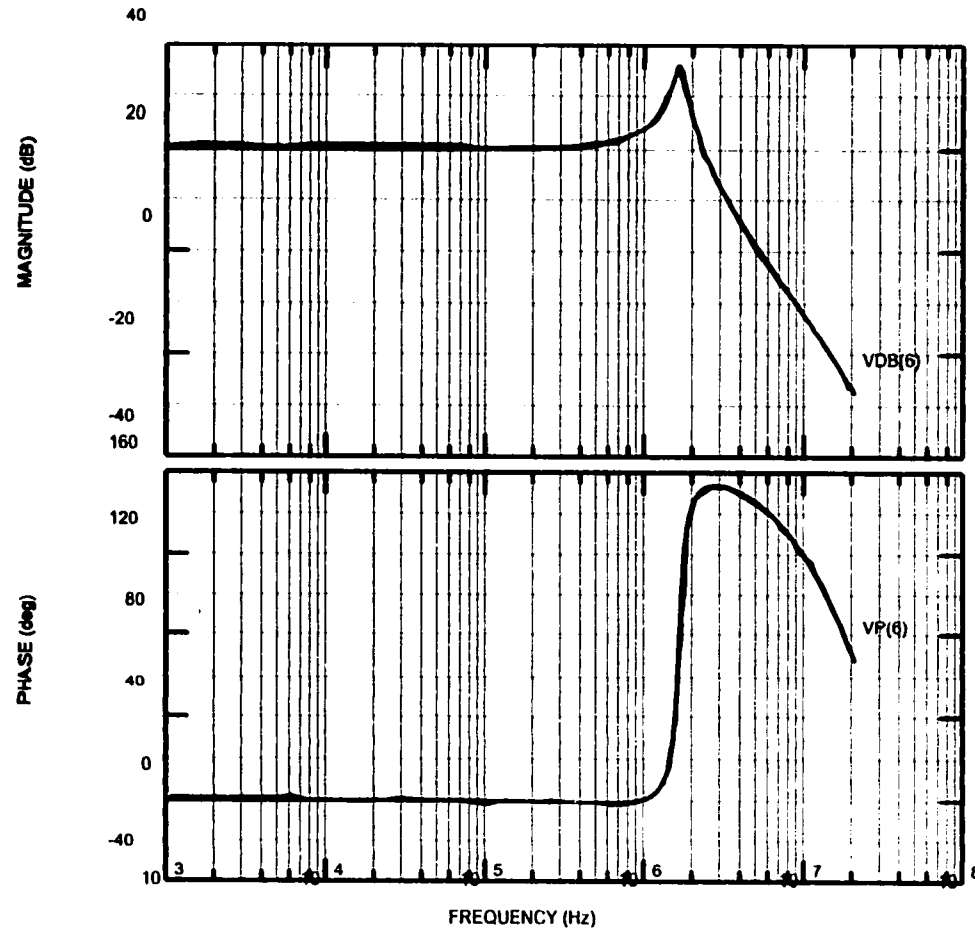
File: DATSP:PGPREAMP.OUT

Figure 4.6 Bode plot of a properly compensated transimpedance amplifier. A low noise JFET input operational amplifier, AD745 is used for the simulation.

TSPICE+ 2.69A
06-AUG-95
14:45:56

Window 1
VDB(6)

Window 2
VP(6)



File: D:\TSP\IPDPREAMP.OUT

Figure 4.7 Simulation results of an improperly compensated transimpedance amplifier. Due to the presence of the second order response of the network, any electrical noise at the input may drive the amplifier into oscillation.

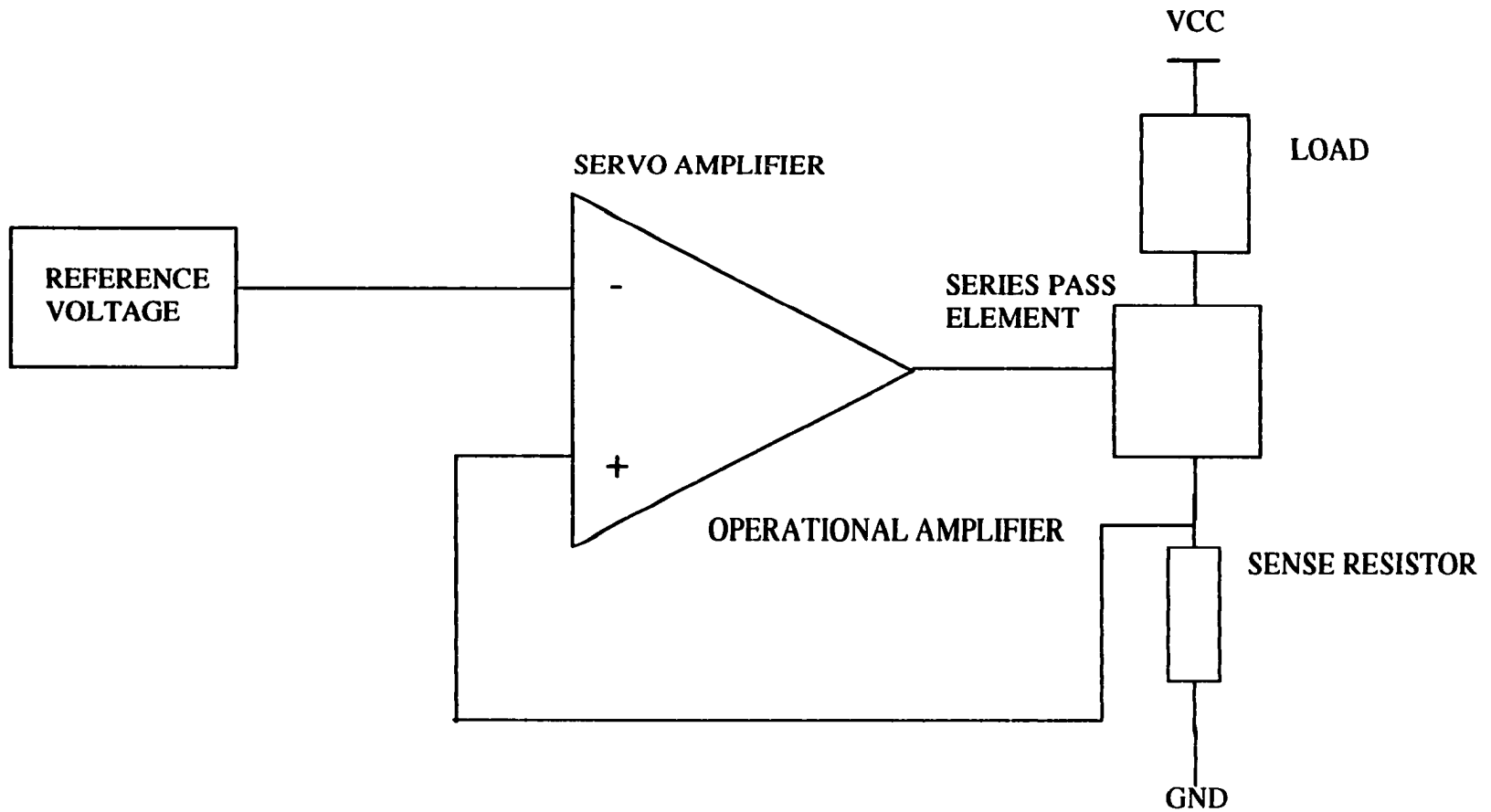
4.7 Diode Laser Current Driver

In addition to the photodetector pre-amplifier, the magnetometer also required a stable and low-noise current supply. Since both the intensity and the wavelength of the diode laser are modulated by the dc supply current, it is important to provide a noise-free dc current to operate the diode laser. Many topologies have been tried previously [13] and their specifications are tailored towards different applications. For example, in an optical communication system, a high speed modulation ability of the diode laser current source is expected. On the other hand, for diode lasers to be used in spectroscopy, a stable emission wavelength is required, and thus a stable dc current supply is desired. In this application, a stable dc current supply was also required. Furthermore, the diode laser current supply should meet the operating temperature requirement of the prototype.

4.8 Regulated Current Source

A current source can be implemented using components as simple as a resistor and a battery. However, its sensitivity to load impedance and the fluctuation of the supply current may be intolerable in most applications. A typical topology of a regulated current source consists of a series pass circuit similar to the one found in a voltage regulator. In general, the series pass current regulator utilizes a dc error amplifier to minimize the difference between a voltage reference and a feedback voltage, which is usually sampled across a sense resistor. This configuration is shown in Figure 4.8. A few key parameters affecting the performance of this kind of current regulator are examined here. One should be aware of the fact that different manufacturers have different pin connections for their diode lasers. An improper design will impair the ability of the built-in photodetector to operate in the photovoltaic mode. The

VCCS



55

Figure 4.8 Schematic diagram of voltage controlled current source. This topology utilizes a reference voltage and a servo amplifier to constantly regulate the voltage drop across the sense resistor.

discussion here applies to Mitsubishi ML-4403 diode and may not apply to other vendors. Nevertheless, the design principle involved will be identical.

4.9 Voltage Compliance, System Stability and Sensitivity

An ideal current source should be able to supply a constant current regardless of the potential drop across the load. The range of potential drop tolerated by the current source is known as the voltage compliance, which is one of the most important specifications of the current source. A poor current regulator such as one formed with a battery and a resistor has very limited voltage compliance since the load voltage directly affects the current flowing through the circuit. Although the current regulator in the prototype drives a load (i.e. a laser diode) with a small fluctuation of load voltage, it is important to understand the allowable operating range of this topology. The voltage compliance of the circuit is related to the operating range of the op-amp and the series pass transistor. When the op-amp reaches its saturating voltage, the current source is not under a feedback control and the proper output current level cannot be achieved. We have studied the voltage compliance of the circuit by inserting a dc voltage source in series with a load resistor and plotted the output current of the regulator versus the load in Figure 4.9. A dc sensitivity analysis was also generated with PSpice and the result indicated that the circuit is extremely sensitive to the value of the sense resistor and the reference voltage level. Although this is a dc analysis result, we can see that a slow drift in the sense resistance or the voltage reference will strongly affect the dc stability of the device.

The current regulator operates as a feedback system by continuously correcting the error between the voltage across the sense resistor and the reference voltage. Since the output of the dc error amplifier is driving the MOSFET gate capacitance, we need to consider

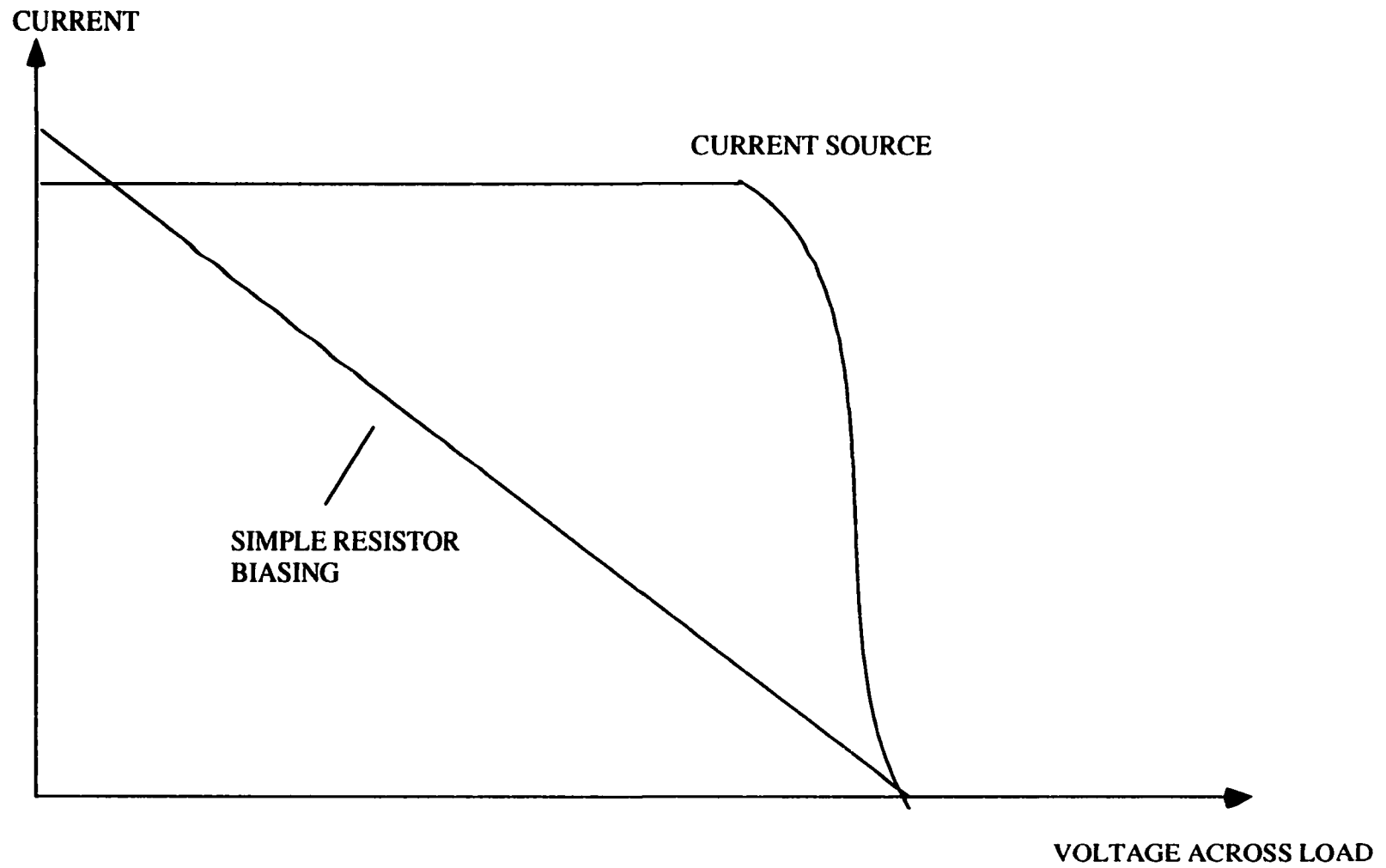


Figure 4.9 A comparison of the voltage compliance capability of a simple resistor biased current source and a voltage controlled current source.

the phase margin of the system. Since the gate capacitance serves a feedback pole, a feedback zero can be used to cancel out its effect as shown in Figure 4.10. A 0.001 μ F capacitance and a pair of resistors, R_1 and R_2 , forms a compensation network to ensure system stability. Since the gate capacitance of the MOSFET varies, the above compensation values are provided as a reference only.

4.10 Noise and Fluctuation Sources

A robust current regulator must maintain a stable output current at all times. The performance of this current regulator with respect to temperature fluctuation, and power supply stability are considered to be the two most probable causes of fluctuation. To avoid drift in output current as the temperature changes, the reference voltage source must be insensitive to operating temperature fluctuations. Currently, the most stable voltage reference, LTZ 1000, is manufactured by Linear Technology. This exhibited a 0.02ppm/K temperature coefficient and a long term stability of 0.01 ppm/year with a properly designed circuit. The op-amp offset voltage, input bias current and open-loop gain also varied with temperature.

Resistor values should be chosen in in the 1k ohm and 10k ohm range to minimize the effect of the temperature coefficient of the copper trace. For example, a 1.25 mm wide, 25 mm long and 35 μ m thick copper trace has a resistance of 10 milli-ohm and a temperature coefficient of 3.4e-3/K. Furthermore, the load resistance of the amplifier should not be too small in order to avoid self-heating of the amplifier. However, a resistance value that is too large will be affected by humidity and should not be used either. Since the gain of an operational amplifier is set by the feedback and input resistance ratio, the stability of the circuit is directly related to the stability of the resistor.

COMPENSATED VCCS

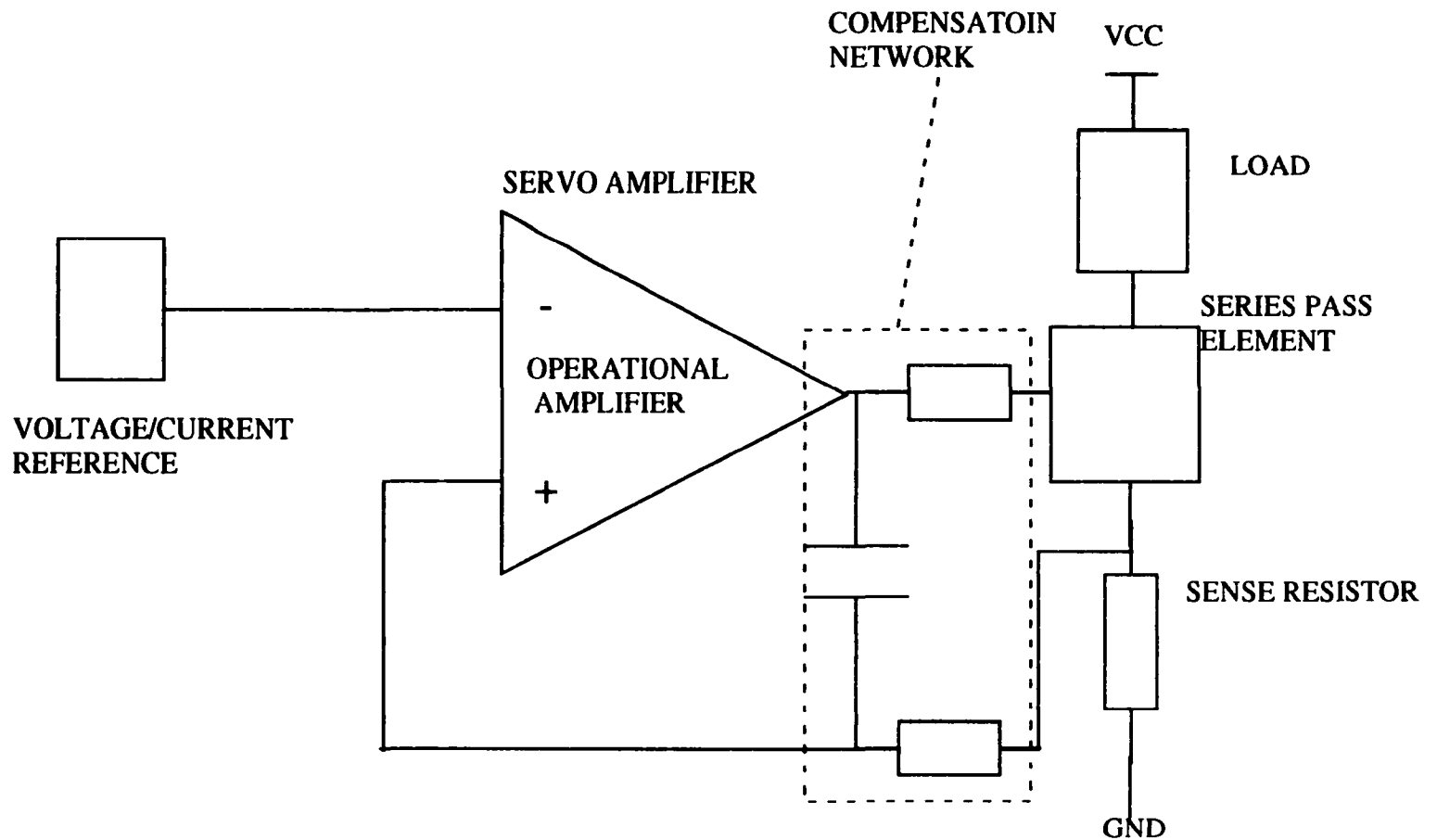


Figure 4.10 Compensation network to cancel the effect of the input capacitance of the series pass element.

Similarly, the stability of the sense resistor affects the performance of the system. Currently a precision, 2 ppm temperature coefficient resistor can be purchased from Vishay, a division of Dale Resistor. Nevertheless, the stray thermal-couple voltage generated by dissimilar metal joints can go as high as 100 nV under unclimatized conditions. Therefore, the sense voltage across the sense resistor should be significantly greater than 100 nV and the offset voltage of the operational amplifier.

Both a voltage reference and a current reference can be used to control the current regulator. The configuration of the current regulator are shown in Figure 4.11. A low drift current regulator using a temperature insensitive voltage reference requires a high quality sense resistor. Currently, we can obtain a 0.1 ppm drift voltage reference and a 0.2 ppm temperature compensated resistor. Therefore, the performance of the current source will be limited principally by the sense resistor. On the other hand, the current regulator using a current source as a reference utilizes the voltage drop across the reference resistor as the reference voltage. This implements a differential scheme such that the sense resistor tracks the reference resistor. It should be noted that a 0 ppm average drift current source (measures from 0 to 50 Celsius) can be obtained from Siliconix. However, the performance of a temperature insensitive voltage reference, such as the one used here, was guaranteed over the industrial temperature range (i.e., -55 deg C to +125 deg C).

The noise performance of a current regulator circuit has been simulated with PSpice. Since PSpice cannot perform an ac sensitivity analysis, we have explicitly put in all the noise generators and performed a dc analysis to identify the most important noise source. For the voltage reference current source, both the voltage reference and the sense resistor fluctuation directly impact the performance of the current source while the current source reference current source removes the dependence on the sense resistor to a certain degree provided the tracking between the sense resistor and the reference resistor are maintained.

COMPENSATED VCCS

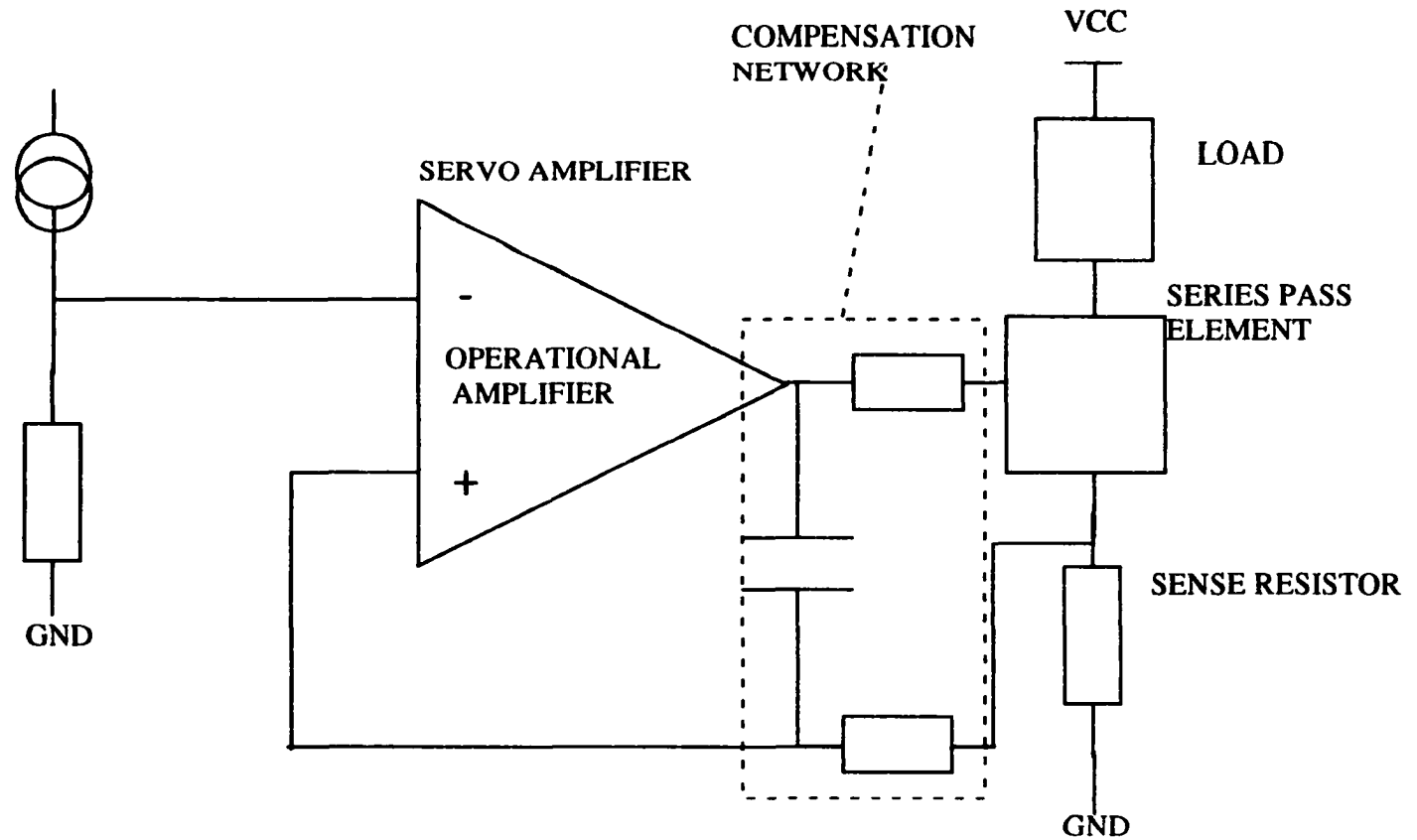


Figure 4.11 A current source reference voltage controlled current source. using a current source as a reference can improve the stability of the system. Furthermore, the cost of a good current reference is lower than the cost of a good voltage reference.

4.11 Transient Protection Circuitry

Since the active layer of the diode laser is extremely thin, it cannot sustain a high current or a voltage spike. To prevent this, transient suppression and reverse bias protection circuits should be used. Usually, a 1N4148 pin diode is reversely connected across the diode laser to avoid an accidental reverse bias on the diode laser. This protection diode must be placed extremely close to the diode laser, with minimal lead inductance. This can be accomplished with a leadless surface mount 1N4148.

In addition to the reverse bias protection, a transient suppressor is needed to protect the diode from power supply turn on and turn off spikes. First of all, the on-off switch must be debounced with a series RC snubber. Furthermore, a “slow-starter” similar to those used in voltage regulator circuits are used. The slow-starter circuit is shown in Figure 4.12. Results of PSpice simulation on the ability of the transient suppressor to suppress both current and voltage spikes are shown in Figure 4.13.

The diode laser should be maintained in the short-circuited position when the power is initially applied to the system. Also, the current level should be kept to a minimum during this transient power-on state. Before the diode laser is turned off, the current level should be reduced to the minimum and the diode laser should be short-circuited. During the investigation of the performance of the device the above procedure was implemented. An all solid-state switching scheme can be employed in the future. In most research grade diode laser drivers (e.g. Spectra Diode Lab SDL-8000), a microcontroller is used to control the timing of the transient protection network. A mechanical relay was used to carry out the switching duties.

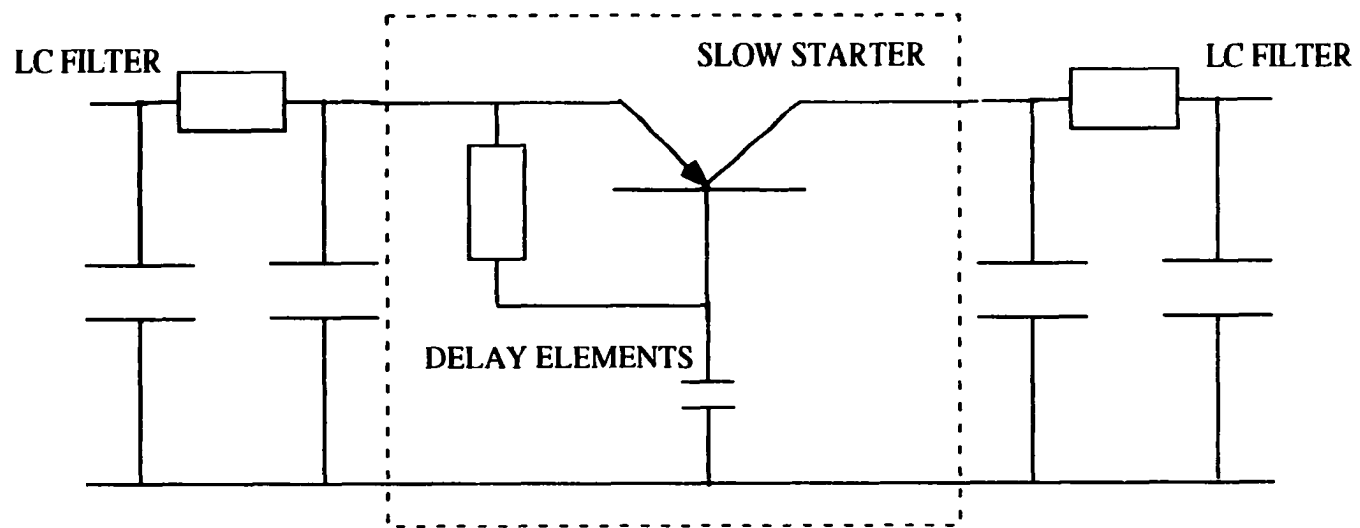


Figure 4.12 Topology of a transient suppressor circuit to protect the diode laser from accidental current and voltage spike.

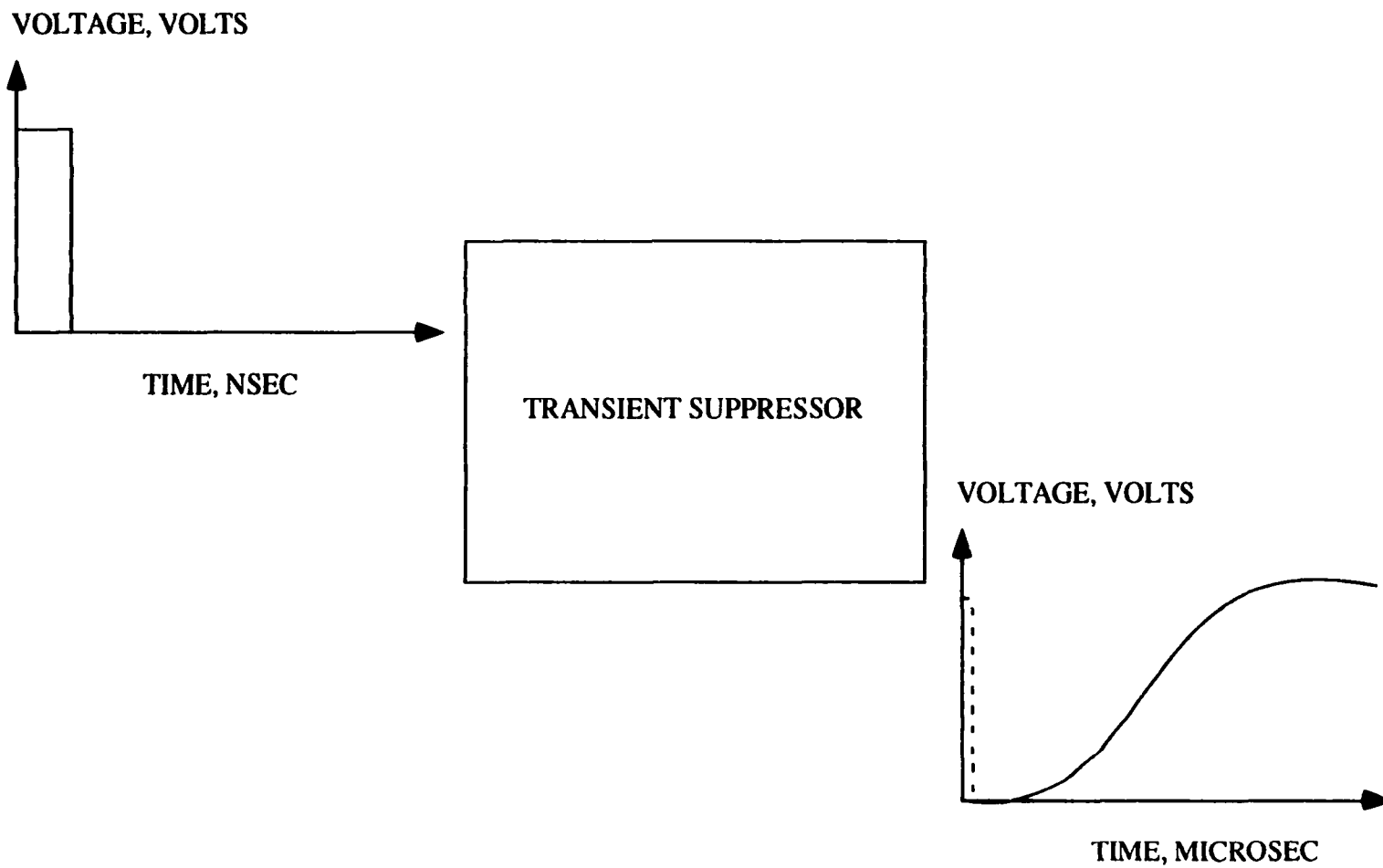


Figure 4.13 Response of the transient suppressor to a current spike. Similar response can be found for a voltage excitation

4.12 Analog-to-Digital Converters and Other Issues

Since the output level of the photodetector can be less than 100 micro-volts, a high resolution analog-to-digital converter must be used. For example, a 5-volt referenced 16-bit converter can only provide a 70 micro-volts bit-resolution. The price and the power consumption level of a converter with higher bit-resolution was too expensive to be used in this application during the development time. This problem can be alleviated by amplifying the signal before the analog to digital conversion. However, the output signal of the sensor is usually composed of a large 120 Hz or 60 Hz signal. The magnitude of other frequency components is very small in comparison.

A broadband amplification will therefore cause the amplifier to saturate and so a frequency selective amplification scheme must be employed. A comb filter, attenuating the 60 Hz component and its harmonics, can be used to prevent the incoming signal from saturating the amplifier. For this application, the user is also interested in the signal at 60 Hz and its harmonics. Assuming the signal is invariant with time, a multiplexing network can be used. A block diagram illustrating the concept is shown in Figure 4.14.

4.13 Servo Techniques for Extended Stability and Dynamic Range

The optimal operating point of the device can be obtained by monitoring the dc or ac output of the device and regulating the coupling distance between the sensor and the transducer via a servo loop. As shown in Figure 4.15, the dc operating point of the device can be chosen and an analog integrator is used to amplify the error signal with respect to a reference voltage and provide the appropriate excitation voltage to the coil maintaining the desired bias point. The performance of such a system is limited by the dc performance of the integrator,

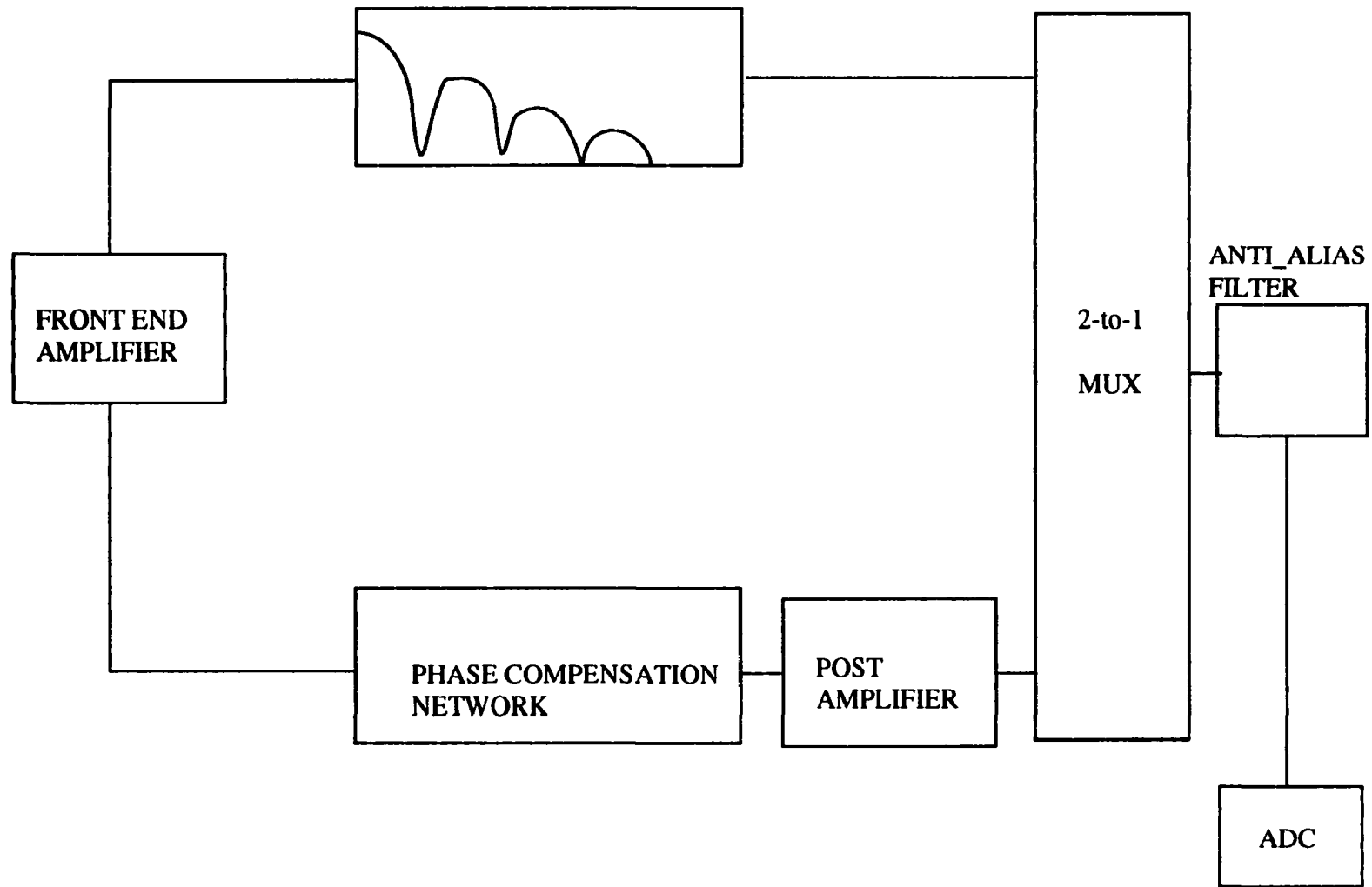


Figure 4.14 Block diagram showing the concept of comb filtering based signal separation technique.

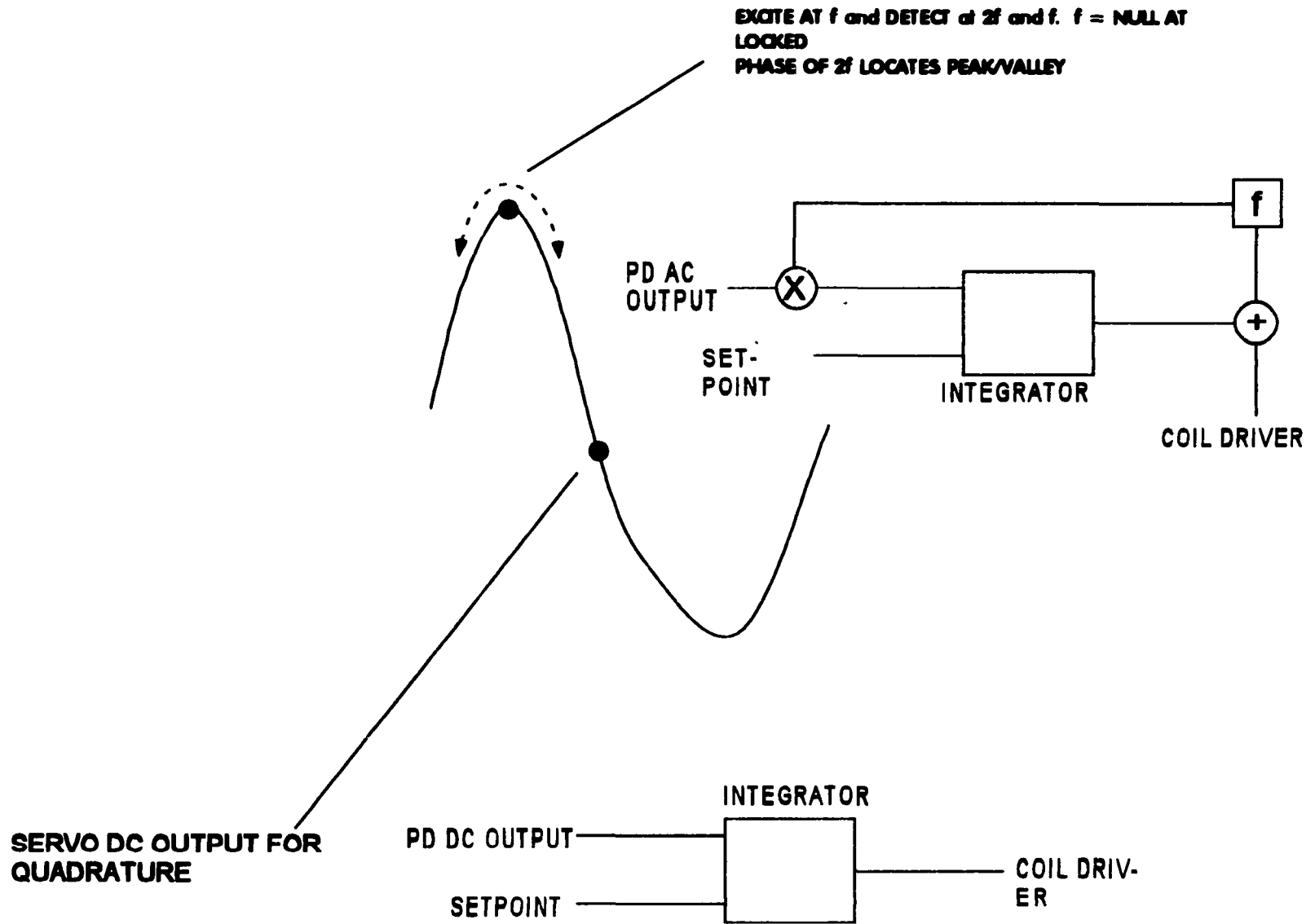


Figure 4.15 Schematic diagram showing the concept of different servo techniques for maintaining system sensitivity and dynamic range.

especially the $1/f$ noise of the integrator amplifier. Alternatively, an ac servo can be used by utilizing the non-linearity of the transfer function: the operating point of the device is maintained at a selected peak of the transfer function, an ac modulating signal at frequency f is applied to the coil. The response of the device will be synchronously detected at the excitation frequency. If the dc operating point of the device deviates from the desired position, a signal at frequency f will be observed. Otherwise, the signal will be up converted to higher harmonics and will not be detected by the synchronous detector. The error signal is also amplified by an integrator and being fed back to the coil. The ac technique provides a narrow band detection scheme, which is not dominated by the $1/f$ noise of the integrator amplifier. Furthermore, if the excitation frequency of the system coincides with one of the resonance frequency of the transducer, a substantial saving in power consumption is expected

In addition to maintaining system sensitivity, a servo system for the provides an extended dynamic range for the measuring device. . A similar technique, known as the flux locked loop is being employed in dc super-conducting quantum interference device (SQUID) instrumentations.

4.14 Power Budget

The total dc power consumption of the magnetometer can be divider into two main areas: digital and analog modules. The digital module comprises of the microcontroller and any other peripheral analog to digital interfacing chips. With the advance of cellular telephone electronics, some very power efficient and small one time programmable (OTP) micro-controllers are available. The analog module consists of the diode laser sensor, the photodetector and other associated driver, detector and signal conditioning electronics. Majority of the dc power is consumed by the diode laser, which can be replaced by a quantum

well semiconductor device for operation in the low milli-watt range. The breakdown of the power consumption for various important items are shown in Figure 4.16.

4.15 Mixed Signal Layout Issues

The signal of interest of the magnetometer usually lies in the microvolt and low millivolt range. It is important to observe a well planned out layout strategy to avoid contamination of the analog signal. A differential signaling scheme is usually desired to obtain low noise analog detection in a mixed signal system. However, a carefully layout printed circuit board can provide a certain degree of isolation. Figure 4.17 depicts a block diagram showing a recommended layout protocol. Starting with the power supply, enough isolation should be provided between different modules, especially the digital and the analog module. Often, a separate power supply may be required for extremely noisy component such as a motor or a pump. Similarly, a single point or star grounding system, which is joined at the chassis, should be used to minimize the crosstalk of return current from various modules via ground resistance. Furthermore, in the sensitive analog section, the signal return path and the power return path should be separated for low noise performance. Appropriate shielding material should also be used to minimize crosstalk via electromagnetic emission. The allowed emission level usually depends on specific standard such as the FCC Part 15.

SYSTEM POWER BUDGET:

DIGITAL MODULE:

MICROCONTROLLER 3-5 mW ONE TIME PROGRAMMABLE

SENSOR AND ANALOG MODULE:

LASER DIODE 100 mW

PHOTODIODE 0.1 mW

DRIVER AND DETECTOR ELECTRONICS 50-70 mW

SYSTEM TOTAL **153.1 - 175.1 mW**

Figure 4.16 System Power Budget.

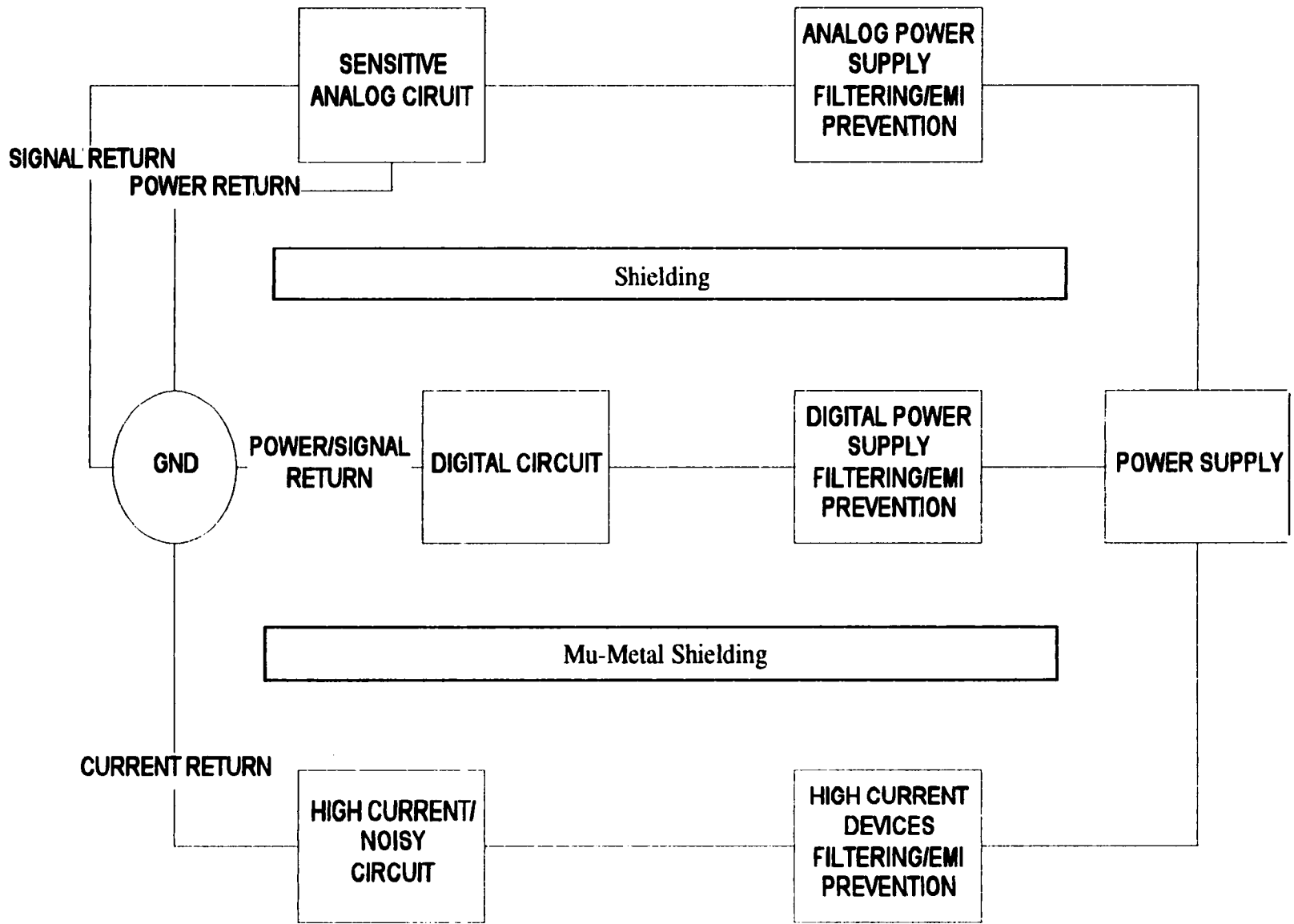


Fig. 4.17 Schematic diagram showing a recommended layout protocol for a mixed signal system.

5. COMPUTER MODELING OF THE DIODE LASER SENSOR COUPLED TO AN EXTERNAL TRANSDUCER

The operating principle of the magnetometer relies on the modulating of the output optical power in a diode laser by a magnetostrictive element, Terfenol-D. A theoretical analysis of the facet reflection coefficient of a diode laser, coupled to an external reflector, can help providing guidance in a better design. The impact of various experimental factors, such as i) coupling distance between the Terfenol and the diode laser, ii) the smoothness of the Terfenol disk surface and iii) the thickness of the active layer, on the performance of the magnetometer are of interest. Section I of this chapter describes the problem in detail and explains the technique used to obtain a solution for the reflection coefficient. Section II introduces the mathematical derivation of the solution and section III discusses computed results and their implications.

5.1 Problem Description

Figure 5.1 depicts the waveguide discontinuity problem of a diode laser sensor coupled to an external perfect reflector. Region 1 is the diode laser cavity, which is represented as a symmetric weakly guiding dielectric waveguide consisting of the cladding layer and the active layer of a typical double heterostructure laser. Although the refractive index of various layers is lossy, they are assumed to be lossless in the following calculation. In addition, we assume a single incident TE mode is being excited in the active layer of the diode laser. The radiation into the free space is represented by a complete set of plane wave spectrum in region 2 while region 3 is considered to be a perfect metal which prohibits field propagation. We are interested in obtaining the modal reflection coefficient, perturbed by the

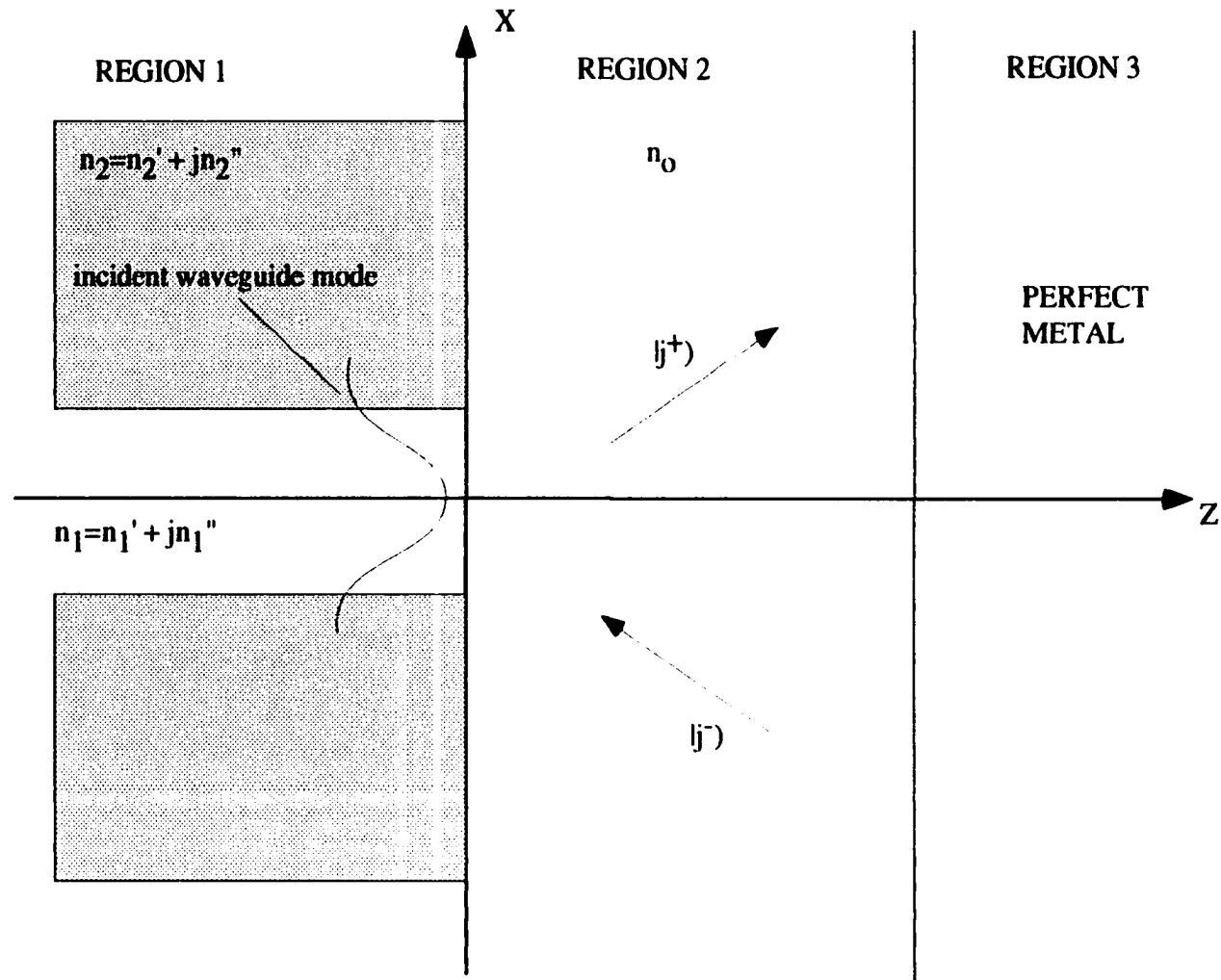


Figure 5.1 Schematic diagram showing the waveguide discontinuity problem of the diode laser sensor. Region 1 composes of the diode laser cavity, region 2 is the coupling gap and region 3 is the transducer material.

coupling distance between the facet and the external reflector , in order to investigate the basic performance of the diode laser sensor. The experimental results demonstrating the basic properties of the diode laser sensor is discussed in Appendix D.

When the active layer of the diode laser is removed, the problem is simplified as a classical mutli-layer reflection problem. The solution of such a reflection problem with an incident plane wave or an incident electromagnetic field represented by a plane wave spectrum can be obtained via the Fresnel reflection coefficient. The exact solution to this problem can be solved via the mode matching technique [14,15,16,17]: the wavefunction in the coupling gap can be expanded in terms of a complete set of free space plane wave functions, while the incident energy from the laser diode facet can be expanded in terms of laser cavity discrete modes and a continous spectrum representing the radiation modes and non-propagating modes. Mathematically, the electromagnetic fields at varous regions can be represented as:

$$E_{region1} = \Psi + r\Psi + \sum_k a_k \phi_k \quad (5.1)$$

where Ψ is the incident TE mode, r is the reflection coefficient for the incident waveguide mode and a_k is the amplitude coefficient for all other waveguide modes generated by the scattering, and ϕ_k is all other allowed waveguide modes. The summation sign represents both a sum of an enumerable set of discrete waveguide modes and the integral of a set of continuous radiation modes. Similarly, the electromagnetic fields at Region 2 can be represented as:

$$E_{region2} = \sum_i (T_i \varphi_i^+ + B_i \varphi_i^-) \quad (5.2)$$

where φ_i^+ is the positive going plane wave, and φ_i^- is the negative going plane wave.

Another sets of equations showing the magnetic fields at both regions can be obtained from (5.1) and (5.2). The unknowns can be solved by requiring the continuity of both the

transverse components of the electric and magnetic fields across the boundary and an integral equation needs to be solved. In general, the infinite radiation mode spectrum prevents an exact solution due to numerical stability. As a result, a common practice is to enclose the system in a perfectly conducting box and discretize the continuous radiation modes. However, the metallic box must be big enough to avoid any interference as a result of the image effect of the metallic boundary [18,19]. Many techniques have been proposed to handle such a problem. These include replacing the entire radiation mode with a plane wave spectrum with a properly chosen propagation constant, which was chosen heuristically [20,21], and replacing both the waveguide mode and the plane wave spectrum with a complete set of basis function such as the Laguerre functions [22], and utilizes the Ritz-Galerkin method to solve for the unknown fields.

As the objective of the present study is to provide a computer model to aid the design and enhancement to the diode laser sensor, a less rigorous approach, due to Kaplan and Deimel [23], is used by assuming the diode laser and the reflector are bounded by a box and expanding the mode function in terms of a complete, discrete set of plane wave spectra assuming the absence of the active layer (i.e., the refractive index of region 1 becomes homogenous). Once all the expansion coefficients are obtained, the Fresnel reflection coefficient is applied accordingly. In order to improve the precision of the model, the presence of the active layer can be taken into account following [23] with an infinite perturbation expansion in terms of a suitably chosen integral of the actual difference in refractive index.

For an optically smooth surface, the Fresnel reflection coefficient can be applied to model the plane wave reflection at the air-external reflector interface. However, for an optically rough surface, the Fresnel reflection coefficient is improper. To take full advantage of the previous calculation method, a simple approach is being proposed to extend the plane

wave expansion technique to account for a rough surface. The roughness of the external reflector is assumed to be less than a quarter of the laser light wavelength (i.e. $0.78 \mu\text{m}$) as a result of the $0.2 \mu\text{m}$ lapping process. In addition, we assume information regarding the correlation length and the statistical distribution function of the rms surface roughness can be obtained.

Instead of assuming a perfect reflection at the boundary of Region 2 and Region 3, the magnitude and phase of each incident plane wave spectrum is obtained at the rough surface-air interface. The planar wavefront of an incident plane wave is perturbed by the rough surface via a random phase screen approach. The distorted wavefront is then expanded by a complete set of plane wave spectra. The Fresnel reflection coefficient for the smooth surface between region 2 and 3 is replaced by the effective Fresnel reflection coefficient, which can be applied to the previous model. It should be noted that the entire set of incident plane wave spectra must be accounted for in order to provide a proper reflection coefficient for the rough surface.

5.2 Mathematical Derivation on Calculating the Reflection Coefficient

The wave functions in the active areas of the diode laser cavity can be represented as:

$$\Psi(x, z) = e^{i\beta z} g(x) \quad (5.3)$$

$$\phi(x, z) = e^{-i\beta z} m(x) \quad (5.4)$$

where ψ is the fundamental waveguide mode travel toward the diode laser facet (i.e., traveling in the positive z direction) and ϕ is the other waveguide modes scatter away from the facet respectively (i.e., traveling in the negative z direction). $g(x)$ and $m(x)$ are the

amplitude distribution functions for the fundamental mode and higher order waveguide mode respectively. At $z=0$, the field distribution takes the form [24]:

$$E_{Cladding\ Layer}(x) = A \cos\left(\frac{dh_a}{2}\right) e^{h_c\left(\frac{d}{2}-x\right)} \quad (5.5)$$

in the cladding region, and

$$E_{Active\ Layer}(x) = A \cos(h_a x) \quad (5.6)$$

in the active region, where A is the amplitude factor and

$$h_c = \sqrt{\beta^2 - n_{cladding}^2 k_o^2} \quad (5.7)$$

$$h_a = \sqrt{n_{Active}^2 k_o^2 - \beta^2} \quad (5.8)$$

with $n_{cladding}$ and n_{Active} as the refractive index in the cladding and active area of the diode laser respectively and k_o as the free space propagation constant in free space. Valid h_a and h_c must satisfy the following transcendental equation:

$$h_c \cos\left(\frac{dh_a}{2}\right) = h_a \sin\left(\frac{dh_a}{2}\right) \quad (5.9)$$

The j^{th} component of the plane wave spectra of region 2, which lies between region 3, (the Terfenol disk) and region 1 (the diode laser facet) can be represented as:

$$j^+(x, z) = B_j e^{ip_j x} e^{iq_j z} \quad (5.10a)$$

for the positive z going plane wave, and

$$j^-(x, z) = B_j e^{ip_j x} e^{-iq_j z} \quad (5.10b)$$

for the negative z going plane wave, with

$$p_j^2 + q_j^2 = k_o^2 n_2^2 \quad (5.10c)$$

where n_2 is the refractive index of region 2, p_j and q_j are the x and z component of the wave vector for the j^{th} component of the plane wave spectra in region 2. The transducer material

was assumed to be a perfect metal for simplicity. Thus all fields vanished at the transducer surface at $z = t$. Nevertheless, the analysis technique can be extended to analyze a conventional metallic interface between region 2 and 3 by introducing another set of plane wave spectra in region 3 and matching the boundary conditions at the interface.

With the above definitions, the fields at various regions can be represented as:

Within the diode laser cavity:

$$E_{region1}(x, z) = \Psi(x, z) + r\Psi(x, z) + \sum_k a_k \phi_k(x, z) \quad (5.12)$$

where r is the reflection coefficient for the incident waveguide mode, Ψ , and a_k is the amplitude coefficient for all other waveguide modes generated by the scattering, and ϕ_k is all other allowed waveguide modes. The summation sign is used to highlight the fact that all waveguide modes should be included for completeness.

Within the free space coupling gap (i.e., region 2):

$$E_{region2}(x, z) = \sum_j [b_j j^+(x, z) + d_j j^-(x, z)] \quad (5.13)$$

where b_j and d_j are the amplitude coefficients for the standing waves in the coupling gap.

The summation sign indicates that a proper representation of the standing wave inside the coupling gap requires the entire plane wave spectrum. Within a perfect metal, no field exists.

The solution to the scattering problem is obtained by demanding the continuity of the tangential electric and magnetic fields at the appropriate interfaces. Although only electric field wave functions are described here, the magnetic fields can be obtained via the Maxwell equations:

$$\text{Curl } \mathbf{E} = -\dot{\mathbf{B}} \quad (5.14)$$

which can also be stated as:

$$\mathbf{k} \times \mathbf{E} = -\dot{\mathbf{B}} \quad (5.15)$$

where \mathbf{E} is the electric field vector and \mathbf{k} is the wave vector and \mathbf{B} is the magnetic flux. For

example, it can be shown that the tangential magnetic field at region 2 is:

$$B_{\text{tangential}} = \left(\frac{n_2}{c}\right) \cos \theta_2 j^+(x, z = 0) \quad (5.16)$$

where $B_{\text{tangential}}$ is the tangential magnetic field component and n_2 is the refractive index of region 2 and θ_2 is the incident (or transmitted) angle of $j^+(x, z)$ with respect to the surface normal of the diode laser facet, region 1.

Using Snell's law, the relationship between incident angles and refracted angles can be found provided the refractive index of two regions forming the interface are known.

Using the following definition for the h operator,

$$h_1(\theta_2) = \sqrt{1 - \left(\frac{n_2}{n_1}\right)^2 \sin^2 \theta_2} \quad (5.17)$$

$$h_2(\theta_2) = \sqrt{1 - \sin^2 \theta_2} \quad (5.18)$$

$$h_1(\theta_2) = \sqrt{1 - \left(\frac{n_2}{n_1}\right)^2 \sin^2 \theta_2} \quad (5.19)$$

Thus, $B_{\text{tangential}}$ for region i , as a function of x co-ordinate, can be found proportional to:

$$B_{\text{tangential}}(x) \propto n_i(x) h_i(\theta_2, x) j^+(x, z = 0) \quad (5.20)$$

for the forward travelling waves. A similar equation can be derived for the negative travelling waves by replacing j^+ with j^- . Note that as the refractive index is non-homogenous across the x co-ordinate, the appropriate h operator should be used and it is emphasized by rewriting them as $h_i(\theta_2, x)$ in (5.20),

Using the above notation and equation (5.13), the continuity requirement for both the magnetic and electric fields at the coupling gap can be written:

Tangential electric fields:

$$\sum_j [b_j j^+(x, z = 0) + d_j j^-(x, z = 0)] = 0 \quad (5.21)$$

assuming a perfect metal in region 3, and

Tangential Magnetic fields:

$$\sum_j [b_j n_2 h_2 j^+(x, z=0) + d_j n_2 h_2 j^-(x, z=0)] = 0 \quad (5.22)$$

assuming a perfect metal in region 3.

Although the inclusion of equation (5.22) is redundant in this case, it is provided here for completeness. As region 2 is uniform in x-co-ordinate, the x dependence of the refractive index n_2 and h_2 is omitted. A correspondence between h_2 and the wave vector $j^+(x,z)$ or $j^-(x,z)$ is indicated by θ_2 in (5.22), which requires a different h_2 for each wave vector, j . If the assumption for region 3 is removed, a suitably chosen set of orthogonal and complete wave functions, such as the plane wave basis function, should be used on the right hand side of equations (5.21) and (5.22). The above sets of equations can be solved by invoking the orthogonality relationship. the which can be written as:

$$\int_{-\infty}^{\infty} (j^+(x, z))^* l^-(x, z) dx = \delta_{jl} e^{-iq_j z} e^{-iq_l z} \quad (5.23)$$

where δ_{jl} is the Kronecker delta function, and j^+ and l^- are two arbitrary components of the plane wave spectra in region 2. Note that the integration is in the x co-ordinate only and is z dependent. Invoking the orthogonality conditions, the following relationships between the amplitude functions of the fields at the surface between the coupling gap and the transducer are found:

$$b_j + d_j e^{-2i(2m_2 h_2 t / \lambda_0)} = 0 \quad (5.24)$$

$$n_2 h_2 (b_j - d_j e^{-2i(2m_2 h_2 t / \lambda_0)}) = 0 \quad (5.25)$$

where λ_0 is the free space wavelength and t is the coupling distance.

At the interface between the diode laser facet and the coupling gap, the continuity of the electric field components at the surface gives:

$$\begin{aligned} \Psi(x, z=0) + r\Psi(x, z=0) + \sum_k a_k \phi_k(x, z=0) \\ = \sum_j [b_j j^+(x, z=0) + d_j j^-(x, z=0)] \end{aligned} \quad (5.26)$$

can be rewritten as:

$$\begin{aligned} \sum_l f_l l^+(x, z=0) + r \sum_l f_l l^+(x, z=0) + \sum_l \sum_k a_k \left(\int_{-\infty}^{\infty} l^+(x, z=0) \phi_k dx \right) l^+(x, z=0) \\ = \sum_j [b_j j^+(x, z=0) + d_j j^-(x, z=0)] \end{aligned} \quad (5.27)$$

with the inner product between l^+ and ψ as f_l at $z=0$. Equation (5.27) is effectively the spectral representation of (5.26). With the waveguide modes represented as a enumerable set of plane wave spectra, the h operator defined previously can be applied to find the tangential magnetic fields:

$$\begin{aligned} n_1(x)h_1(x) \left[\sum_l f_l l^+(x, z=0) + r \sum_l f_l l^+(x, z=0) \right] + \sum_l \sum_k a_k \left(\int_{-\infty}^{\infty} l^+(x, z=0) \phi_k dx \right) n_1(x)h_1(x) l^+(x, z=0) \\ = n_2 h_2 \sum_j [b_j j^+(x, z=0) + d_j j^-(x, z=0)] \end{aligned} \quad (5.28)$$

Projecting (5.27) and (5.28) with $j(x, z=0)$, (a process which is equivalent to multiplying (5.27) and (5.28) with $j(x, z=0)$ and integrating with respect to the x co-ordinate. Intuitively, it is similar to equating the spectral components on both sides of the equation.) and invoking the orthonormal condition, the following are obtained:

$$f_j + f_j r + \sum_k a_k \int_{-\infty}^{\infty} j^-(x, z=0) \phi_k dx = b_j + d_j \quad (5.29)$$

$$\begin{aligned} \sum_l [f_l + f_l r + \sum_k a_k \int_{-\infty}^{\infty} l^+(x, z=0) \phi_k dx] \int_{-\infty}^{\infty} j^-(x, z=0) n_1(x)h_1(x) l^+(x, z=0) dx \\ = n_2 h_2 (b_j - d_j) \end{aligned} \quad (5.30)$$

Since $n_1(x)$ and $h_1(x)$ are spatially dependent, they cannot be separated out for integration. A zero order approximation, which assumes the refractive index of the diode laser structure can be represented by the average of the refractive index of the cladding and the active area, is invoked here to continue on the calculation. A series expansion can be used to obtain a more

accurate result [23]. For the purpose of studying the dependence of coupling gap and sensor response, the above approximation seems to work well. Therefore,

$$n_1(x)h_1(x) = n_1h_1 + \text{first order and second order terms} \quad (5.31)$$

By performing the inner product of (5.26) with Ψ and invoking orthogonality relationship between different waveguide modes, we obtain:

$$1 + r = \sum_j f_j^* (b_j + d_j) \quad (5.32)$$

or

$$r = \sum_j f_j^* (b_j + d_j - f_j) \quad (5.33)$$

by utilizing the relationship $1 = \sum_j f_j f_j^* |_{z=0}$ (assuming a properly normalized waveguide mode) and f_j^* as the complex conjugate of the j^{th} spectral component of Ψ . A relationship between b_j and f_j can be obtained via (5.29) and (5.30) using only the zero-th order approximation. As the product between n_1h_1 is now a constant, it can be extracted out of the integration.

Invoking the orthogonality property, the series summation is reduced to one term in (5.30).

By combining (5.29) and (5.30), (5.24) and (5.25) and substituting, we obtain:

$$\begin{aligned} & f_j(n_1h_1 - n_2h_2)/(n_1h_1 + n_2h_2) + f_j \\ & = b_j \{ 1 + [(n_1h_1 - n_2h_2)/(n_1h_1 + n_2h_2)] [(n_2h_2 - n_3h_3)/(n_2h_2 + n_3h_3)] \exp(2\pi n_2h_2t/\lambda_0) \} \end{aligned} \quad (5.34)$$

Replacing the plane boundary Fresnel reflection coefficients, $(n_1h_1 - n_2h_2)/(n_1h_1 + n_2h_2)$ and $(n_2h_2 - n_3h_3)/(n_2h_2 + n_3h_3)$ with r_{12} and r_{23} respectively, the modal reflection coefficient can be written as:

$$r = \sum_j R f_j (f_j^*) \quad (5.35)$$

$$R = [r_{12} + r_{23} \exp(2\pi n_2h_2t/\lambda_0)] / [1 + r_{12} r_{23} \exp(2\pi n_2h_2t/\lambda_0)] \quad (5.36)$$

It should be emphasized that all of the Fresnel coefficients are function of the angle of

incident. Equation (5.35) suggests the interpretation that the modal reflection coefficient is the overlapping integral, in the continuum case, between the incident waveguide mode and the reflected waveguide mode in the spectral domain.

5.2.1 Modeling of a rough external reflector

With a perfect reflector, there is a one to one correspondence between the incident plane wave vector and the reflected plane wave reflector. It is governed by Snell's law that the incident angle is identical with the reflected angle. With respect to $z=0$, an additional phase shift is required to properly described the relationship between the incident and reflected wave vector. A random phase screen approach, which assumes only the phase of the incident plane wave vector be perturbed by the rough surface, is proposed to model the effect of the rough reflector. The general algorithm is to reflect a set of plane wave spectra through the phase screen and re-calculate the phase and amplitude of each of the spectra. The original Fresnel reflection coefficient, r_{23} , is now replaced by the amplitude and phase of the perturbed plane wave spectrum. It should be emphasized that in order to check the validity of the above proposal, a benchmark analytical solution needed to be formulated.

5.3 Computation Results

The first step in calculating the modal reflection coefficient requires the knowledge of the fundamental TE mode of the symmetric dielectric waveguide. The mode profile can be obtained by solving the dispersion equation (5.9), which was obtained numerically through the Matlab computation environment. The mode function of the even TE mode is shown in Figure 5.2 and the spectral domain representation of the modal function is shown in Figure

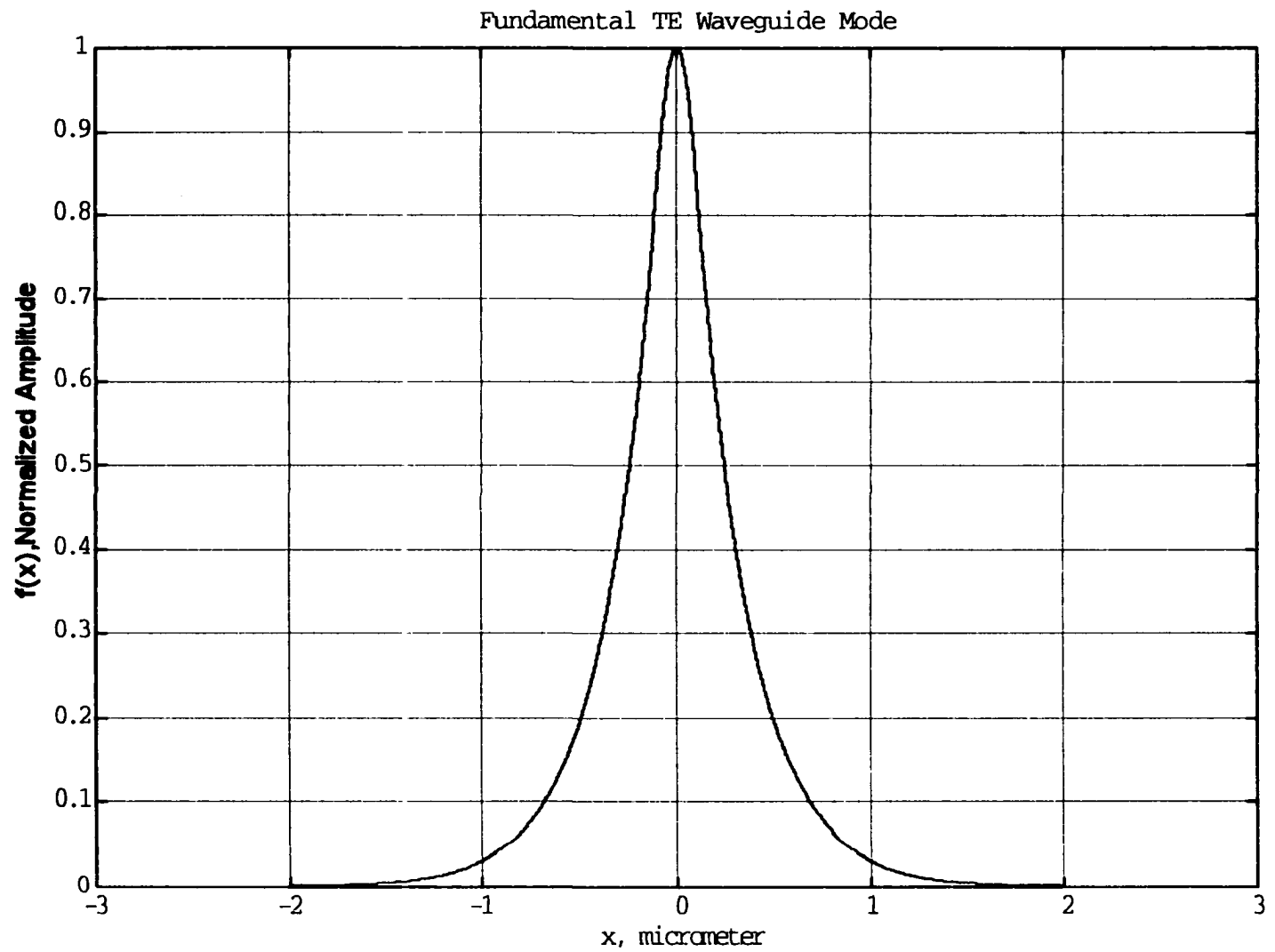


Figure 5.2 The modal distribution of the fundamental, even TE mode of a symmetrical weakly guiding waveguide.

5.3. The spectral representation is obtained via the Fourier transform. The material parameters are listed in the Matlab source code as shown in Appendix E.

The transfer characteristics of the diode laser is obtained by computing (5.35) and (5.36) by varying the coupling distance, t , in (5.36). The characteristics of the modal reflectivity of the diode laser sensor is shown in Figure 5.4. It compares reasonably well with the experimental data described in Appendix D. As the actual coupling distance cannot be determined easily, only qualitative comparison can be made. With a metallic external reflector, it is not possible to obtain an estimate of the coupling distance. However, using a dielectric reflector such as a microscope slide, an experiment can be constructed to verify the quantitative relationship between the coupling distance and the computational results, provided an inverse relationship exists between the far field pattern of the radiation and the modal characteristics of the emission at the facet.

The proposed experimental setup is shown in Figure 5.5. A microscope slide is used as an external reflector and the far field radiation pattern is transformed by a high quality fourier transform lens. The image is analyzed by a beam analyzer, which profiles the beam via a CCD array. It should be noted that only the intensity of the beam will be measured by the analyzer. The mathematical relationship between the far field pattern and the coupling distance need to be derived to make use of the data.

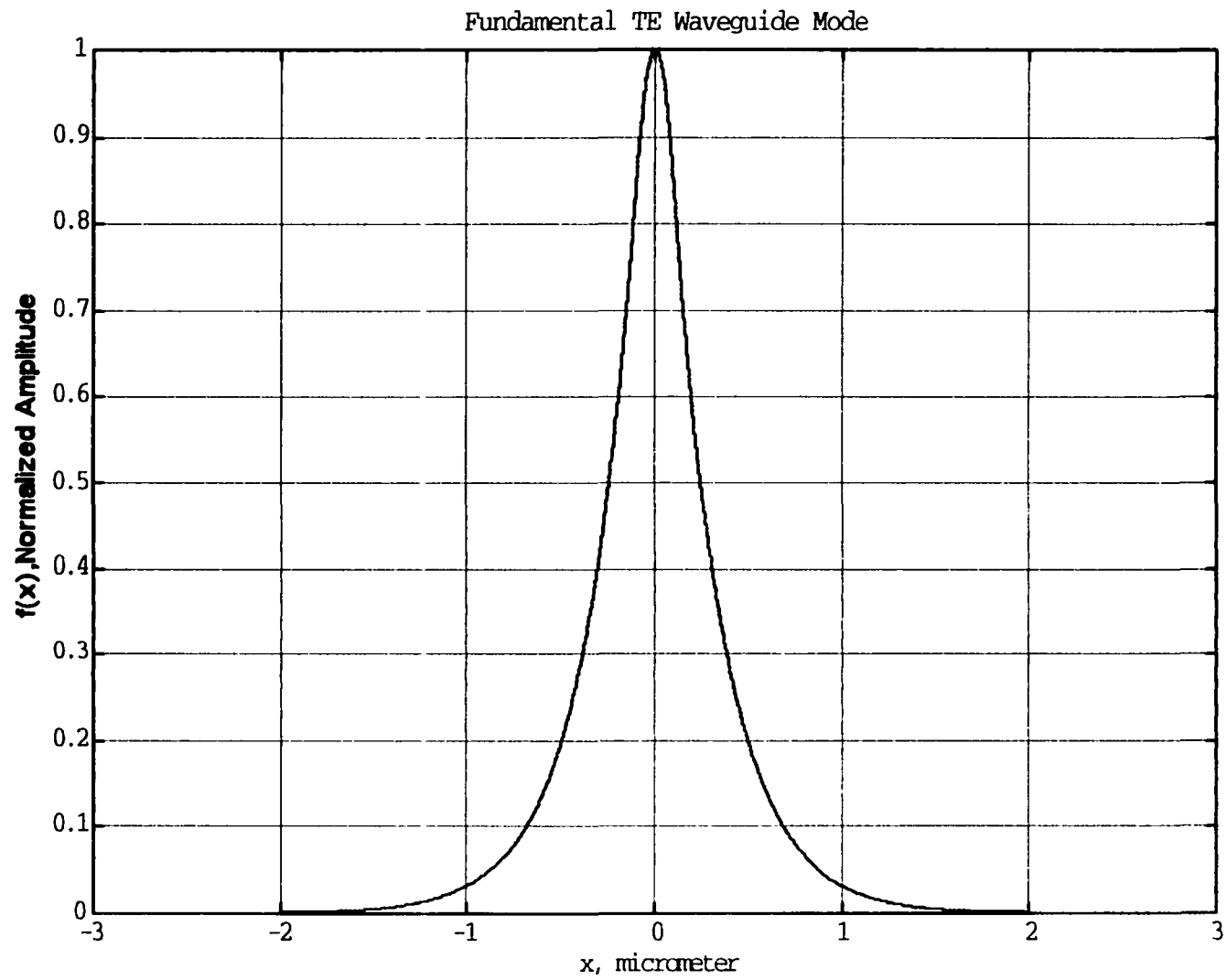


Figure 5.3 The spectral domain distribution of the fundamental, even TE mode of a symmetrical weakly guiding waveguide.

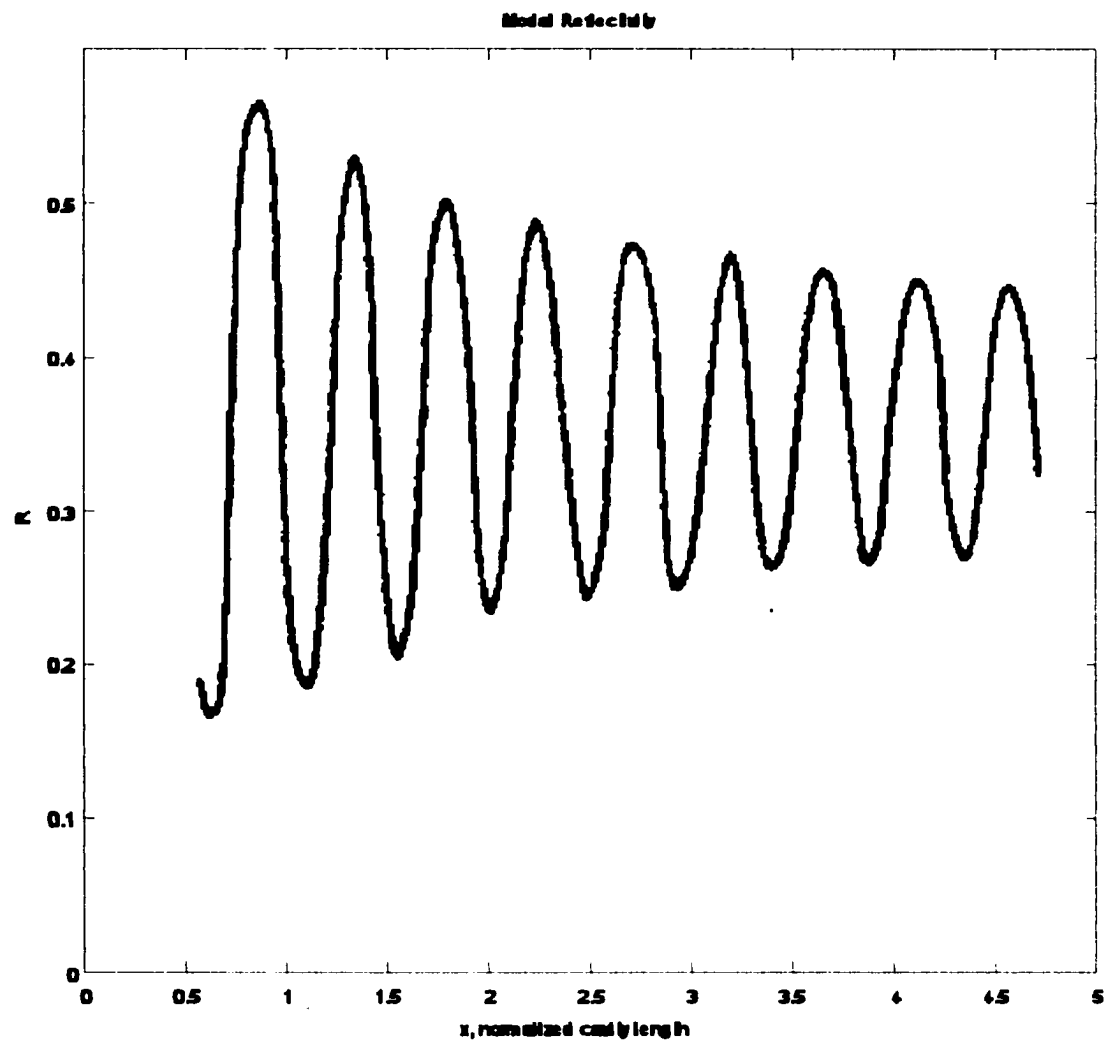


Figure 5.4 The modal reflectivity of a diode laser sensor coupled to a perfect external reflector with a varying coupling distance.

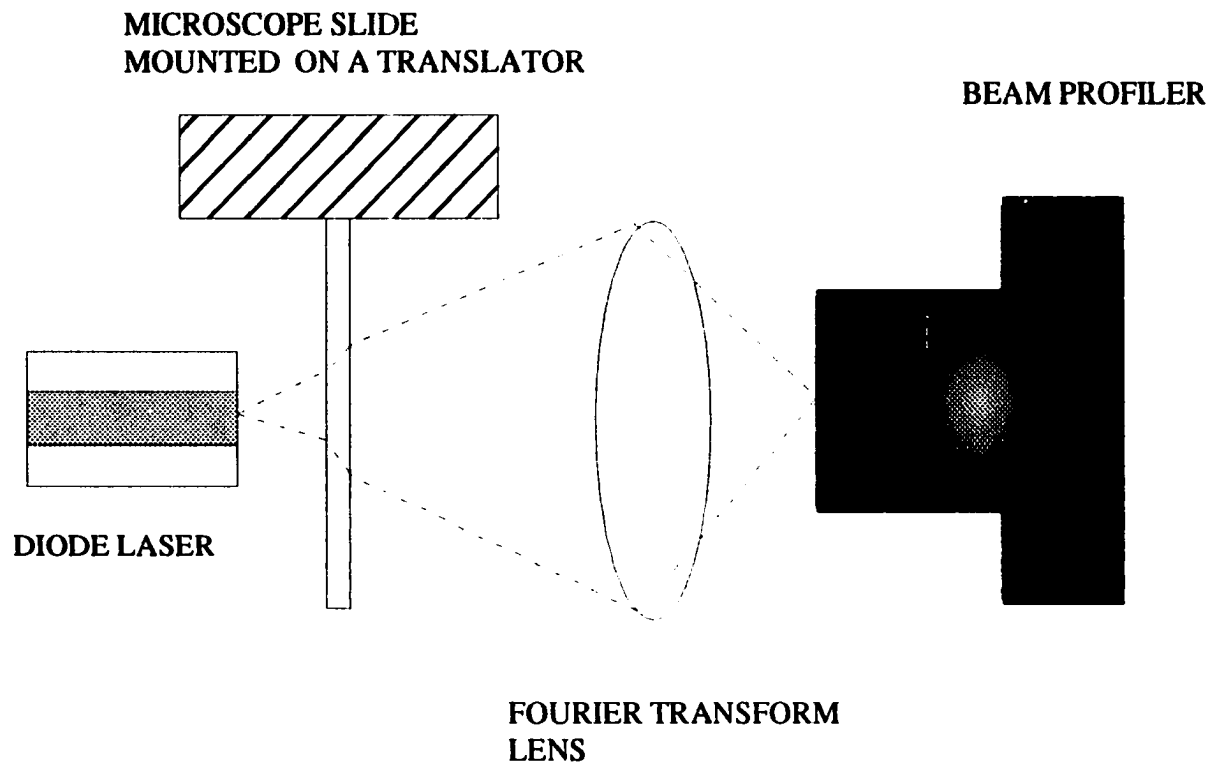


Figure 5.5 An experimental setup to evaluate the coupling distance of the diode laser sensor via the far field radiation pattern of the system.

6. LIMIT OF SENSITIVITY OF THE TERFENOL BASED DIODE LASER SENSOR

6.1 Operation of the Device

The operation of the sensor involves various components such as the diode laser, the photodetector and a transimpedance amplifier. Furthermore, the analog data will be sampled and stored for further signal processing. If the above components introduce random noise during the detection process, the sensitivity of the system will be reduced. In this chapter, we evaluate the theoretical limit to the sensitivity of the diode laser sensor. We have identified three different origins of random noise in the system:

- (a) photodetector pre-amplification noise and intrinsic photodetector dark current,
- (b) intrinsic diode laser noise such as spontaneous emission induced intensity noise , phase noise, and mode hopping noise due to temperature fluctuation,
- (c) current driver noise which modulates both the intensity and the emission frequency of the diode laser.

These noise sources are discussed and their impact on the detection sensitivity are quantified.

This chapter is divided into different sections. Section 6.2 discusses the random noise due to the photodetector preamplification. Section 6.3 studies the intrinsic diode laser noise and current driver induced fluctuations. Section 6.4 examines the noise performance of the

diode laser under the influence of an external cavity by modeling the external cavity sensor as a Mach Zender interferometer. Section 6.5 computes the total system noise assuming all noise sources are uncorrelated.

6.2. Photodetector Preamplification Noise

The interaction between the magnetostrictive Terfenol-D element and the external cavity sensor will be detected as an amplitude modulation in the output intensity of the diode laser. The photodetector and a transimpedance amplifier convert the optical signal to an electrical voltage. Thus, the sensitivity of the system depends on the noise level of the photodetector-amplifier module. The equivalent circuit model for a PIN photodetector, which is being used in all our experiments, is shown in Figure 6.1.

The small signal diode model of SPICE 2G6 has been used to simulate the PIN diode. Since the shot noise of the PIN diode is generated by the optical radiation, we have included an external current noise source to account for this noise contribution. The value of the capacitance, as the diode is operated with a photovoltaic mode, is calculated using data published by the manufacturer and a typical resistance value for the PIN diode is used. Although both thermal noise and shot noise can be found in a PIN diode, $1/f$ noise has not been observed with a detector operating in a photovoltaic mode [25].

Since the impedance of the photodetector is very high, it is important to have an op-amp with a low input current noise and a low dc bias current drift. We have performed the noise modeling with AD 754, a low noise FET-input op-amp from Analog Devices. In addition, the noise performance of the dc bias cancellation scheme described in Chapter 3 is also examined.

Assuming the detection system is limited by the photodetector pre-amp noise only, the

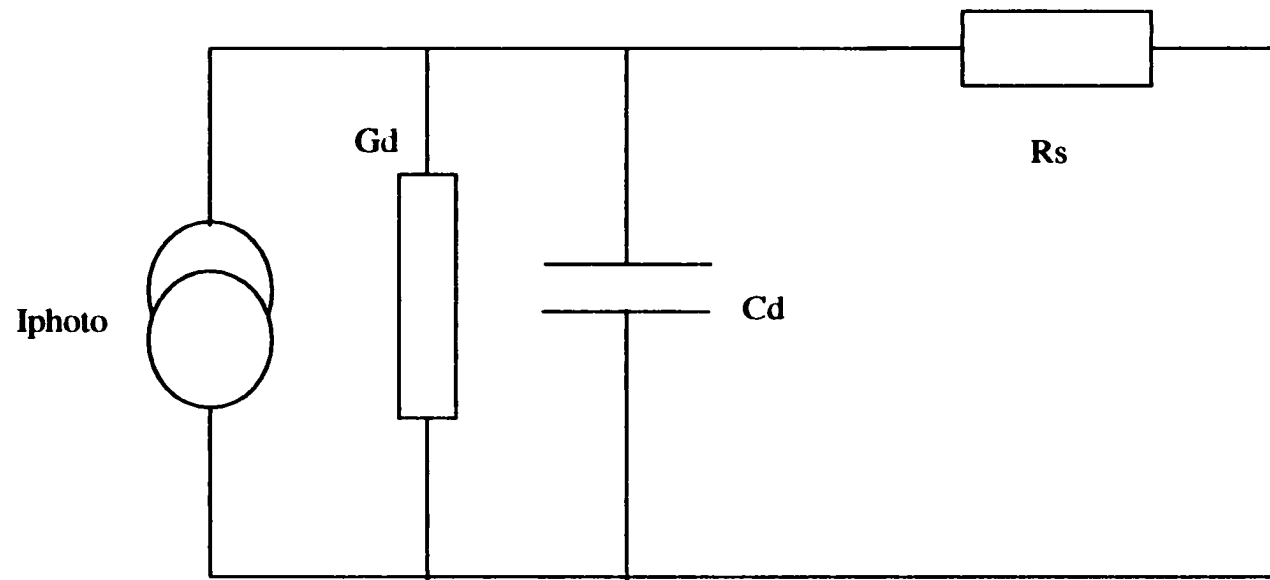


Figure 6.1 Small signal model of a reversed biased PIN photodetector. I_{photo} is the ideal current generator, G_d is the resistance of the diode when it is reversed biased, C_d is the junction capacitance, and R_s is the contact resistance.

minimum detectable distance can be calculated. Using a dry-cell battery as the power supply, the white noise of a properly designed pre-amp with the photodetector operating in a photovoltaic mode reached -140 dBV/root Hz with a 1 Hz bandwidth at 1 kHz. A 2 kilo-ohm feedback resistor was used while the bandwidth of the pre-amp was set at 10kHz in the above measurement [26]. It should be emphasized that the noise calculation used in this analysis assumes the diode laser sensor is biased to provide a linear response and is limited to a small signal regime. This assumption is valid when the movement of the Terfenol disk is limited to a small fraction of one spatial period (i.e., one-fourth of the emission wavelength) of the response curve of Figure D1 in Appendix D, which is valid in virtually all applications.

The dc offset of the amplitude modulated waveform is a measure of the steady state output level of the sensor. It should be emphasized that the shot noise of the photodetector is proportional to the square root of the background dc level. The measured noise background of -140 dBV in the above experiment was taken in a dark room [26]. Thus, the actual noise level of the photodetector during operation will be slightly higher. However proceeding with the assumption that the white noise level of the detector was -140 dBV/root Hz with a 1 Hz bandwidth, let θ represent the phase shift of the optical wave in traversing the coupling distance, d . The output of the sensor output versus phase shift can be described as:

$$V_{OUT} = V_{DC} [1 + \sin(2\theta)] \quad (6.1)$$

The ac response of the sensor is the derivative of the above transfer function. Assuming the dc output level of the photodetector as 1 volt, the minimum detectable phase shift will be 0.5×10^{-7} radian at 1 kHz.

$$\phi_{SHOT_NOISE} = 0.5 \times 10^{-7} \text{ radian} \quad (6.2)$$

6.3. Diode Laser Intensity Noise

Besides the photodetector pre-amplifier, the intensity noise of a diode laser can also limit the performance of the sensor. In this paragraph, we are going to calculate the impact of a diode laser's intensity noise on the sensor response. Both the current supply and the quantum nature (i.e. spontaneous emission) of the diode laser contributes to the noise level of the device. These contributions were evaluated separately. The quantum noise of the diode laser is usually described via the quantity known as the relative intensity noise (RIN), which is defined as the ratio of noise optical power squared to the mean power squared. If the noise is measured with a noise bandwidth of Δf , the RIN can be represented as follow [27]:

$$RIN = \frac{\delta I}{I} \quad (6.3)$$

where I is the average output power and δI is the noise power fluctuation.

Since all optical power must be measured with a photodetector, the quantum noise of the photodiode places a limit on the detectable RIN, which is :

$$I_{NOISE} = 3.2 \times 10^{-16} \sqrt{\langle I \rangle} B \text{ mA} \quad (6.4)$$

where I is the time averaged output power and B is the system measurement bandwidth.

When the RIN is larger than the above detection limit, the measurement is considered reliable. In the following discussion, the validity of the above condition has been assumed. The RIN varies depending on the level and modulation frequency of the injection current. At a modulation frequency of 50 MHz and a 1 Hz bandwidth, the RIN was measured at different levels of injection current and is shown in Figure 6.2. With an injection current at 1.5 times the lasing threshold, the RIN is in the order of 10^{-15} . However, the presence of $1/f$ noise, with a $1/f$ knee extending up to 10 KHz, raises the total noise level to 10^{-12} at 100 Hz.

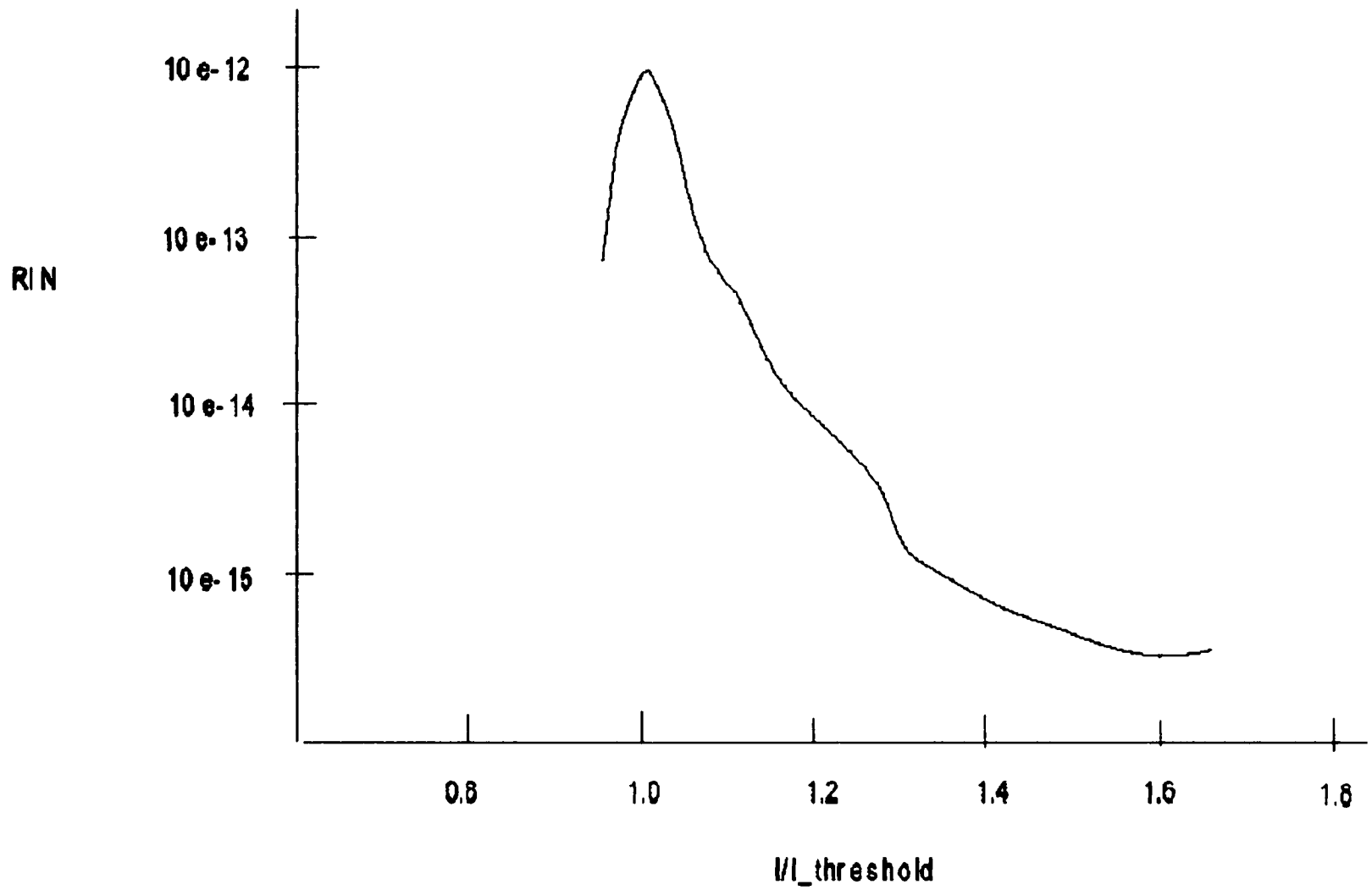


Figure 6.2 RIN of an index guided diode laser at a modulation frequency of 50 MHz.

RIN to a level of 10^{-12} at 100 Hz.

The experimental results on the RIN at 50 MHz and the RIN at low frequency is shown in Figure 6.3. Since the output of the sensor is obtained in units of volts, it is more convenient to deal with the square root of RIN instead of RIN. Estimating the RIN as 10^{-12} and repeating the calculation in the previous paragraph, we obtained a minimum detectable phase shift as:

$$\phi_{RIN} = 1.5 \times 10^{-6} \text{ radian} \quad (6.5)$$

In addition to the RIN, the emission intensity of the diode laser fluctuates as the injection current to the device varies. Both the voltage/current reference and the voltage noise of the dc error amplifier in the diode laser driver circuit contribute to the noise of the current source. A typical noise level of a commercial voltage reference is at about -124 dBV at 300 Hz with a 1 Hz bandwidth. Using the above parameter, the noise level of the current source was calculated using a dc resistance of 5 ohms for the diode laser assuming the turn-on delay was negligible and the bandwidth of the current source was far from the relaxation oscillation frequency. The amplitude modulation (am) conversion coefficient between the injection current and the output power is governed by the slope of the L-I curve. Thus, the intensity noise, L_{NOISE} , of the diode laser due to injection current fluctuation can be calculated as

$$L_{NOISE} = \delta i \times L/I \quad (6.6)$$

where L/I is the slope of the L-I characteristics of the diode laser sensor, and δi is the current noise in the current driver.

Similarly, following the previously formulation, the minimum detectable phase shift was:

$$\phi_{NOISE} = 1 \times 10^{-4} \text{ radian} \quad (6.7)$$

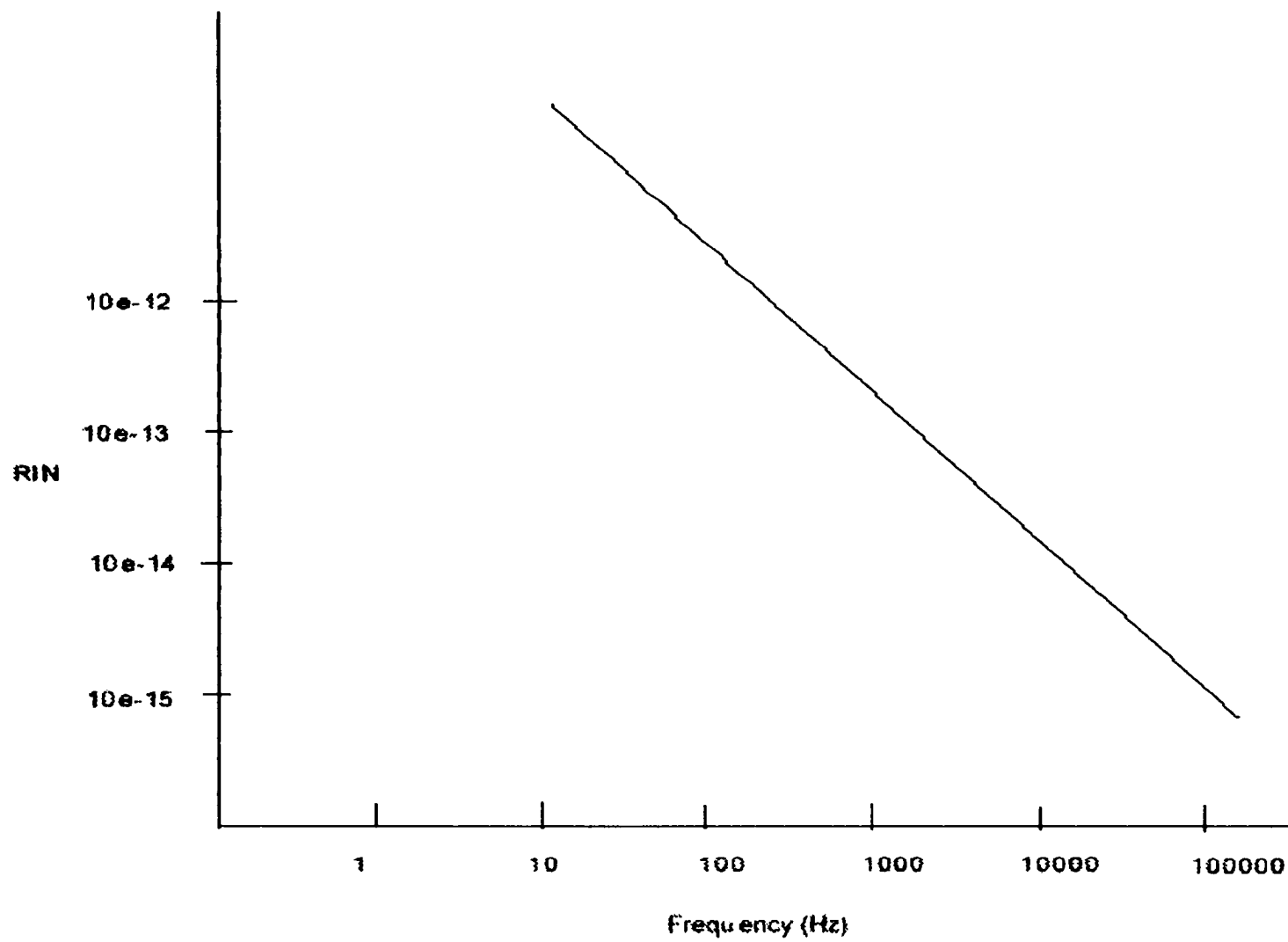


Figure 6.3 RIN of a diode laser at baseband frequency.

6.4 Diode Laser Phase Noise

In addition to intensity noise, the diode laser also possesses phase noise. The diode laser sensor operates as an interferometric sensor, as a result, the phase noise will be converted to intensity noise. The role of phase noise in a Mach-Zehnder type interferometer has been analyzed by Petermann [27]. The contribution of the diode laser phase noise in the detection limit of the external cavity diode laser sensor can be analyzed similarly. With the unfolded external cavity and by ignoring multiple reflection effect, the output of the diode laser is correlated with the resultant E-field at facet A of the diode laser image. The E-field can be represented as:

$$E_{facet}(t) = E(t) + E(t - 2\tau) \quad (6.8)$$

where $E_{facet}(t)$ is the electric field at the diode laser facet, and $E(t)$ is the electric field in the external cavity, and τ is the time to traverse the cavity.

This formulation ignores the following:

- (a) diffraction loss in the coupling process
- (b) a spatial modulation on the E-field due to a diverging wavefront
- (c) a spatial interaction aperture limited to the active layer area of the diode laser.

Although these assumptions seem to be rather crude, they provide a framework for calculating an “order-of-magnitude” estimate of the phase noise. The power at the output facet, $P(t)$, will then be obtained as in [27],

$$P(t) = P_{dc} [1 + \cos(\theta_{dc} + \delta\theta)] \quad (6.9)$$

where θ_{dc} is the total phase shift as the wave travels through a round-trip of the external cavity and $\delta\theta$ is the ac fluctuation between the round-trip.

The optimal bias point for the sensor keeps θ_{dc} at 120 degrees. As the linearity of the cosine curve deviates slowly from 90 degrees to 120 degrees. The above equation can be approximated as :

$$P(t) = P_{dc} [1 + \delta\epsilon] \quad (6.10)$$

Utilizing the relationship between the spectral density of the frequency noise and the phase noise, an equivalent RIN_{phase} can be calculated as:

$$RIN_{phase} = 4\pi\nu^2(\tau) \quad (6.11)$$

where τ is the time for traversing the cavity, and ν is the line-width of the laser

With a coupling distance of 10 micrometer, the RIN_{phase} of the sensor is on the order of 10^{-13} . Thus, the rms voltage fluctuation is on the order of $10^{-6.5}$. Following the previous calculation procedure, the minimum detectable phase shift, ϕ_{phase} , is:

$$\phi_{phase} = 0.25 \times 10^{-6.5} \text{ radian} \quad (6.12)$$

6.5 Total System Noise

Assuming the noise sources are not correlated, the the total rms fluctuation of the phase-shift can be calculated as the root mean square of the various contributing noise source. Judging from the above analysis, the system noise, ϕ_{TOTAL} , of the diode laser sensor will be limited by the noise of the current source, and can be calculated as:

$$\phi_{TOTAL} = (\phi_{Shot_Noise}^2 + \phi_{Lnoise}^2 + \phi_{RIN}^2 + \phi_{Phase}^2)^{0.5} = 0.1 \text{ milli - radian} \quad (6.13)$$

The above minimum detectable phase shift correspond to 12.4×10^{-3} nm in physical distance, which is comparable to the data obtain in [5]. With such a simple configuration, the

diode laser sensor can achieve an impression detection limit. In order to achieve the theoretical limit, the mechanical mounting must be isolated from ambient noise and a narrow-band detection system be employed. An example of using the external cavity diode laser sensor to investigate the thermal distortion in a thermal imaging setting was demonstrated in the Optics and Thermal Wave Laboratory at the Center of Non-Destructive Evaluation [28]. The experimental setup is briefly discussed in Appendix G.

7. CONCLUSIONS

This dissertation discusses the development and characterization of a novel diode laser magnetometer which can be used in a many metrology applications, ranging from surveillance to personal dosimetry. By coupling a highly magnetostrictive material, Terfenol-D, to the output facet of a diode laser, a sensitive ultra-short external cavity sensor is formed. The perturbation of the ac magnetic field is detected as an amplitude modulation of the laser output power.

The performance of a thin Terfenol-D disk was examined with a heterodyne interferometer at various excitation frequencies. The magnetoelastic response of the transducer was not uniform across the surface and substantial pinning of magnetostriction was observed around the perimeter of the transducer disk. The origin of this phenomenon is being discussed.

The electrical design and mechanical fabrication details of the optical magnetometer is being described, especially some of the critical alignment issues and imperfections regarding the diode laser manufacturing. A series of experiment was performed to study the general characteristics of the ultra-short external cavity sensor, and to characterize the performance of the magnetometer. With the construction technique as described, a pronounced mechanical resonance of the transducer disk was observed.

As a design aid to gain further insight into optimizing the magnetometer, a numerical study of the effect of the external reflector on the diode laser cavity is provided. The problem was treated as an electromagnetic scattering problem, in which an incident waveguide mode is scattered by an abruptly terminated dielectric-air-reflector interface. The plane wave expansion technique was used to solve for the modal reflectivity. The numerical data compares reasonably well with experimental data. However, a quantitative comparison is not

possible due to experimental difficulties. A proposed solution with a dielectric reflector is proposed.

The theoretical limitation of the device is analyzed in terms of relative intensity noise, phase noise and shot noise of the diode laser and the photodetector. The intensity noise of the sensor, as a result of the noise modulation by the current driver, is the limiting factor of the device.

In addition to the magnetometer application, other metrology application of the ultra-short external cavity sensor is described.

7.1 System Engineering

The manufacturing of the proposed magnetometer requires standard commercial off the shelf (COTS) electronics, which can be obtained at many sources without a significant delivery delay. The design of the fixture is simple enough that a standard milling machine suffices. However, it can benefit from a precision computer numerical controlled (CNC) milling machine. A significant amount of effort is required to set up an alignment fixture for manufacturing setting. A computerized automatic alignment technique is recommended, lowering the requirement for a highly trained optical technician. In addition, ultra-violet (UV) curable glue is desired so that the adjustment of the device can be locked in place quickly during the alignment process. Although the current design of the housing have not been optimized for a UV curable glue application, only slight modification may be required.

A modular approach is adopted in the design of the system allowing easy fault isolation. However, like many instruments with optical components, the alignment sensitive portion of the detector will be sealed with epoxy and is not user serviceable. It will be replaced as a plug-in module. The reliability and reproducibility of the device is ensured via

built-in testing and self-calibration. The micro-controller unit can issue an electronic check up during power-up sequence to verify the electrical integrity of the system while the calibration of the device can be obtained by pulsing a known amount of current into the coil for the servo loop and recording the response. The frequency response of the device can be calculated with a fast fourier transform (FFT).

7.2. Current Status

A pocket-size magnetometer prototype as described in this dissertation was fabricated. The performance of the device was evaluated at various excitation frequency. A 8-bit micro-controller unit was also fabricated to record and analyze the analog output data in real-time. Currently, a simple FFT routine is used to calculate the frequency content of the excitation magnetic fields. The data is displayed on a LCD display. A chassis, which have not been fabricated, is required to finalize integration of the system and to prepare the magnetometer for field testing. With the current form factor, a vector magnetometer can be integrated by putting three miniature magnetometers in three orthogonal axis. Additional magnetometer can be added to implement a first order or a second order gradiometer configuration, which helps to reduce the effect of motion induced frequency noise.

7.3 Future Direction

The computer design aid developed in this dissertation can be extended to account for tilting and other manufacturing imperfection issues. Furthermore, a theoretical investigation of the ac magneto-elastic property of the transducer should be carried out to verify the experimental observations. With a minimal amount of integration effort, the unit can be

engineered and be used in a field test for system validation. Last but not least, taking advantage of the latest battery technology and the availability of low threshold quantum well diode laser, a re-examination of the power budget and component choice should be carried out.

APPENDIX A: OPERATING PRINCIPLE OF A HETERODYNE INTERFEROMETER

A1. THEORY OF OPERATION [29]

A1.1 Optical Setup

The OP35-0 is a Mach-Zehnder heterodyne interferometer. A variable ratio of splitting of the light from the built-in 5 mW He-Ne laser (or user supplied Argon laser) is achieved into an acousto-optic device (AO on Figure A1).

Order zero out of AO goes undeflected through a Polarizing Beam Splitter (PBS), a Variable Distance Focusing Optics (FO) and a Quarter-Wave Retardation plate (QW) and is focused at the sample surface. Correct angular position of OW will have the light returning from the sample surface be reflected at PBS in direction of the detector DET. Order 1 out of AO is frequency shifted by 40 MHz with respect to order zero. It is superimposed onto the sample beam at the Beam Mixer BM and at DET. The interference signal at 40 MHz is phase modulated by the displacement of the sample surface.

The phase information is Electronically Demodulated in the Electronics unit of the OP35-O (ED). This unit includes an automatic gain control to make the calibration of the output signal independent of the amplitude of the carrier signal. It also includes a phase demodulator wherein signals within a band selectable from either 1 KHz or 10 KHz and in both cases up to 35 MHz are demodulated.

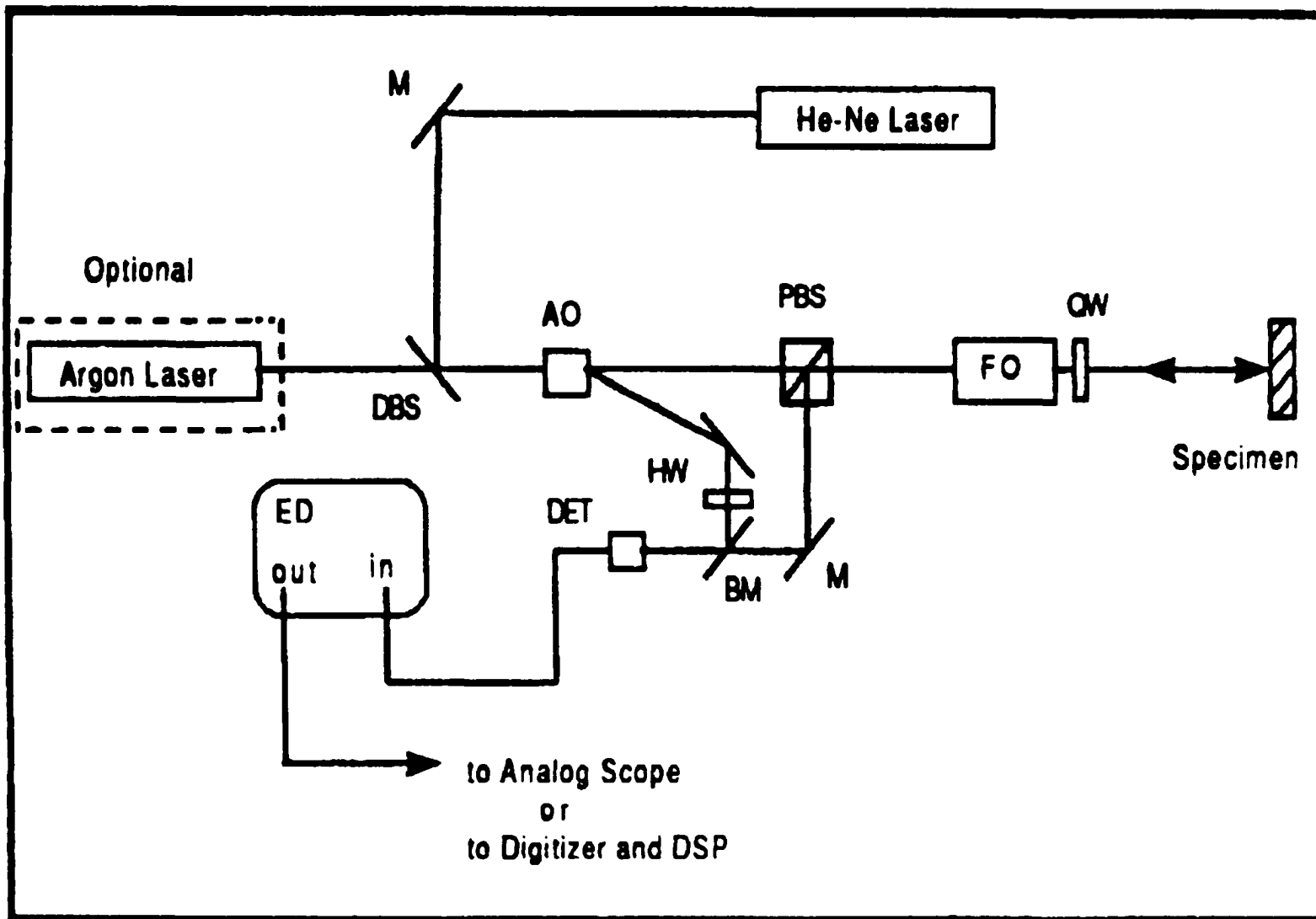


Figure A1 Optical setup for the OP-35 heterodyne interferometer

A1.2 Electronics Setup

The signal which is incident at the RF port of the mixer comes from the AC output of the detector and can be written as follows:

$$\begin{aligned} \cos(2\pi f_b t + \Omega(t) + 4\pi\delta(t)/\lambda) &= \cos(2\pi f_b t + \Omega(t))\cos(4\pi\delta(t)/\lambda) \\ &\quad - \sin(2\pi f_b t + \Omega(t))\sin(4\pi\delta(t)/\lambda) \end{aligned} \quad (\text{A1.1})$$

where f_b is the carrier frequency (40 MHz) due to frequency shifting of the reference beam by the Bragg cell, $\Omega(t)$ is some phase term representing the effect of laser phase fluctuations as well as vibrations in the environment, and $\delta(t)$ is the ultrasonic displacement.

Within the small displacement approximation (ultrasonic displacement amplitude smaller than $\lambda/8=800$ Angstrom), this can be rewritten as:

$$\cos(2\pi f_b t + \Omega(t)) - 4\pi\delta(t)/\lambda \sin(2\pi f_b t + \Omega(t)) \quad (\text{A1.2})$$

At the LO port of the mixer, the signal from the VCO is always in quadrature with the cosine term above. Hence, in the mixer which is a multiplier, the mathematical operation which occurs can be described as:

$$\{\cos(2\pi f_b t + \Omega(t)) - 4\pi\delta(t)/\lambda \sin(2\pi f_b t + \Omega(t))\} \sin(2\pi f_b t + \Omega(t)) \quad (\text{A1.3})$$

With the notation in (A1.4), (A1.3) can be simplified to

$$A = 2\pi f_b t + \Omega(t) \quad (\text{A1.4})$$

$$\{\cos(A) - [4\pi\delta(t)/\lambda]\sin(A)\} \sin(A) = -2\pi\delta(t)/\lambda + 2\pi\delta(t)/\lambda \cos(2A) + 0.5\sin(2A) \quad (\text{A1.5})$$

which is the voltage signal at the IF output port from the mixer.

The low-pass filter with cut-off at 35 MHz, at the output of the electronics, will reject the last two terms on the right-hand side of this equation and we will be left with only $2\pi\delta(t)/\lambda$ at the output of the electronics. Actually, this term is multiplied by some constant K and the calibration technique will take this into account. Now, let us suppose that $\delta(t)$ results from some CW deformation of the sample surface so that $\delta(t) = U\sin(2\pi f_0 t + \beta(t))$. Then, at the output:

$$V_{\text{out}}(t) = 2\pi K/\lambda U \sin(2\pi f_0 t + \beta(t)) \quad (\text{A1.6})$$

which shows that the phase information is conserved. The best experimental verification of this is when, with the same electronics used in conjunction now with the OP-35-I/O, we detect the In-Plane and the Out-Plane components of the ultrasonic displacement caused by the passage of a surface Rayleigh wave. We know from theory [30] that there is a phase shift of 90 degrees between the In-Plane and the Out-Plane displacements. This has been verified experimentally with a good accuracy and is reported in [31]. With some averaging (16 acquisitions) of the signal in order to obtain a better signal-to-noise ratio, this 90 degree phase shift can be measured with an accuracy better than 2%.

Finally, we have verified experimentally that a surface displacement in the direction of the interferometer will result in a negative signal on the scope. Hence, positive signal means displacement in the direction away from the interferometer. This has been verified by measuring with an OF-35-O the slow motion of the surface of a composite materials sample when heated by a laser pulse in the thermo-elastic regime. The first deformation of the surface always is bump-like because of the local thermal expansion of the material.

When monitoring a large amplitude ($> \lambda/8$) ultrasonic displacement with an OP-35. It can be shown that after some mathematical manipulations, and taking into account the rejection of high frequencies by the low-pass filter,

$$V_{out}(t) = -0.5 \sin(4\pi\delta(t)/\lambda) \quad (A1.7)$$

Using $\delta(t) = U \sin(2\pi f_u t + \beta(t))$ and using the Bessel function identities

$$\sin[U \sin(\omega t)] = 2J_1(U) \sin \omega t + 2J_3(U) \sin 3\omega t + \dots \quad (A1.8)$$

This yields a voltage signal at the fundamental frequency f_u modulated by the different harmonics $3f$, $5f$, etc... The greater the amplitude U , the more important become the contributions from the different superior harmonics. ULTRA OPTEC is presently working at the development of an electronic kit which would allow to process in real time the output of the OP-35's electronics in such cases. This will expand considerably the field of applications of the OP-35's.

APPENDIX B: DATA SHEETS OF THE DIODE LASER ML-4403 USED IN THIS STUDY

DESCRIPTION

ML4XX2A is an AlGaAs semiconductor laser which provides a stable, single transverse mode oscillation with emission wavelength of 780nm and standard light output of 3mW.

ML4XX2 uses a hermetically sealed package incorporating the photodiode for optical output monitoring. This high-performance, highly reliable, and long-life semiconductor laser is suitable for such applications as optical disk reading and optical information processing.

FEATURES

- Low noise
- Built-in monitor photodiode
- High reliability, long operation life
- Multiple longitudinal mode

APPLICATION

Reading memory disk, video disk player, data link

ABSOLUTE MAXIMUM RATINGS

Symbol	Parameter	Conditions	Rating	Unit
P _o	Light output power	CW	5	mW
		Pulse (Note 1)	6	
V _{RL}	Reverse voltage (Laser diode)	-	2	V
V _{RD}	Reverse voltage (Photodiode)	-	15	V
I _{FD}	Forward current (Photodiode)	-	10	mA
T _c	Case temperature	-	-40~+60	°C
T _{stg}	Storage temperature	-	-55~+100	°C

Note 1: Duty less than 50%, pulse width less than 1 μ s.

ELECTRICAL/OPTICAL CHARACTERISTICS (T_c = 25 °C)

Symbol	Parameter	Test conditions	Limits			Unit
			Min.	Typ.	Max.	
I _{th}	Threshold current	CW	-	40	60	mA
I _{op}	Operating current	CW, P _o = 3mW	-	50	70	mA
V _{op}	Operating voltage	CW, P _o = 3mW	-	1.8	2.5	V
η	Slope efficiency	CW, P _o = 3mW	-	0.32	-	mW/mA
λ_p	Peak oscillation wavelength	CW, P _o = 3mW	765	780	795	nm
$\theta_{//}$	Beam divergence angle (parallel)	CW, P _o = 3mW	8	11	15	deg.
θ_{\perp}	Beam divergence angle (perpendicular)	CW, P _o = 3mW	20	33	45	deg.
I _m	Monitoring output current (Photodiode)	CW, P _o = 3mW, V _{RD} = 1V, R _L = 10 Ω (Note 1)	0.15	0.4	0.7	mA
I _o	Dark current (Photodiode)	V _{RD} = 10V	-	-	0.5	μ A
C _t	Total capacitance (Photodiode)	V _{RD} = 0V, f = 1MHz	-	7	-	pF

Note 2: R_L is load resistance of the Photodiode.

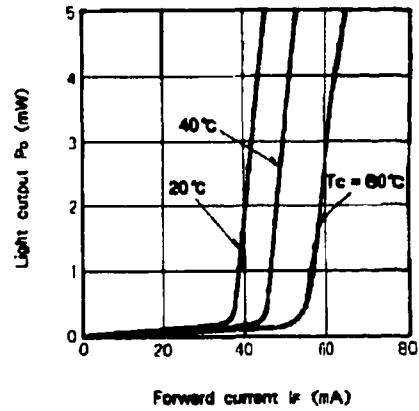
SAMPLE CHARACTERISTICS

Light output vs. forward current

Typical light output vs. forward current characteristics are shown in Fig.1. The threshold current for lasing is typically 40mA at room temperature. Above the threshold, the light output increases linearly with current, and no kinks are observed in the curves. An optical power of about 3mW is obtained at $I_{th} + 10mA$.

Because I_{th} and slope efficiency η (dP_o/dI_f) is temperature dependent, obtaining a constant output at varying temperatures requires to control the case temperature T_c or the laser current. (Control the case temperature or laser current such that the output current of the built-in monitor PD becomes constant.)

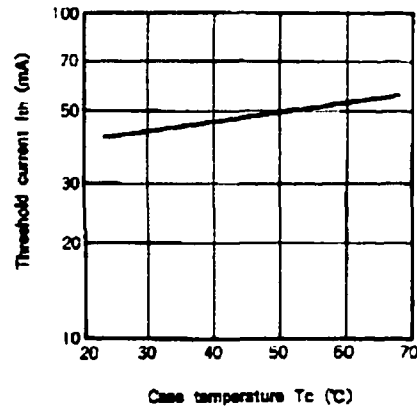
Fig. 1 Light output vs. forward current



Temperature dependence of threshold current(I_{th})

A typical temperature dependence of the threshold current is shown in Fig.2. The characteristic T_0 of the threshold current is typically 140K in $T_c \leq 70^\circ C$, where the definition of T_0 is $I_{th} \propto \exp(T_c/T_0)$

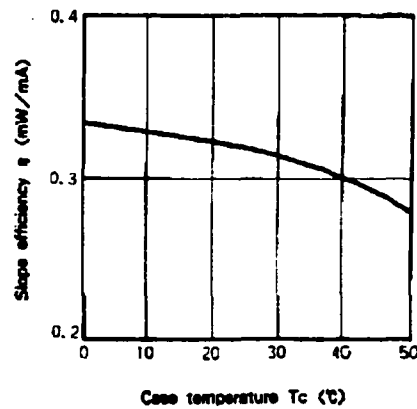
Fig. 2 Temperature dependence of threshold current



Temperature dependence of slope efficiency

A typical temperature dependence of the slope efficiency η is shown in Fig.3. The gradient is $-0.001mW/mA/^\circ C$

Fig. 3 Temperature dependence of slope efficiency



Far-field pattern

ML4XX2A oscillates in the standard transverse mode (TE_{00}) regardless of the optical output level. They have a typical emitting area (size of near-field pattern) of $2.1 \mu m^2$. Fig.7 and Fig.8 show typical far-field radiation patterns in "parallel" and "perpendicular" planes.

The full angles at half maximum points (FAHM) are typically 11° and 33° .

Fig. 7 Far-field patterns in plane parallel to heterojunctions $\theta //$

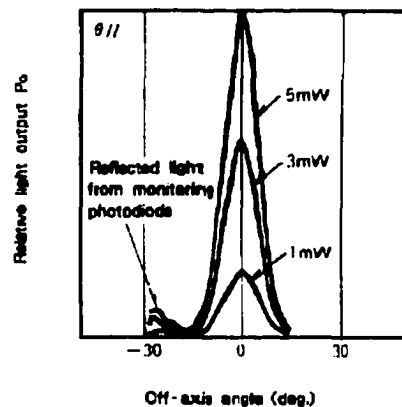
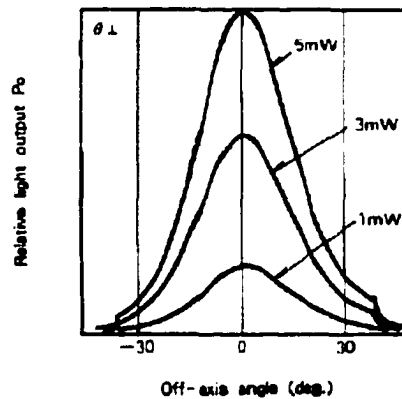


Fig. 8 Far-field patterns in plane perpendicular to heterojunctions $\theta \perp$

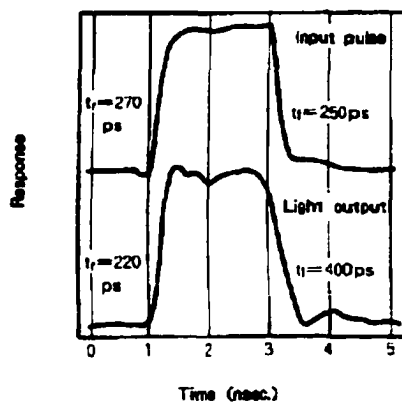


Pulse response waveform

In the digital optical transmission systems, the response waveform and speed of the light output against the input current pulse waveform is one of the main concerns.

Generally, the laser diode is biased up to near the threshold current to minimize oscillation delay time. Figure 9 shows a standard response waveform obtained by biasing ML4XX2A to lth and applying a square pulse current (top of Fig.9) up to 3mW. The rise time and the fall time in Fig.9 are typically 0.3ns and 0.4ns. They are limited by response speed of the detector.

Fig. 9 Pulse response waveform



S/N vs. optical feedback ratio

S/N vs optical feedback ratio, where the frequency is 20kHz and the bandwidth is 300Hz is shown in Fig.13.

That where the frequency is 10MHz and the bandwidth is 300kHz is shown in Fig.14.

The S/N value is the worst value obtained at case temperatures of 25°C to 50°C.

Fig. 13 S/N vs. optical feedback ratio
f=20kHz, BW=300Hz, T_c=25-50°C

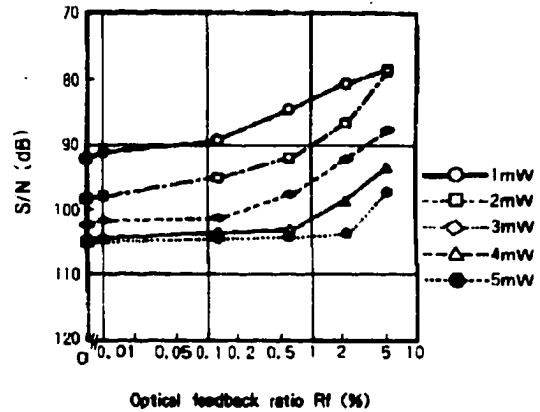
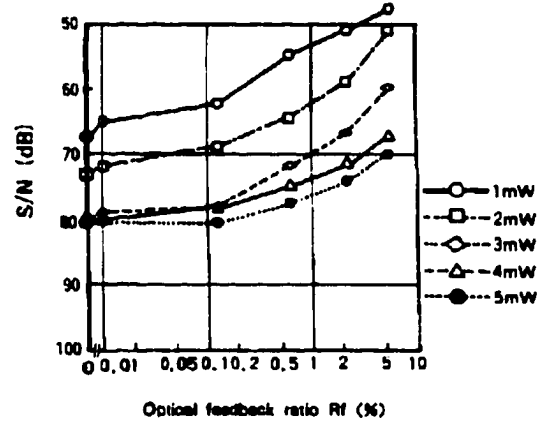


Fig. 14 S/N vs. optical feedback ratio
f=10MHz, BW=300kHz, T_c=25-50°C



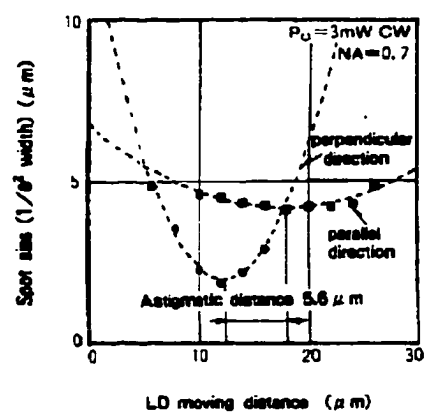
Astigmatic distance

There seems to be a difference in luminous point in the parallel and perpendicular direction with laser beam. This distance between the two points is the astigmatic focal distance. Therefore, when the laser beam is focused, there is a difference in focal point in the two directions, making it difficult to converge the beam spot to the diffraction limit.

The typical astigmatic focal distance at NA = 0.7 of ML4XX2A is shown in Fig.15.

The LD position which minimizes the horizontal and vertical spot diameters is obtained. The astigmatic distance is the difference in moved distances thus obtained.

Fig. 15 Astigmatic distance



APPENDIX C: SPICE LISTINGS FOR VARIOUS ANALOG CIRCUITS**C.1 PHOTODETECTOR PERAMP**

```
.inc AD745K.cir
Cpd 2 0 80p
Rin 1 0 10k
Cin 1 0 2080p
Rfbk 2 6 10k
Cfbk 2 3 2000p
Rlp 3 6 33.2
Clp 6 0 0.127u
X1 1 2 4 5 3 AD745K
.probe
VCC 4 0 12
VEE 5 0 -12
IINPUT 2 0 1E-06 AC 0.001 0
.AC DEC 50 1e3 2E+07
.NOISE V(6) IINPUT 20
.PRINT AC V(6)
.PRINT NOISE INOISE(DB) INOISE(P) ONOISE(DB) ONOISE(P)
```

C.2 PHOTODETECTOR PERAMP W/ DC NULLING

```
*.inc AD745K.cir
.inc AD743.cir
```

Cpd 2 0 80p

Rin 1 0 20k

Cin 1 0 440p

Rfbk 2 6 20k

Cfbk 2 3 360p

Rlp 3 6 62

Clp 6 0 0.127u

X1 1 2 4 5 3 AD743

X2 12 0 4 5 7 OP-27E

Rout 2 7 10k

***Integrator Cap**

***Cint 6 7 10pF**

*** OUTPUT LPF**

Rnull 6 9 200k

Cnull 9 0 1000n

Ccomp 10 0 1000n

Rcomp 9 10 200k

Ccomp2 11 0 1000n

Rcomp2 10 11 200k

Ccomp3 12 0 1000n

Rcomp3 11 12 200k

```
.probe  
VCC 4 0 12  
VEE 5 0 -12  
IINPUT 2 0 dc -1E-03 AC 0.001 0  
.AC DEC 20 1 2E+07  
.NOISE V(6) IINPUT 20  
.PRINT AC V(6)  
.PRINT NOISE INOISE(DB) INOISE(P) ONOISE(DB) ONOISE(P)
```

C.3 Laser Diode Driver

* With the LD Anode at GND

* Ver 6

```
.inc IRFZ12.cir
```

```
.inc op27.cir
```

```
Rctrl 2 7 50
```

```
Cctrl 2 7 0.1u
```

```
Roffset 7 6 5
```

```
Rsense 9 7 10
```

```
D1 0 1 Dled
```

```
X2 1 8 9 IRFZ12
```

```
x1 2 3 5 6 4 op-27
```

```
rcomp 4 8 50
```

rcomp2 9 3 500

ccomp 4 3 0.001u

.MODEL Dled D(IS=1E-15, RS=4, VJ=1.8)

.probe

VSS 1 0 9

VCC 5 0 9

VEE 6 0 -9

IREF 1 2 0.0022 AC 0.001 0

.DC RCTRL 0.1 1000 100

.AC DEC 20 10 5E+07

.NOISE V(9,7) IREF 10

.PRINT DC IM(RSENSE)

.PRINT AC IDB(RSENSE) IP(RSENSE)

.PRINT NOISE INOISE(DB) INOISE(P) ONOISE(DB) ONOISE(P)

.end ; end lddrv.cir

C4. OP-27 SPICE MODEL

* OP-27 SPICE Macro-model 12/90, Rev. B

* JCB / PMI

*

* Revision History:

* REV. B

* Re-ordered subcircuit call out nodes to put the

* output node last.

* Changed Ios from 7E-9 to 3.5E-9

* Added F1 and F2 to fix short circuit current limit.

*

*

* Copyright 1990 by Analog Devices, Inc.

*

* Refer to "README.DOC" file for License Statement. Use of this model

* indicates your acceptance with the terms and provisions in the License Statement.

*

* Node assignments

* non-inverting input

* | inverting input

* || positive supply

* ||| negative supply

* ||| | output

* ||| | |

.SUBCKT OP-27 1 2 99 50 39

*

* INPUT STAGE & POLE AT 80 MHZ

*

R3 5 97 0.0619

R4 6 97 0.0619

CIN 1 2 4E-12

C2 5 6 16.07E-9

I1 4 51 1

IOS 1 2 3.5E-9

EOS 9 10 POLY(1) 30 33 10E-6 1

Q1 5 2 7 QX

Q2 6 9 8 QX

R5 7 4 0.0107

R6 8 4 0.0107

D1 2 1 DX

D2 1 2 DX

EN 10 1 12 0 1

GN1 0 2 15 0 1

GN2 0 1 18 0 1

*

EREF 98 0 33 0 1

EPLUS 97 0 99 0 1

ENEG 51 0 50 0 1

*

*** VOLTAGE NOISE SOURCE WITH FLICKER NOISE**

*

DN1 11 12 DEN

DN2 12 13 DEN

VN1 11 0 DC 2

VN2 0 13 DC 2

*

*** CURRENT NOISE SOURCE WITH FLICKER NOISE**

*

DN3 14 15 DIN

DN4 15 16 DIN

VN3 14 0 DC 2

VN4 0 16 DC 2

*

*** SECOND CURRENT NOISE SOURCE**

*

DN5 17 18 DIN

DN6 18 19 DIN

VN5 17 0 DC 2

VN6 0 19 DC 2

*

*** GAIN STAGE & DOMINANT POLE AT 4.0 HZ**

*

R7 20 98 111.5E3

C3 20 98 357E-9

G1 98 20 5 6 16.15

V1 97 21 1.2

V2 22 51 1.2

D5 20 21 DX

D6 22 20 DX

*

*** POLE - ZERO AT 2.9MHZ / 6MHZ**

*

R8 23 98 1

R9 23 24 0.935

C4 24 98 28.4E-9

G2 98 23 20 33 1

*

* ZERO - POLE AT 6.8MHZ / 40MHZ

*

R10 25 26 1

R11 26 98 4.88

L1 26 98 19.4E-9

G3 98 25 23 33 1

*

* POLE AT 60 MHZ

*

R12 27 98 1

C5 27 98 2.65E-9

G4 98 27 25 33 1

*

* ZERO AT 28 MHZ

*

R13 28 29 1

C6 28 29 -5.68E-9

R14 29 98 1E-6

E1 28 98 27 33 1E6

*

* COMMON-MODE GAIN NETWORK WITH ZERO AT 3 KHZ

*

R15 30 31 1

L2 31 98 53.1E-6

G5 98 30 POLY(2) 2 33 1 33 0 250.5E-9 250.5E-9

D7 30 97 DX

D8 51 30 DX

*

* POLE AT 80 MHZ

*

R16 32 98 1

C7 32 98 1.99E-9

G6 98 32 29 33 1

*

* OUTPUT STAGE

*

R17 33 97 1

R18 33 51 1

GSY 99 50 POLY(1) 99 50 1.8E-3 40E-6

F1 34 0 V3 1

F2 0 34 V4 1

R19 34 99 180

R20 34 50 180

L3 34 39 1E-7

G7 37 50 32 34 5.56E-3
G8 38 50 34 32 5.56E-3
G9 34 99 99 32 5.56E-3
G10 50 34 32 50 5.56E-3
V3 35 34 2.5
V4 34 36 3.1
D9 32 35 DX
D10 36 32 DX
D11 99 37 DX
D12 99 38 DX
D13 50 37 DY
D14 50 38 DY

*

* MODELS USED

*

.MODEL QX NPN(BF=50E6)

.MODEL DX D(IS=1E-15)

.MODEL DY D(IS=1E-15 BV=50)

.MODEL DEN D(IS=1E-12, RS=1.09K, KF=1.08E-16, AF=1)

.MODEL DIN D(IS=1E-12, RS=19.3E-6, KF=4.28E-15, AF=1)

.ENDS OP-27

C5. AD745 SPICE MODEL

* AD745J SPICE Macro-model 3/92, Rev. A

* ARG / PMI

*

* This version of the AD745 model simulates the worst case

* parameters of the 'J' grade. The worst case parameters

* used correspond to those in the data sheet.

*

*

* Copyright 1992 by Analog Devices, Inc.

*

* Refer to "README.DOC" file for License Statement. Use of this model

* indicates your acceptance with the terms and provisions in the License Statement.

*

* Node assignments

* non-inverting input

* | inverting input

* | | positive supply

* | | | negative supply

* | | | | output

* | | | | |

.SUBCKT AD745J 3 2 99 50 37

*

* INPUT STAGE AND POLE AT 54MHZ

*

II 97 1 1

J1 5 2 1 JX

J2 6 4 1 JX

CIN 2 3 20E-12

IOS 3 2 75E-12

EN 7 3 9 0 1

GN1 0 2 12 0 1E-6

GN2 0 3 15 0 1E-6

EOS 4 7 POLY(1) 31 52 1E-3 1

R1 5 51 86.842E-3

R2 6 51 86.842E-3

C1 5 6 16.969E-9

EPOS 97 0 99 0 1

ENEG 51 0 50 0 1

EREF 98 0 52 0 1

*

*** VOLTAGE NOISE SOURCE WITH FLICKER NOISE**

*

VN1 8 0 DC 2

VN2 0 10 DC 2

DN1 8 9 DEN

DN2 9 10 DEN

*

*** CURRENT NOISE SOURCE WITH FLICKER NOISE**

*

VN3 11 0 DC 10

VN4 0 13 DC 10

DN3 11 12 DIN

DN4 12 13 DIN

*

*** CURRENT NOISE SOURCE WITH FLICKER NOISE**

*

VN5 14 0 DC 10

VN6 0 16 DC 10

DN5 14 15 DIN

DN6 15 16 DIN

*

*** GAIN STAGE AND DOMINANT POLE AT 22.9HZ**

*

R3 17 98 86.842E3

C2 17 98 80E-9

G1 98 17 5 6 11.515

V1 97 18 .727

V2 19 51 1.893

D1 17 18 DX

D2 19 17 DX

*

*** POLE AT 30MHZ**

*

R4 23 98 1

C3 23 98 5.305E-9

G2 98 23 17 52 1

*

* POLE AT 30MHZ

*

R5 24 98 1

C4 24 98 5.305E-9

G3 98 24 23 52 1

*

* NEGATIVE ZERO AT -54MHZ

*

R6 25 26 1

C5 25 26 -2.947E-9

R7 26 98 1E-6

E1 25 98 24 52 1E6

*

* POLE / ZERO AT 2MHZ / 2.25MHZ

*

R8 27 98 1

R9 27 28 8

C6 28 98 8.842E-9

G4 98 27 26 52 1

*

* COMMON MODE GAIN STAGE WITH ZERO AT 126KHZ

*

E2 29 30 2 52 0.5

E3 30 98 3 52 0.5

R10 29 31 1

R11 31 98 100E-6

C7 29 31 1.264E-6

*

*** REFERENCE NODE AND OUTPUT STAGE**

*

RMP1 97 52 1

RMP2 52 51 1

GSY 99 50 POLY(1) 99 50 9.625E-3 12.5E-6

R13 99 36 200

R14 36 50 200

L1 36 37 1E-10

G5 34 50 27 36 5E-3

G6 35 50 36 27 5E-3

G7 36 99 99 27 5E-3

G8 50 36 27 50 5E-3

V3 32 36 1.55

V4 36 33 1.55

D3 27 32 DX

D4 33 27 DX

D5 99 34 DX

D6 99 35 DX

D7 50 34 DY

D8 50 35 DY

F1 36 0 V3 1

F2 0 36 V4 1

*

* MODELS USED

*

.MODEL JX PJF(BETA=66.299, VTO=-1.5 IS=400E-12

.MODEL DX D(IS=1E-15)

.MODEL DY D(IS=1E-15, BV=50)

.MODEL DEN D(RS=1.931E3, KF=2.278E-15, AF=1)

.MODEL DIN D(RS=5.277E3, KF=42.593E-15, AF=1)

.ENDS AD745J

APPENDIX D. BASIC PROPERTIES OF AN EXTERNAL CAVITY DIODE LASER SENSOR

D1.1 Origin Of Output Power Modulation Of An External Cavity Diode Laser Sensor [32]

The output power modulation property can be attributed to the modification of the effective facet reflectivity by the external reflector of the ultra-short external cavity. When the external cavity length creates a resonance condition, the effective facet reflectivity will be increased and an anti-resonance condition decreases the effective facet reflectivity. Since the lasing threshold is a function of the facet reflectivity, the output power will be modulated by the external cavity length. A typical response curve for the diode laser sensor is shown in Figure D1.1.

In addition to sensor applications, the ultra-short external cavity diode laser has also been used as an optical readout device for magneto-optical phase-change recording medium. The variation of the output power versus the external cavity length for different reflectivity of the recording medium is shown in Figure D1.1(b). It should be noted that even though the reflectivity of the external reflector (the recording medium in this case) is only 4%, a significant amount of output power modulation can be observed, provided the external cavity length is extremely short (i.e., less than one wavelength).

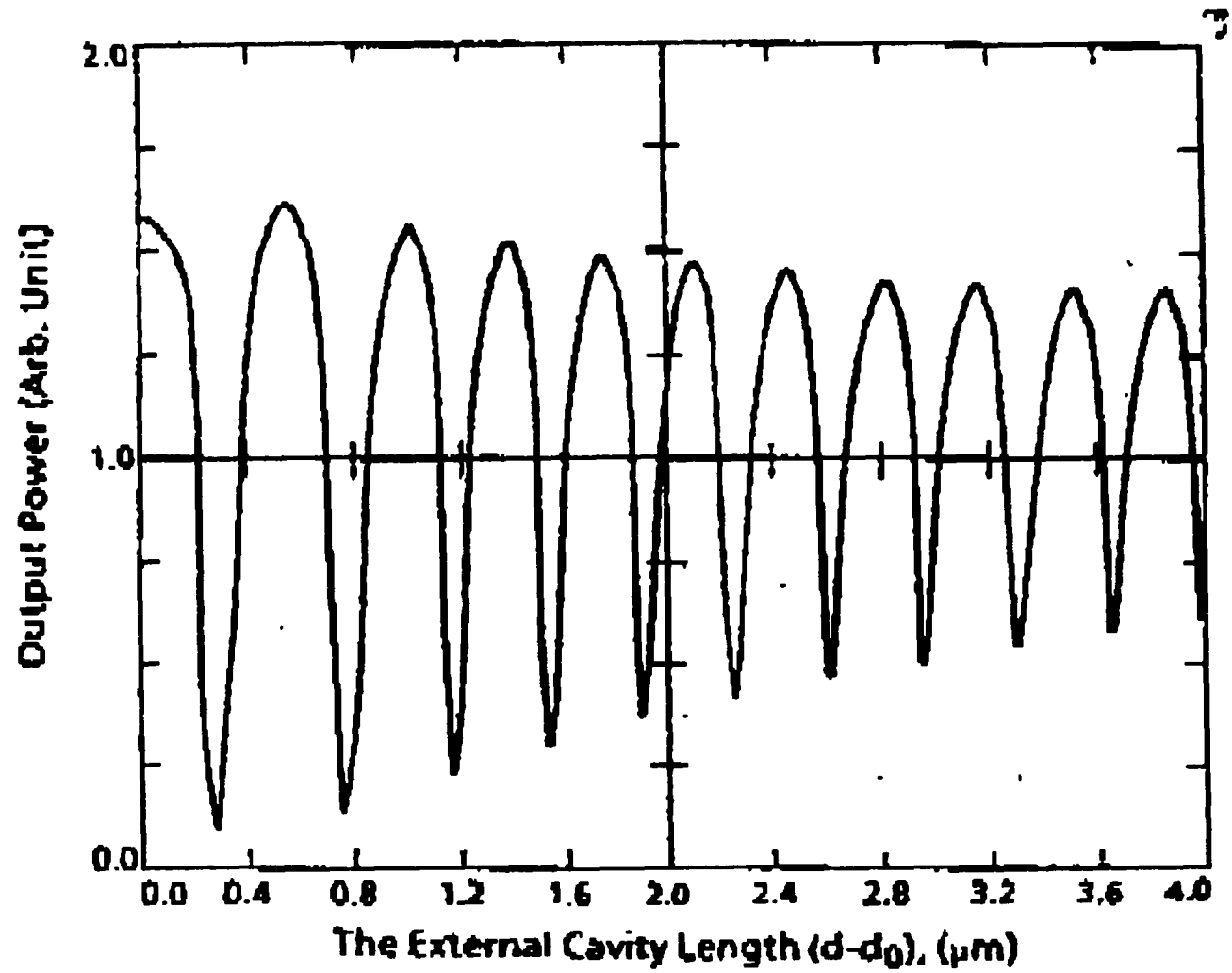


Figure D1.1 (a) Experimental result of output power versus external cavity length. The starting position is not exactly known. A 99% mirror was used as the external reflector.

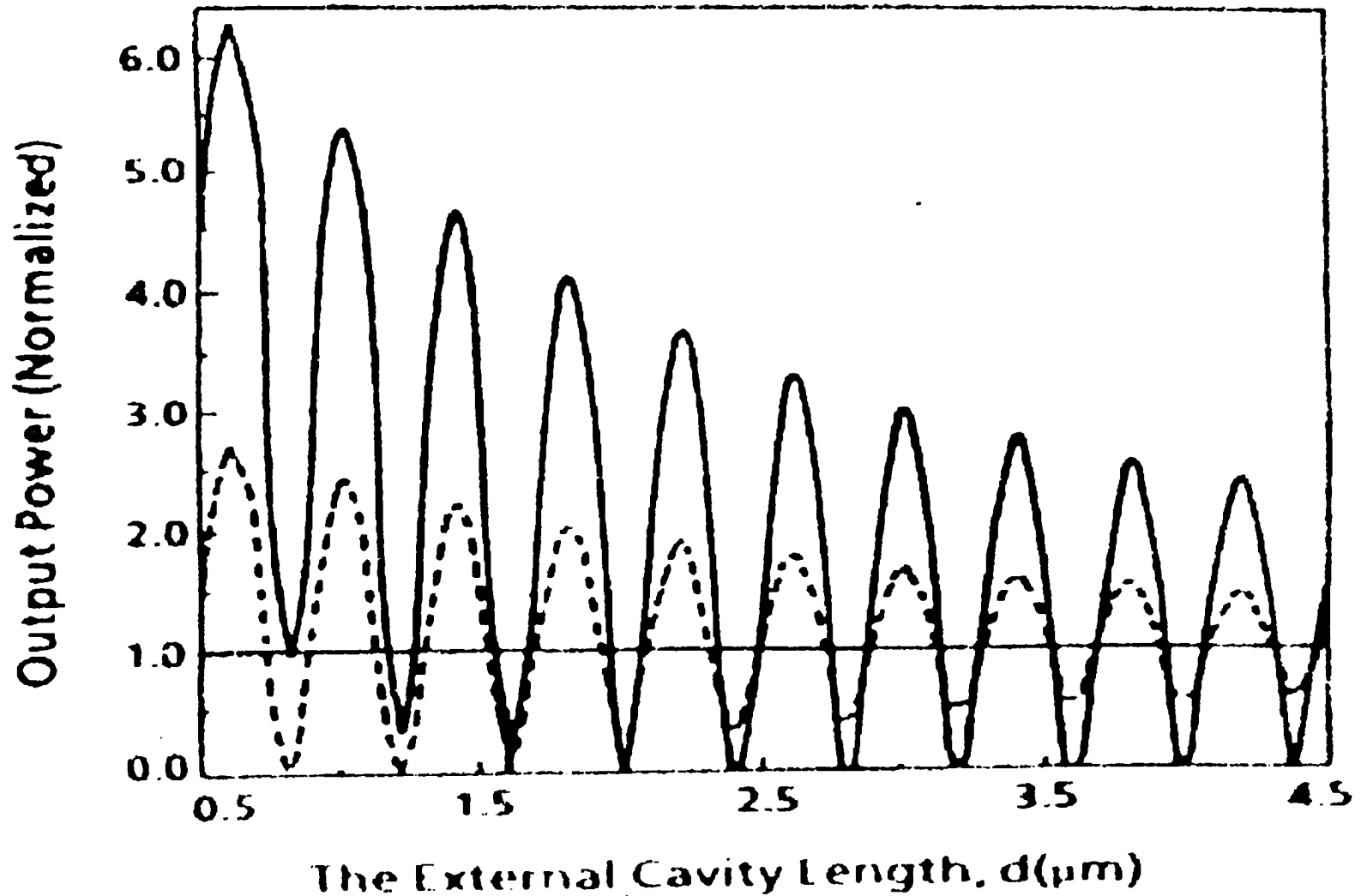


Figure D1.1 (b) Variation of output power versus external cavity length with two different sets of external reflector. The solid lines represent the plot of output variation using a 35% external reflector while the dashed line represents the output power fluctuation of the diode laser using a 4% reflector.

D1.2 Experimental Setup For Investigating Diode Laser Sensor Operating Characteristics

A few experiments were constructed to study the concept of a diode laser sensor. A microscope cover slide was attached to a commercially available stacked piezoelectric transducer and coupled to one facet of a diode laser. We observed a strong modulation on the output power of the diode laser as the coupling distance between the diode laser facet and the slide varied.

D1.2.1 Experimental Setup With Diode Laser And Microscope Cover Slide

A standard commercial 1.3 μm diode laser with a built-in monitoring photodiode was used in this experiment. The diode laser was mounted on a 9 mm header. The laser chip was manually mounted on the heat sink and was aligned with the edge of the heat sink as shown in Figure D1.2(a). Although the chip was carefully aligned, the ultimate coupling distance between the laser and the external reflector was obstructed by pits of solder as shown in Figure D1.2(a). We did not attempt to remove the solder since such operation would inevitably damage the facet of the laser. The diode laser was mounted on a diode laser mount (ThorLab MDT604), which was mounted onto a xyz flexure stage with 0.05 μm sensitivity (ThorLab MDT102).

A low voltage piezoelectric stack (Thorlab AE0505D16, maximum displacement of 17.0 μm at 150 V) served as an actuator to vary the coupling distance between the diode laser facet and a 4% reflector. The piezoelectric stack was epoxied to a blank mounting bracket (ThorLab MDT608). A 5 mm by 5mm regular microscope cover slide, with a refractive index approximately equal to 1.5, was attached to the other end of the

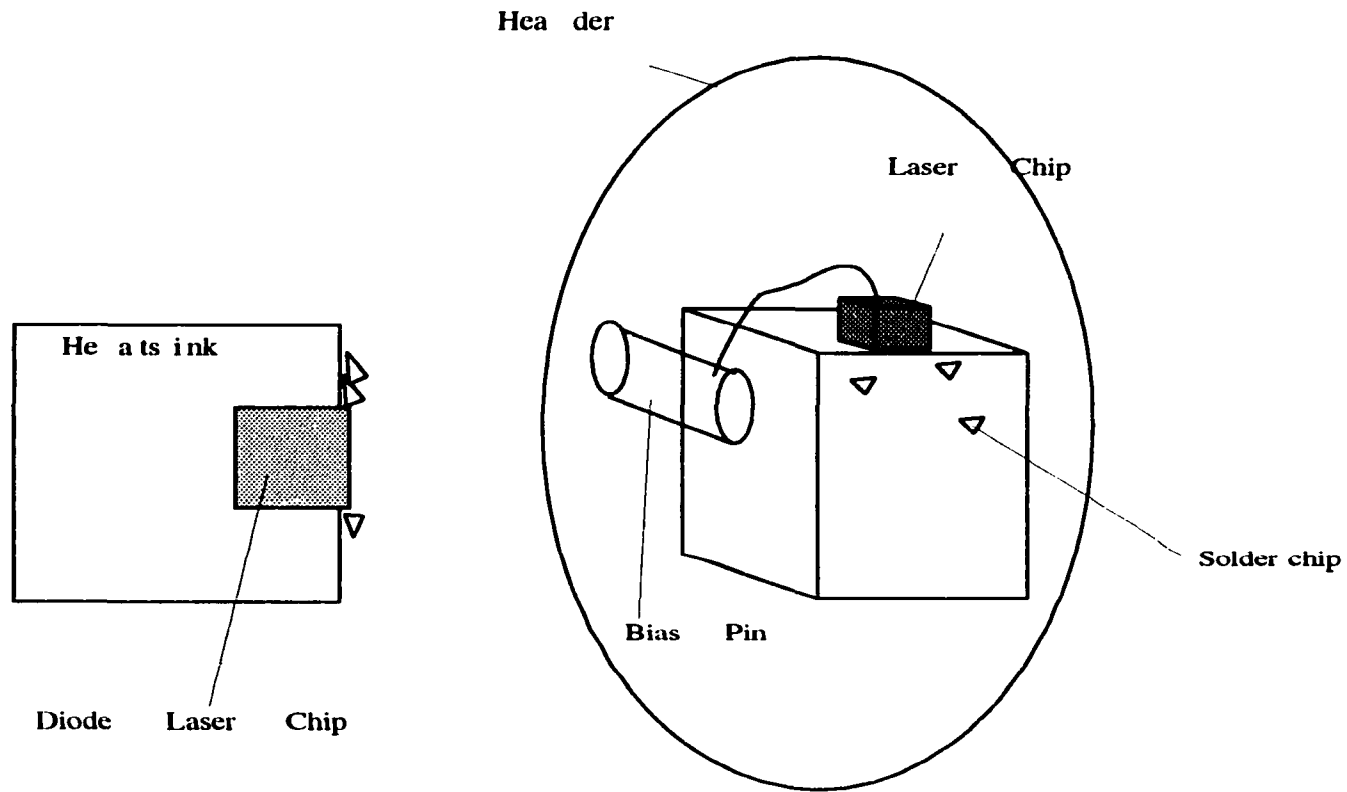


Figure D1.2 (a) Top view and side view of a diode laser chip mounted to a heatsink. Although the chip was carefully aligned the solder chip prevented a tight coupling distance.

actuator with Duco cement. A schematic diagram showing the experimental setup is shown in Figure D1.2(b).

Coarse adjustment on the coupling distance between the diode laser and the external reflector could be adjusted by the micrometer of the flexure stage while fine adjustment was controlled by a dc voltage applied across the piezoelectric stack. A HP 3325B function generator supplied both the dc voltage and the ac modulation voltage. The diode laser was biased with a low-noise current supply designed and fabricated during this program. No temperature control on the diode laser was used during this experiment.

D1.2.2 Experimental Setup With Diode Laser And 0.25 Pitch Rod Lens

We also attempted to use a 0.25 pitch rod lens a 4% external reflector. However, many commercially available 0.25 rod lens are antireflection coated on both ends and a mechanical polishing or chemical etching process was required to obtain a 4% reflection surface. We tried both mechanical and chemical techniques for removing the antireflection coating but the results were unsatisfactory. Although we were not able to carry out our experiment with a rod lens as the external reflector as planned, the external cavity effect could be verified with any 4% reflector. A one-side antireflection coated rod lens should be available as an OEM product from the manufacturer. Thus, all observations to be described in this report were obtained with the microscope slide setup.

D2.1 Observations

The threshold current of the solitary diode laser was measured to be approximately 40 mA. The diode laser was biased at 34.4 mA which corresponded to an dc output voltage of -

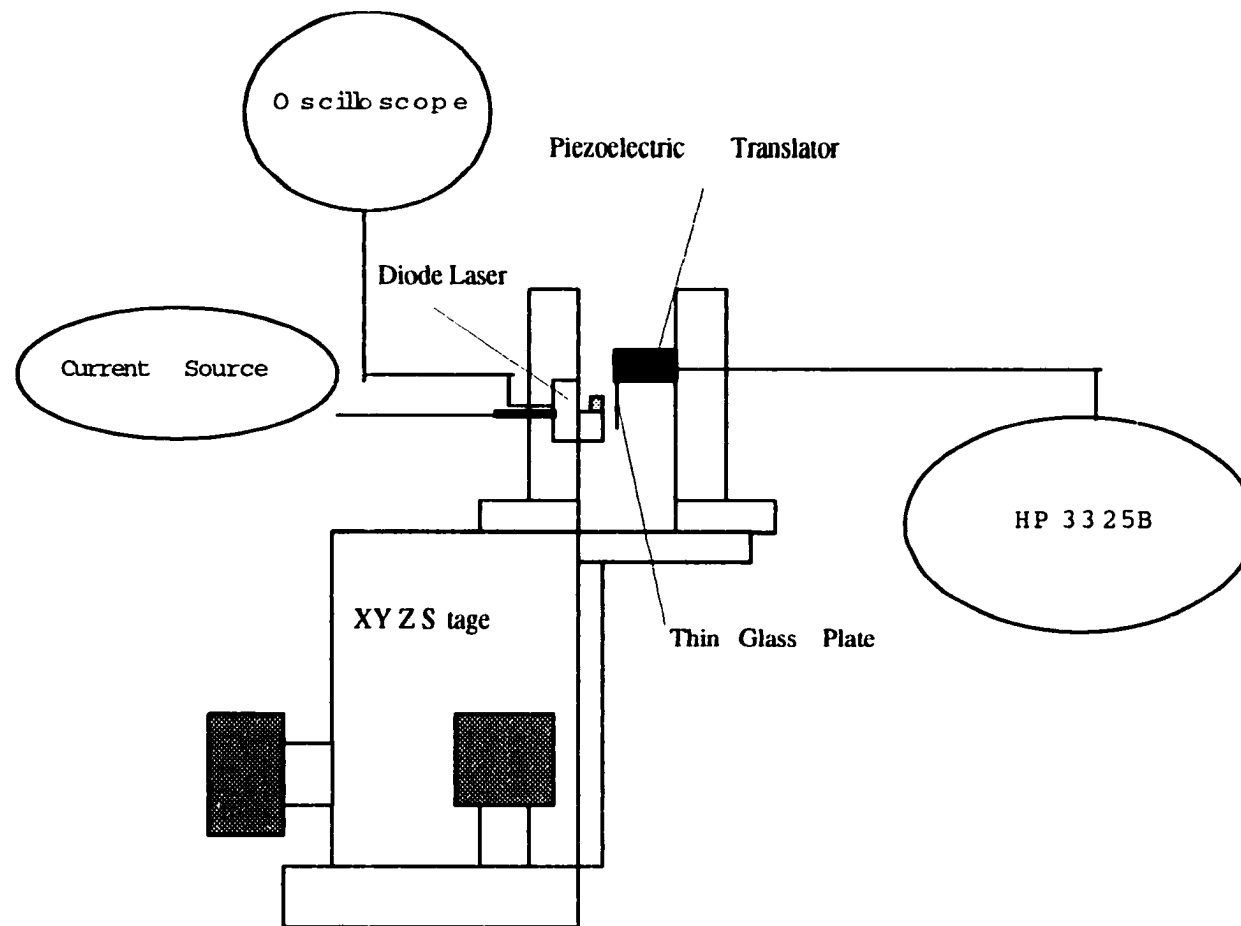


Figure D1.2 (b) Experimental setup for studying the reflectivity modulation property of a diode laser.

0.608 V on the monitoring photodetector. The diode laser was allowed to stabilize for 45 minutes before starting the experiment. The dc output of the monitoring photodetector dropped to -0.550 V at the end of the 45 minutes and the bias current was readjusted to 34.7 mA which corresponded to -0.605 V.

The x-axis of the stage was moved forward and set at an arbitrary point of $x=5$ (which was taken directly from the marking of the micrometer). The dc output of the monitoring photodiode increased to -0.695 V. Furthermore, a sinusoidal modulation voltage of 2 volts peak-to-peak was applied to the piezoelectric stack. The ac output of the monitoring photodiode was recorded with a digital storage oscilloscope (DSO). The output plot is shown in Figure D2.1.

With the diode laser bias current remaining at 34.7 mA and a 2Vpp ac modulation on the piezoelectric stack, the coupling distance was varied by the xyz flexure stage. At $x=10$, 15, 28 and 29.5, the dc output voltages were measured to be -0.689 V, -0.556 V, -1.100 V and -0.151 V respectively. Since there was no encoder available with the flexure stage, we were not able to verify if the reading directly taken from the micrometer was corrupted by backlash or other mechanical problems. Thus, a direct translation of the reading to absolute coupling distance was prohibited.

With the same diode bias current and ac modulation on the piezoelectric stack, a dc voltage of approximately 3.85 V was applied to the stack until a linear ac response was obtained on the DSO with a dc value at about -0.632 V. The ac output of the photodetector is shown in Figure D2.2. At a different dc voltage (i.e., -1.298 V) across the piezoelectric stack, we observed a minimum ac and dc response on the monitoring photodiode.

With the same diode bias current, the sinusoidal modulation voltage was replaced with a triangular modulation waveform of 7 Volts peak to peak. The ac output of the photodetector was recorded and is shown in Figure D2.3. The output of the photodetector

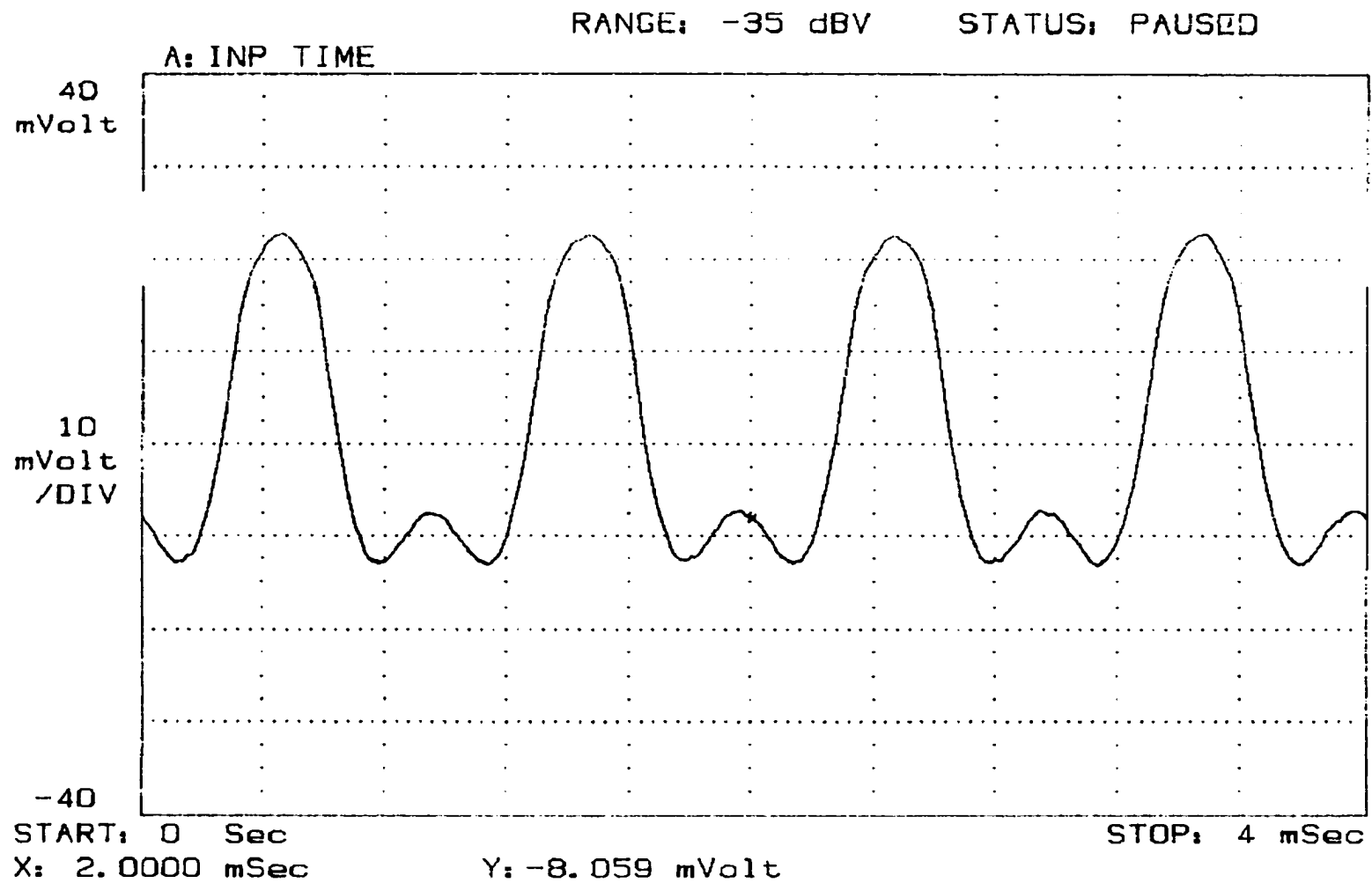


Figure D2.1 The output of the monitoring photodetector of a diode laser coupled to a 4% reflector. The coupling distance is modulated by a piezoelectric translator excited by a 1 volt peak sinusoidal voltage. The non-linearity of the output indicates the modulation span beyond a half a wavelength.

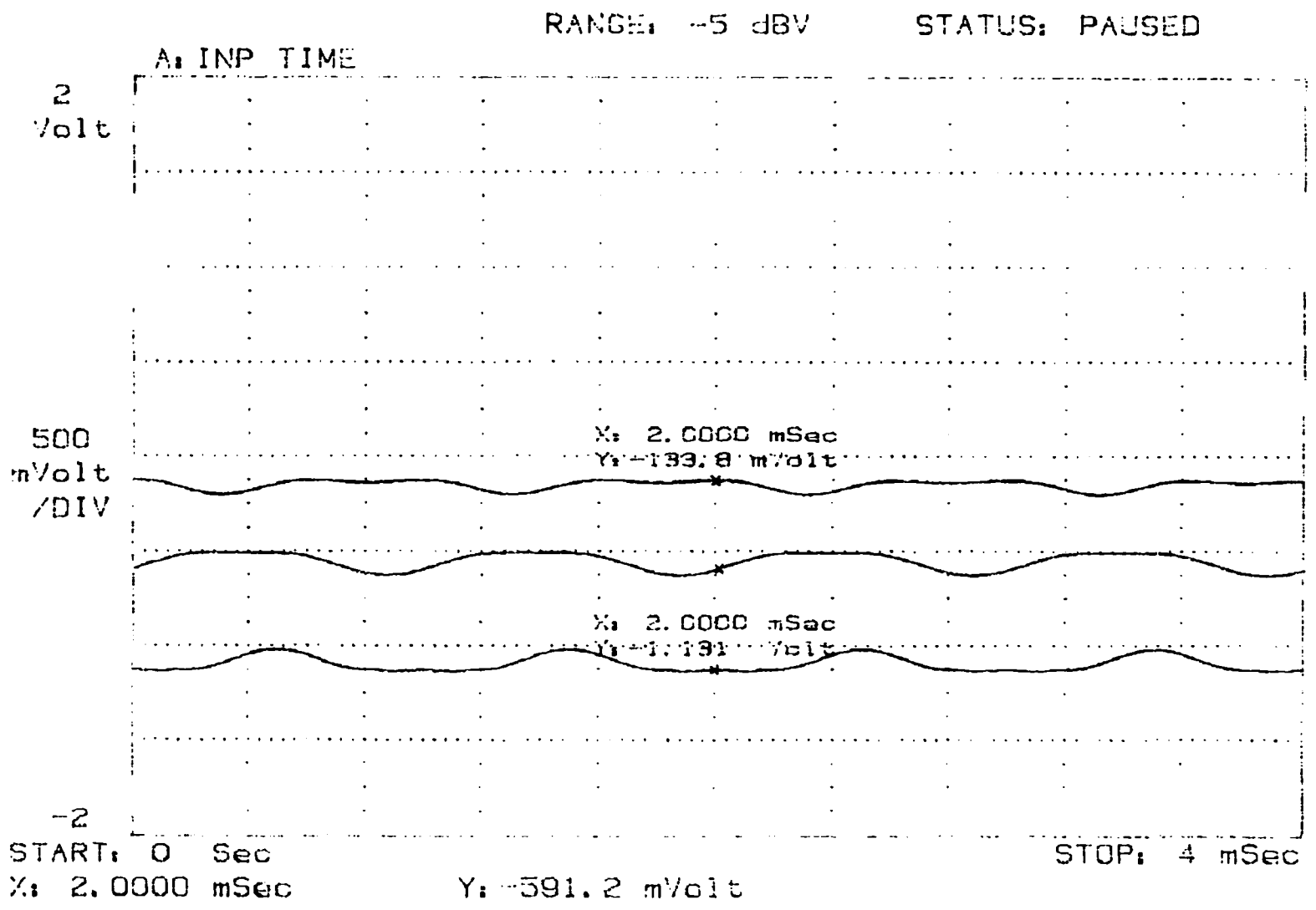


Figure D2.2 The dc output level of the monitoring detector at different coupling distances between the 4% reflector and the diode laser.

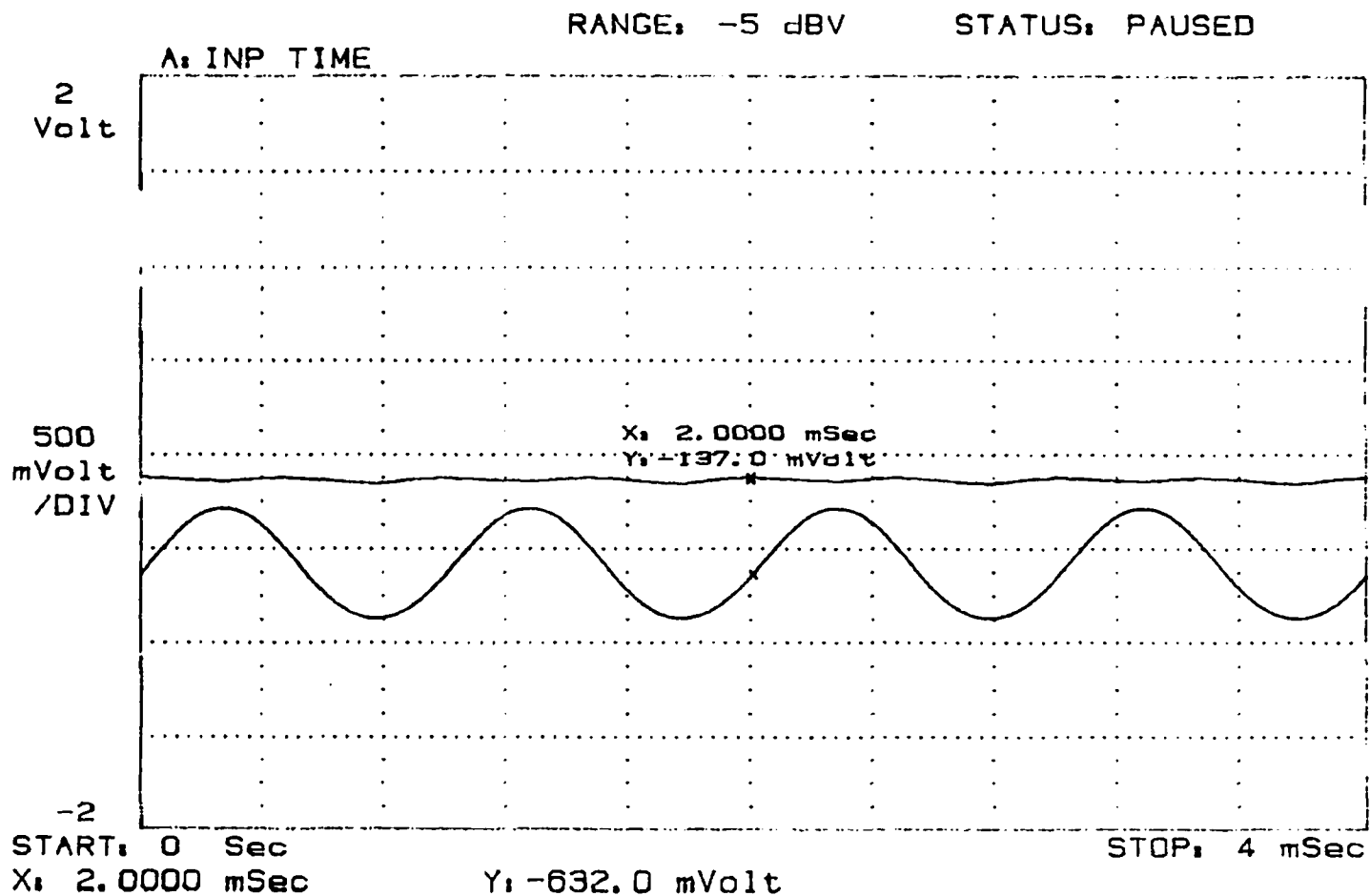


Figure D2.3 The output voltage of the photodetector when the coupling distance between the 4% reflector is modulated by an piezoelectric translator. The upper trace shows the output of the photodetector when the operating point of the system was set manually at its maximum. The lower trace shows the output of the system when it is biased at the optimal position.

fluctuated from -0.161 V to -1.200 V.

Increasing the diode laser bias current to 36.7 mA and using a triangular excitation of 8.0 Volts peak to peak, and a dc bias of 1.7 V across the piezoelectric stack, we were able to obtain a modulation on the monitoring photodiode from -0.081 V to 1.900 V. The result is shown in Figure D2.4. With a further increase of bias current of 46.7 mA and a triangular excitation of 9 Volts peak to peak and a dc bias of 2.7 V across the stack, we were able to obtain a modulation on the photodiode output from -0.7663 V to 3.400 V. The output of the photodetector is shown in Figure D2.5.

D3.1 Discussions Of Experimental Observations

The principle of an external cavity reflectivity modulator was demonstrated with the above experiments. Furthermore, the dc output level of the monitoring photodiode indicated the modulation effect of the 4% reflector on the effective facet reflectivity of the diode laser. For example, the dc output level of the diode laser, at 36.7 mA dc bias, was modulated from -0.081 V (i.e., non-lasing) to 1.900 V (i.e., lasing), a 23.5 times difference. As the bias current increased to 46.7 mA, the reflectance modulation demonstrated a 4.4 times difference. The diode laser seemed to be less susceptible to the reflectance modulation process as the current increased. We postulated that the reflectance modulation process translated the L-I curve to a new position. Moreover, the translated L-I curve may exhibit a slightly different slope. Thus, the modulation depth varied with the dc level of the bias current.

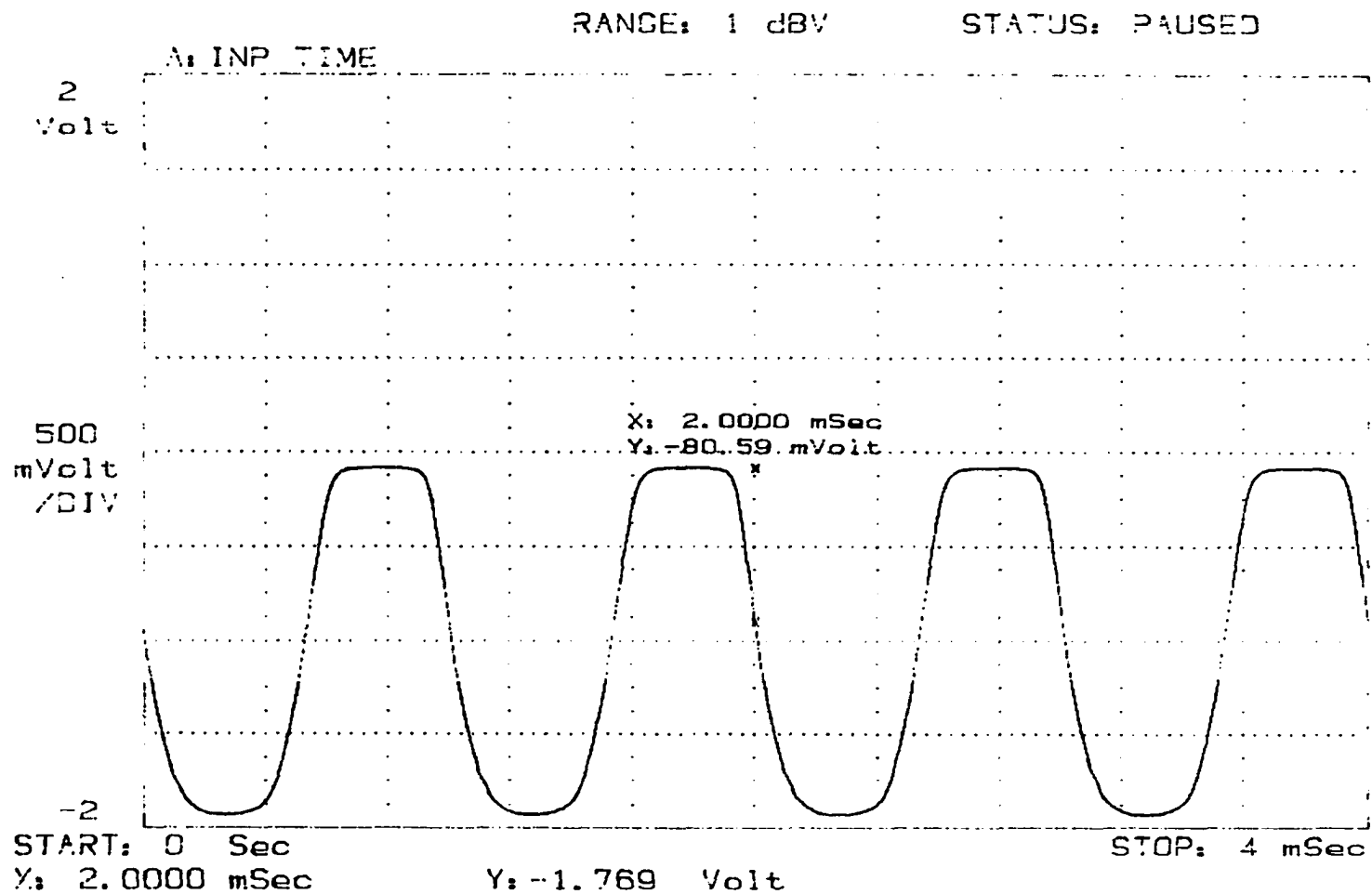


Figure D2.4 The output of the photodetector when the coupling distance between the 4% reflector and the diode laser is modulated with a 3.5 volts peak saw-tooth signal. The distortion of the waveform (i.e., the rounding off of the corner) may be a result of the bandwidth of the piezoelectric translator.

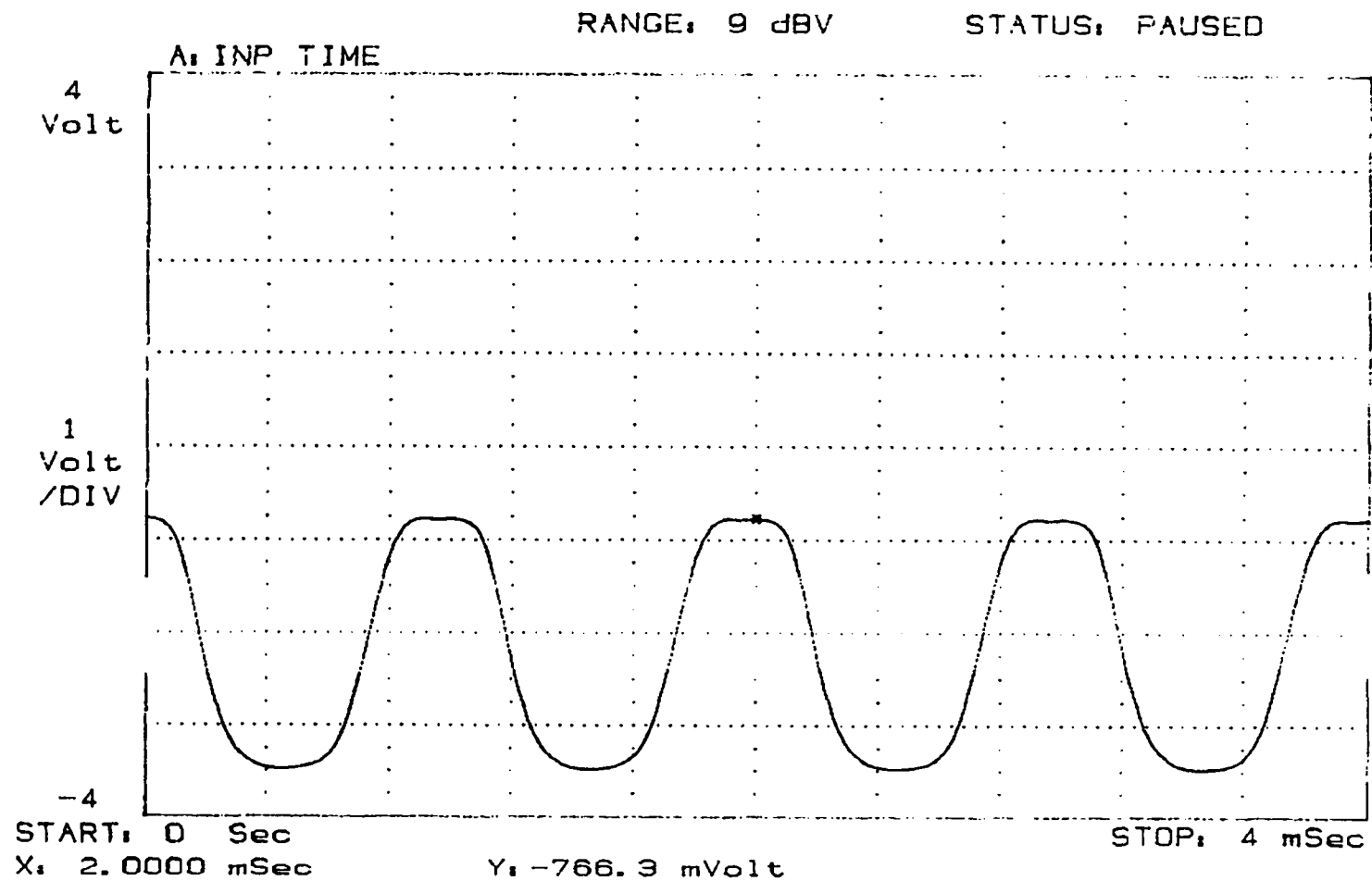


Figure D2.5 The output voltage of the photodetector when the coupling distance between the diode laser and the 4% reflector is modulated by a 4.5 volts peak saw-tooth signal. The dc bias level of the diode laser is increased considerably with respect to the experimental result shown in Fig. D2.4. With a higher bias, the output of the diode laser spans a greater range.

APPENDIX E: MATLAB SOURCE CODE FOR CALCULATING MODAL REFLECTIVITY

```
function F=f100(x);
n1=3.51; %apprx. core index
n2=3.22; %cladding index
lambda=1.3; % free space wavelength in micrometer
ko=2*pi/lambda; % wave-vector
d=0.1; %active layer thickness [2d=0.2 um]
temp=sqrt(n1^2-n2^2)*ko*d;
F=x.^2+x.^2.*(tan(x)).^2-temp^2; %Dispersion equation for sym wg
```

E2. Graphical Display Of Dispersion Equation Roots

```
x=0:0.01:1.3;
plot(x,f100(x)); grid on;
xlabel('x');ylabel('f(x), dispersion function');
title('Roots of Dispersion Relation');
root=fzero('f100',1.5,0.0001);
```

E3. Even Fundamental Te Waveguide Mode Generator

```
function F=f200(x);
root=0.5688; %propagation mode
d=0.1; %active layer thickness 2d=0.2 um
kappa=root/d;
gamma=(root*tan(root))/d;
```

```

for i=1:length(x);
    if ( abs(x(i))<d )
        F(i)=cos(x(i)*kappa);
    elseif ( abs(x(i))>d )
        F(i)=cos(kappa*d)*exp(-gamma*(abs(x(i))-d));
    else
        F(i)=0.00;
    end
end
end

```

E4. Graphical Display For Showing TE Waveguide Mode

```

x=-3:0.001:3;
plot(x,f200(x)); grid on;
xlabel('x, micrometer');ylabel('f(x),Normalized Amplitude');
title('Fundamental TE Waveguide Mode');
x=-3:0.001:3;
mode=f200(x);

```

E5. Spectral Representation For TE Mode

```

x=-3:0.001:3;
plot(x,f200(x)); grid on;
xlabel('x, micrometer');ylabel('f(x),Normalized Amplitude');
title('Fundamental TE Waveguide Mode');
x=-3:0.001:3;
mode=f200(x);

```

```
spectra=abs(fft(mode));
```

E6. Calculation Of Reflection Coefficients

```
#include <stdio.h>
#include <stdlib.h>
#include <math.h>
#include <malloc.h>
#include "complex.h"
#define k 8.05537 /* this is in per micrometer */
#define xbound 50
#define s_max 1.8
#define s_total 100
#define delta_s 2.0*s_max/s_total
#define start_h 0.0
#define del_h 0.05
#define h_total 100

double *data;
int total_number;

/* input: The components of the incident wavevector */
/* The thickness of the coupling gap */

void main(int, char **);
void ReadGrid(char *);
```

```

void main(int argc, char *argv[])
{

    FILE *fp1;
    int i,j,ii,ih;
    complex *wave, *corr;
    double x, z,delta_x,tmp_re,tmp_im,s,s2,t;
    /* Read in surface profile file */

    /* Check to see if data_file exist */
    if ((fp1=fopen(argv[1], "r")) == NULL)
    {
        printf("No matching pattern for '%s'\n", argv[1]);
        exit(-1);
    }
    fclose(fp1);
    ReadGrid(argv[1]);
    printf("Total number is %d\n", total_number);
    wave = (complex *)calloc(total_number+1, sizeof(complex));
    corr = (complex *)calloc((h_total+1)*(s_total+1), sizeof(complex));

    /* for (i=1;i<=total_number;i++) printf("%d %lf\n",i,data[i]); */
    for (ih=1;ih<=h_total;ih++)
    {
        t = start_h + (double)del_h*(ih-1);

```

```

for (ii=1;ii<=s_total;ii++)
{
    printf("ih is %d t is %lf\n",ih,t);
/* Calculate the phase and amplitude of the wavefront and put them in array */
    s2=-1.0*s_max + (double)ii*delta_s;
    printf("s2 is %lf\n",s2);
    delta_x= xbound*2.0/total_number;
    for (i=1;i<=total_number;i++)
    {
        x= -1.0*xbound +(double)i*delta_x;
        z= t-data[i];
/*      z= t; */
        if (1-s2*s2 >= 0)
        {
            wave[i].re = cos(k*s2*x)*cos(k*sqrt(1-s2*s2)*z) - sin(k*s2*x)*sin(k*sqrt(1-s2*s2)*z);
            wave[i].im = sin(k*s2*x)*cos(k*sqrt(1-s2*s2)*z) + sin(k*s2*x)*sin(k*sqrt(1-s2*s2)*z);
        }

        if (1-s2*s2 < 0)
        {
            wave[i].re = cos(k*s2*x)*exp(-1.0*k*sqrt(s2*s2-1)*z);
            wave[i].im = sin(k*s2*x)*exp(-1.0*k*sqrt(s2*s2-1)*z);
        }
/*      printf("wave re %lf im %lf\n",wave[i].re,wave[i].im);
*/    }

```

```

/* end for i */

/* Perform dot product with all available components */

    for (i=1;i<=s_total;i++)
    {
        s=-1.0*s_max + (double)i*delta_s;
/*      printf("s is %lf\n",s);
*/      tmp_re=0.000000;
        tmp_im=0.000000;
        /* integrate using trapezoidal rule */
        for (j=1;j<total_number;j++)
        {
            x= -1.0*xbound +(double)j*delta_x;
/*          printf(" x is %lf\n",x);
*/          tmp_re = tmp_re + 0.5*delta_x*(wave[j].re*cos(k*s*x) -
wave[j].im*sin(k*s*x)+wave[j+1].re*cos(k*s*(x+delta_x)) -
wave[j+1].im*sin(k*s*(x+delta_x)));
            tmp_im = tmp_im + 0.5*delta_x*(wave[j].im*cos(k*s*x) +
wave[j].re*sin(k*s*x)+wave[j+1].im*cos(k*s*(x+delta_x)) +
wave[j+1].re*sin(k*s*(x+delta_x)));
        }
        corr[((ih-1)*s_total)+i].re = corr[((ih-1)*s_total)+i].re + tmp_re;
        corr[((ih-1)*s_total)+i].im = corr[((ih-1)*s_total)+i].im + tmp_im;
/*      printf("%d,%d,%d,%lf,%lf,%lf\n",ih,i,(int)(ih-1)*s_total+i,corr[(int)(ih-

```

```
l)*s_total+i].re,corr[(int)(ih-1)*s_total+i].im,s);
*/
    }
    /* end for i */
}
/* end for s */
}
/* end for ih */
for (ih=1;ih<=h_total;ih++)
{
    for (i=1;i<=s_total;i++)
    {
        printf("%lf,%lf\n",corr[((ih-1)*s_total)+i].re,corr[((ih-1)*s_total)+i].im);
    }
}
/* end for */
/* Update spectral components */

}
/* end main */

/* function for memory allocation */
```

```
void ReadGrid(char *data_file)
{
FILE *fp1,*fp2;
int error, i, counter,sum,location;
double height;
char comma;

/* check to see if time file exist */
fp2=fopen(data_file,"r");
if (fp2 == NULL)
{
printf(" ... The data file \"%s\" cannot be opened.\n", data_file);
exit(-1);
} /*end if */

/* Check to see how many points are there */
error = 1; /* set flag to default */
sum=0;
while (error > 0)
{
error=fscanf(fp2, "%d %lf\n",&location,&height);
/* printf("%d %lf\n",location,height); */
if (error > 0) sum=sum+1;
}
}
```

```
fclose(fp2);

printf("Total number of data point is %d\n",sum);
if(((data=(double *) calloc(sum+16,sizeof(double))) == NULL)
{
    printf("error assigning mem\n");
    exit(-1);
}
else
{
    printf("memory allocated for surface profile\n");
}
fp1=fopen(data_file,"r");
for (i=1;i<=sum;i++)
{
    error=fscanf(fp1,"%d %lf\n",&counter,&height);
    data[i]=height;
/*    printf("data %d is %lf %lf\n", i, data[i], height);*/
}
total_number=sum;
/*    printf("Total is %d\n",total_number); */
fclose(fp1);
} /* end ReadGrid*/
```

APPENDIX F: DESCRIPTION OF THE ON-BOARD MICROCONTROLLER

The basic functions of the signal processing electronics are to convert the analog signal received from the photodetector circuitry to digital signal, and perform the digital signal processing functions. The computation results will be displayed by a 16 characters x 1 line liquid crystal display (LCD) module. The prototype provides both the frequency and the intensity of the ac magnetic field. A threshold can be preset by the user to determine the number of Fourier spectra being displayed. Due to the limitation of the microcontroller development system, we are limited to an off-chip EPROM version of the microcontroller. A 16-bit Intel A8097BH microcontroller is used as a main controller, which is a ROMless derivative of the popular MCS-96 series controller. The "address valid with write strobe" bus mode is chosen to support the 16 bit external bus. A multiplexing scheme, implemented with a 74LS573, was used in the design. The two 2716 EPROM supplies the 2K word length memory space for the DSP algorithm and other housekeeping codes. Two 6426 SRAM provides the 8K word length scratch pad memory space for DSP computation. The built-in 10-bit A/D converter is used to sample the output data from the analog electronics. The successive approximation conversion time is about 88 state times, which is approximately 25 microsecond with a 10 Mhz clock speed. A block diagram showing the design is shown in Figure F1.

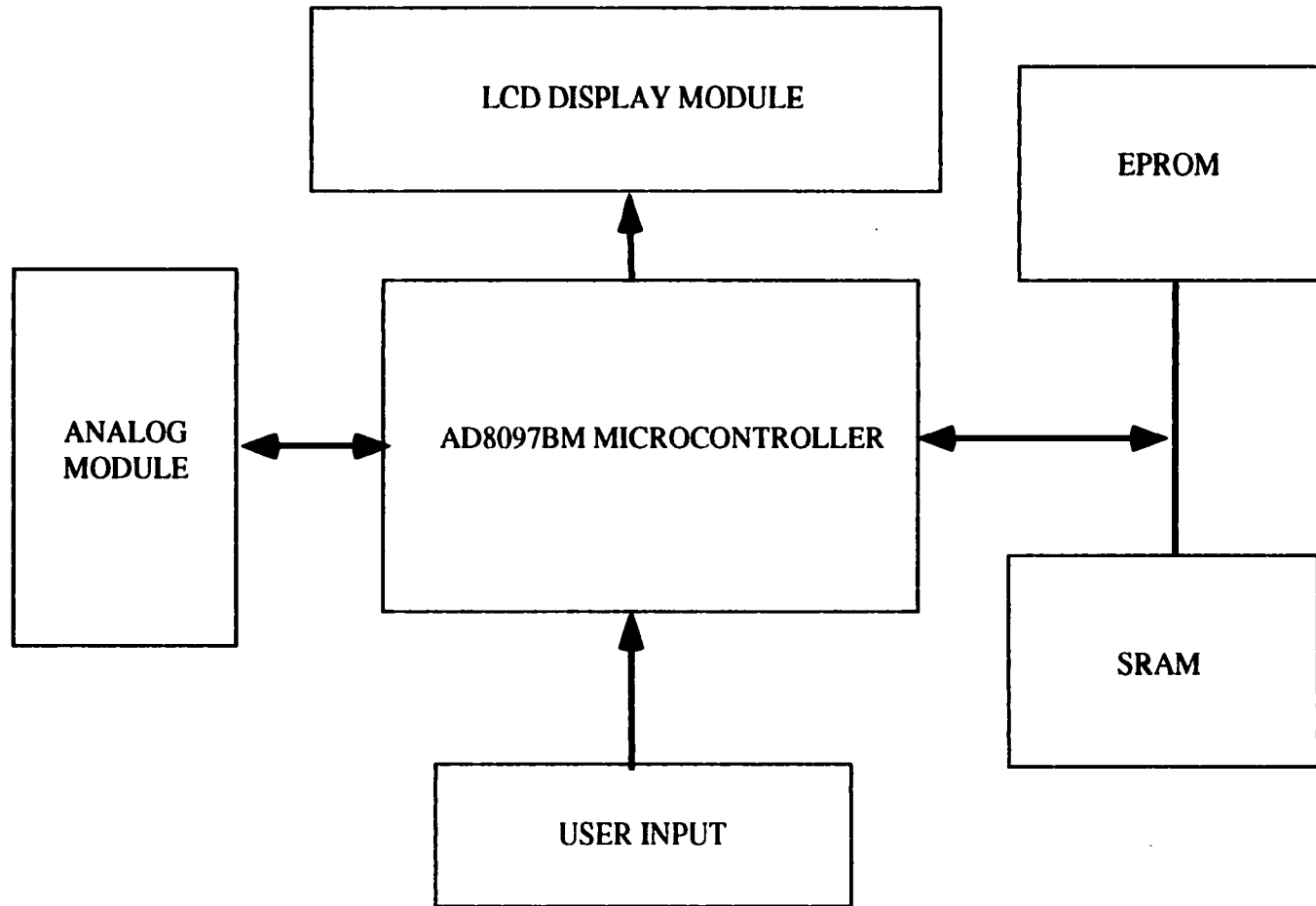


Figure F1. Block diagram showing the organization of the on-board microcontroller unit developed for the pocket size magnetometer.

APPENDIX G: APPLICATION OF AN EXTERNAL CAVITY SENSOR IN THERMAL DISTORTION IMAGING

A diode laser external cavity sensor, identical to the one being described in this thesis, was also used to image the thermal distortion of a microscope slide. This work was performed during the development of a thermal wave based eddy current diagnostic instrument. A technique was developed to investigate the response of an eddy current probe to a localized impedance change, as a result of a thermal perturbation, of a gold coated microscope slide. Questions were raised on whether the response obtains with the instrument a result of lift-off effect or the actual response due to the localized impedance change.

The highly sensitive diode laser sensor was coupled closely to the microscope and a spatial scan was performed. Although the optical table was de-stabilized by the chilling water pump of the Ar⁺ laser, the sensor was able to detect the thermal bump on the microscope slide. The relationship between the chopping frequency and the magnitude of lift-off was investigated. The details of the experiment was published in [31].

REFERENCES

- [1] R. Chung, "A laser diode magnetostrictive terfenol-d magnetometer", M. S. thesis, Iowa State University, Ames, 1990 and references listed therein.
- [2] I. Hickman, *Analog and RF Circuits*, Newnes, Reed Educational and Professional Publishing Ltd., London, 1998.
- [3] R. Chung, R. Weber, and D. C. Jiles, "The Magnetostrictive Laser Diode Magnetometer for Personal Magnetic Field Dosimetry", *Proc. 37th Annual Magnetism and Magnetic Materials Conference*, Houston, November, 1992. *Journal of Applied Physics*, 73(6):5638-5639, 1993.
- [4] J. Y. Kim and H. C. Hsieh, "An Open Resonator Model for the Analysis of a Short External Cavity Laser Diode and its Application to the Optical Disk Head", *IEEE J. of Lightwave Tech.*, LT-10(4):439-447, 1992.
- [5] R. Miles, A. Dandridge, and A. Tveten, "An External Cavity Diode Laser Sensor". *IEEE J. of Lightwave Tech.*, LT-1(1):81-92, 1983.
- [6] OP-35 Application Notes, published by Ultra-Optec, Quebec, 1990.
- [7] M. P. Shultz, R. Chung, J. Greenough, R. Greenough, D. C. Jiles, and R. Weber, "Variation of Strain Amplitude and Phase in a Cylindrical Specimen of Td-Dy-Fe in an AC Field", *IEEE Trans. on Magnetics*, 28(2):3162-3167, 1992.
- [8] A new differential micrometer translator was later purchased. However, it also deemed very difficult to apply this with a high level of repeatability.
- [9] Yet-zen Liu of Fermionics Inc., 4928 Front Street, Simi Valley, California, can provide specially coated devices.
- [10] Analog Devices Application Support Group, private communications
- [11] Burr-Brown Application Support Group, *Application Note AN-3*, Burr-Brown, Phoenix, 1992
- [12] Burr-Brown technical support group, *Analog Circuits Application Note Book*, Burr-Brown, Phoenix, 1992
- [13] C. C. Bradley, J. Chen, and G. Hulet, "Instrumentation for the Stable Operation of Diode Laser", *Rev. Sci. instr.*, 61(8):2097-2103, 1990.
- [14] T. Ikegami, "Reflectivity of Mode at Facet and Oscillation Mode in Double Heterostructure Injection Lasers", *IEEE J. Quantum electronics*, QE-6(6):470-478, 1972.

- [15] L. Lewin, "A Method for the Calculation of the Radiation Pattern and Mode Conversion Properties of a Solid State Laser", *IEEE Trans. on Microwave Theory Tech.*, 23(7):576-584, 1975.
- [16] T. Rozzi, J. Chen, and G. Hulet, "Variational Treatment of the Diffraction at the Facet of Double Heterostructure Laser and of Millimeter Wave Dielectric Antenna", *IEEE Trans. Microwave Theory Tech.*, 31(2):199-207, 1983.
- [17] J. Schwinger and D. S. Saxon, *Discontinuity in Waveguides*, Gordon and Breach, New York, 1968.
- [18] T. Rozzi, *Open Electromagnetic Waveguide*, IEE Press, London, 1997
- [19] S. Vassallo, *Optical Waveguide Theory*, Elsevier, San Diego, 1993
- [20] P. Kendall, et. al., "Semiconductor Laser Facet Reflectivity Using Free-Space Radiation Modes", *IEE Proceedings-J*, 140(1):49-52, 1993.
- [21] P. Kendall, et. al., "New formula for semiconductor laser facet reflectivity", *IEEE Photonics Tech. Lett.*, 5(2):205-213, 1993.
- [22] T. Rozzi, "Rigorous Analysis of the Step Discontinuity in Dielectric Waveguide". *IEEE Trans. Microwave Theory Tech.*, 26(10):736-744, 1978.
- [23] D. Kaplan and P. Deimel, "Exact Calculation of the Reflection Coefficient for Coated Optical Waveguide Devices", *BSTJ* (63) 6:857-877, 1984.
- [24] D. Marcuse, *Theory of Dielectric Optical Waveguide*, Academic Press, San Diego, 1978
- [25] H. Hamstra and K. Wendland, "Performance of PIN Photodiode", *Applied Optics*, 61(8):470-476, 1971
- [26] R. Chung, unpublished data. This was obtained at Quantum Magnetics, Inc., of San Diego, CA, during the development of an undersea surveillance sensor. The data was submitted as reports to Naval Research and Development Facility.
- [27] K. Petermann, *Laser Diode Modulation and Noise*, Kluwer Academic Publisher, Tokyo, 1988.
- [28] J. Y. Kim, R. W. Chung, and J. Moulder, "Measurement of Photothermally Induced Distortion of Thin Films Using an External Cavity Laser Diode Sensor." *Electronics Letters*, Vol. 29(4):1057-1060, 1993.
- [29] Robert Bernier of Ultra-Optec, Quebec, private communication. This derivations are a result of the author's effort in calibrating the OP-35 and communication notes to resolve an inconsistent calibration figure of the OP-35.
- [30] I. A. Viktorov, *Rayleigh and Lamb waves: Physical theory and Applications*, Plenum Press, New York, 1967, Vol. 154.

- [31] J. P. Monchalin, R. Heon, J. F. Bussiere, and B. Farahbakhsh, "Heterodyne Interferometer for Non-destructive Evaluation", *Journal of Nondestructive Evaluation*, Vol. 8(2):121-133, 1989.
- [32] R. Chung, R. Weber, and D. C. Jiles, "A Terfenol Based Magnetostrictive Diode Laser Magnetometer," *IEEE Trans. on Magnetics*, Vol. 27(6):5358-5360, 1991.

ACKNOWLEDGEMENTS

The author would like to acknowledge the financial support of the Electric Power Research Center of Department of Electrical and Computer Engineering at Iowa State University. This dissertation work was funded under the Iowa Test and Evaluation Facility program directed by Dr. John Lamont. Furthermore, the author would like to acknowledge the immense effort of Dr. David Jiles and Dr. Robert Weber in reviewing and revising this dissertation. Moreover, the author would like to acknowledge the late John Moulder for the working and learning opportunity at the Thermal Wave and Optics Laboratory at the Center for Non-destructive Evaluation (CNDE). All of the experimental equipments for this dissertation were provided by the optics lab. at CNDE. Also, I would like to thank Dr. H. C. Hsieh and Dr. A. Gauteson for serving in the committee. The author would like to thank many of the co-workers, such as Dr. Jin-Yong Kim, Dr. Mike Hughes, Mark Kubovich, Greg Dace, Dr. Jim Rose, Dr. Nario Nakagawa of CNDE, for assistance and contribution in many experimental and theoretical issues. Last but not least, I would like to thank my family members for the support in finishing this dissertation.